Numerical Assessment of Directional Stability and Control with Tip-mounted Propellers

Sylvain van der Meer

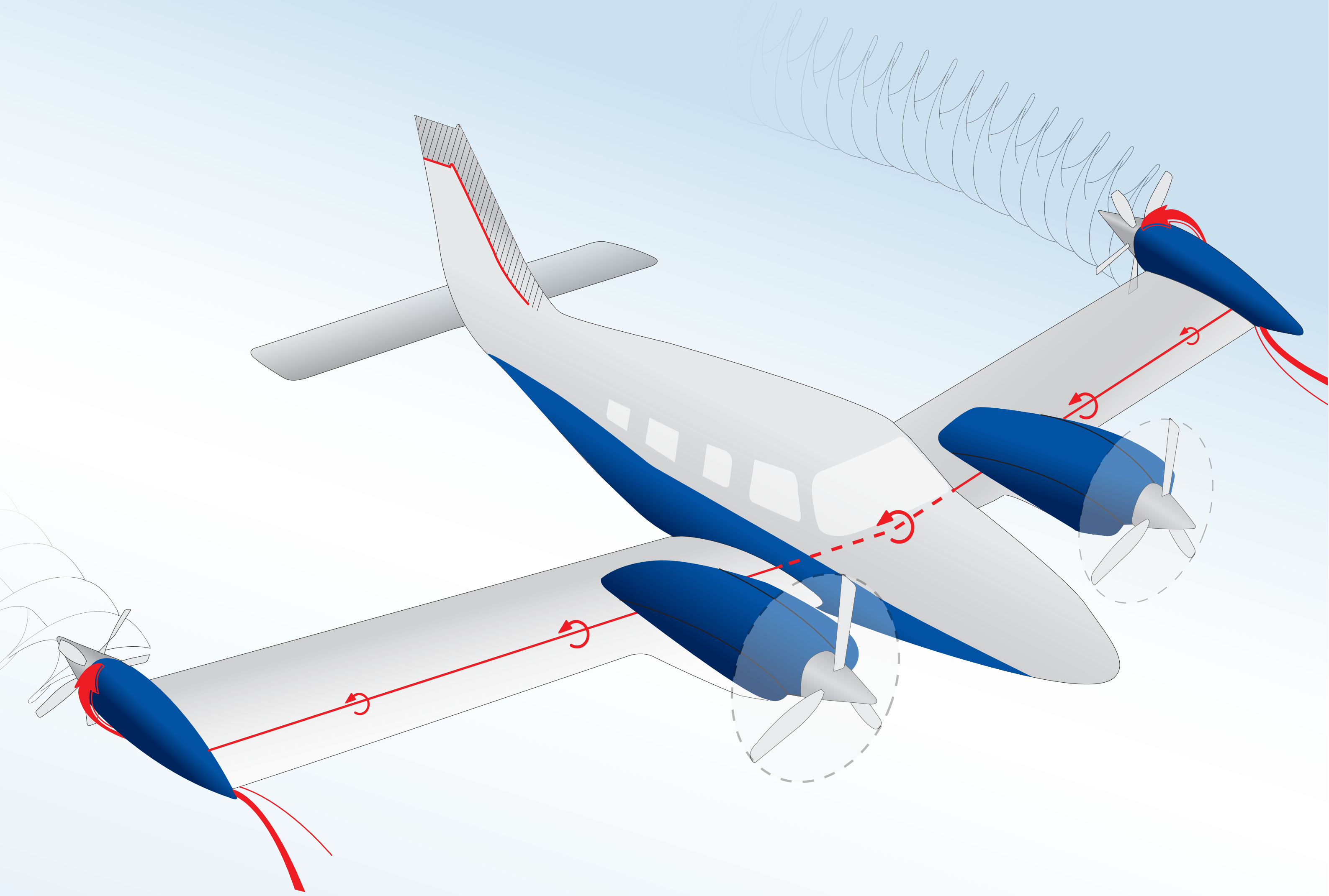

Delft University of Technology

Numerical Assessment of Directional Stability and Control with Tip-mounted Propellers

by

Sylvain van der Meer

to obtain the degree of Master of Science
at the Delft University of Technology,
to be defended publicly on Friday January 24, 2020 at 13:30.

Student number:	4214773	
Project duration:	September 17, 2019 – January 24, 2020	
Thesis committee:	Prof.dr.ir. L.L.M. Veldhuis,	TU Delft, supervisor, chair
	Dr.ir. T. Sinnige,	TU Delft, daily supervisor
	Prof.dr.ir. M. Voskuijl,	Nederlandse Defensie Academie
	Dr.ir. E. van Kampen,	TU Delft

An electronic version of this thesis is available at http://repository.tudelft.nl/.

TU Delft

Summary

A propeller has a high propulsive efficiency, yet inherently leaves the air it propels swirling. The efficiency of a propeller can be enhanced by placing it in the tip vortex of a wing. Such a tip-mounted propeller configuration lets the vortex created by the wing and the vortex created by the propeller counteract each other, enhancing the propulsive efficiency of the system.

Even though the benefits of such a configuration are clear, the concept is not commercially viable. Among other benefits, electric engines are scalable, light and can be placed in advantageous positions. This allows the engine to be placed at the tip of a wing. The batteries for electric propulsion are heavy, so synergistic effects are needed to improve the efficiency to such an extent that electric propulsion will be commercially viable.

Another benefit can be defined by tip-mounted propulsion. As the propeller is mounted at the tip of the wing, the moment arm is large. This could result in a large directional control moment. On the other hand, if one engine is inoperative, the resulting moment is so large that it cannot be compensated by a rudder deflection. Therefore, if a one-engine inoperative situation arises, to still produce thrust both propellers have to be interlinked resulting in a heavy system, or both engines should be switched off.

If tip-mounted propellers are used to enhance directional stability and control, the vertical tailplane size can be reduced, resulting in a reduction of mass, drag and hence overall power consumption. In this thesis the contribution of tip-mounted propellers to static stability, dynamic stability, and control is researched, for both positive and negative input power. Negative input power denotes that the propellers are recuperating energy from the airflow, and is a state that is applicable when one engine is inoperable.

The forces on a tip-mounted pusher propeller are obtained by linking a lifting line wing model and a combined blade-element momentum vortex propeller model. The lifting line model is used to calculate wing-induced velocities on the pusher propeller disk. These induced velocities are used as input for the propeller model, and a resulting thrust and power is obtained. These are corrected for an angle of attack on the propeller disk by empirical relations. The thrust, normal force and power are saved to a 7D dataset. A non-linear flight mechanics model of the Piper Seneca III uses the dataset as lookup table and implements the tip-mounted propeller as forces at the tip locations.

Thrust variations in the 7D dataset are parametrically visualised, showing the expected trends. Resulting forces are compared with a rudder deflection, to estimate a potential rudder size reduction. When the aircraft is flying slow, tip-mounted propellers can match the maximum moment produced by the conventional rudder. When flying fast, around half the reference yawing moment can be produced by tip-mounted propellers.

The static stability contribution of tip-mounted propellers is visualised parametrically for propeller diameter, advance ratio, blade pitch and a toe-in angle. Negative toe-in angles, hence toe-out angles, prove to greatly enhance the directional static stability. High thrust values greatly enhance longitudinal static stability as the reference aircraft's wing tips are positioned above the centre of gravity.

In the same parametric fashion as the static stability evaluation, the contribution of tip-mounted propellers to dynamic stability is evaluated. The damping factor and natural frequency are obtained for first order motions Dutch roll and the Phugoid by fitting an exponential curve to the time-response of the flight mechanics model. This method succeeds in capturing the motion characteristics, and indicates clear trends: the frequency of the Dutch roll increases with toe-out angles and thrust, and the frequency increases with thrust. The Phugoid's natural frequency increases with thrust, and damping factor decreases with thrust. An attempt is done to use the curve-fitting method for the second order motion Short period as well, yet proves too inaccurate.

A typical tip-mounted propeller design is evaluated to summarise the effects of using tip-mounted propellers for directional stability and control. For this non-optimised design, the static stability is enhanced by 37%. The dynamic stability has increased significantly as well. Maximum blade pitch deflection and maximum rudder deflection result in similar time-history sideslip responses when the aircraft is flying slow, when flying fast the tip-mounted propeller design's sideslip response is around half the reference rudder deflection response. This conclusion also applies to a one engine inoperative simulation.

In this thesis, a significant first step is made toward enhancing directional stability and control with tip-mounted propellers by defining the contribution of tip-mounted propellers in a parametric fashion. The results are directly applicable to an aircraft that has been designed with tip-mounted propellers, yet does not rely on tip-mounted propellers for directional stability and control. A typical design is evaluated in cruise, recuperative and one-engine inoperative cases, proving that from a stability and control point of view the vertical tailplane can be reduced in size.

Before tip-mounted propellers can be used for directional stability and control behaviour analysis in the stalled regime, more research has to be conducted. This is left as recommendation.

List of Terms and Acronyms

Notation	Description
AVL	Athena Vortex Lattice, Vortex Lattice Method software package
BEM	Blade-Element Momentum
CFD	Computational Fluid Dynamics
CG	Center of gravity
JavaProp	Software package for low-fidelity propeller analysis
MAC	Mean aerodynamic chord
Matlab	Engineering programming language
OEI	One engine inoperative
Python	Programming language
SciPy	Open-source software for mathematics, science, and engineering
Simulink	Simulation and Model-Based Design software
TMP	Tip-mounted propeller
VTP	Vertical tailplane
XFOIL	Interactive isolated subsonic airfoil development and analysis system
XROTOR	Software package for low-fidelity propeller analysis

List of Symbols

Notation	Description
α	Wing angle of attack [deg]
α_e	Section effective angle of attack [deg]
α_p	Propeller angle of attack [deg]
$a_{n_{x_b}}$	Body frame normal acceleration in X $[\mathrm{m} \cdot \mathrm{s}^{-2}]$
$a_{n_{y_b}}$	Body frame normal acceleration in Y $[\mathrm{m} \cdot \mathrm{s}^{-2}]$
$a_{n_{z_b}}$	Body frame normal acceleration in Z $[\mathrm{m} \cdot \mathrm{s}^{-2}]$
b	Wing span [m]
β_p	Propeller blade pitch [deg]
β_s	Aircraft sideslip angle [deg]
c	Wing chord [m]
C_L	3D Lift coefficient [-]
c_l	2D Lift coefficient [-]
C_{l_α}	2D Lift coefficient due to angle of attack
C_{m_α}	Pitch moment coefficient due to angle of attack
C_n	Yaw moment coefficient
C_{n_β}	Yaw moment coefficient due to sideslip
$C_{n_{\delta_r}}$	Yaw moment coefficient derivative due to rudder deflection
$C_{n_{TMP}}$	Yaw moment coefficient due to TMP forces
C_{n_r}	Yaw moment coefficient derivative due to yaw rate
C_P	Power coefficient [-]
C_T	Thrust coefficient [-]
C_{X_u}	Tangential force coefficient derivative due to X-velocity
C_{Y_β}	Side force coefficient derivative due to sideslip
C_{Z_u}	Normal force coefficient derivative due to Z-velocity
D	Diameter [m]
δ_e	Elevator deflection [deg]
δ_r	Rudder deflection [deg]
ζ	Eigenmotion damping factor [-]
f	Parameter fraction [-]
Γ	Vorticity strength $[\mathrm{m}^2 \cdot \mathrm{s}^{-1}]$
γ	Flight path angle [deg]
J	Advance ratio [-]
K_P	Power fraction of original Seneca engine [-]
N	Number of line sections [-]
n	Propeller rotational speed $[\mathrm{s}^{-1}]$
P	Propeller input power [J]
p	Aircraft roll-rate $[\mathrm{rad} \cdot \mathrm{s}^{-1}]$
ϕ	Roll angle [deg]
η_p	Propeller propulsive efficiency [-]
q	Aircraft pitch-rate $[\mathrm{rad} \cdot \mathrm{s}^{-1}]$
r	Aircraft yaw-rate $[\mathrm{rad} \cdot \mathrm{s}^{-1}]$
Re	Reynolds number [-]
ρ	Density $[\mathrm{kg} \cdot \mathrm{m}^{-3}]$
σ_e	Effective propeller blade solidity [-]
S_{VTP}	VTP area $[\mathrm{m}^2]$
T	Propeller thrust [N]

Notation	Description
T_C*	Thrust coefficient $\left(T/\left(q\cdot S_{wing}\right)\right)$ [-]
θ	Aircraft pitch angle [deg]
ϵ_{TMP}	TMP toe-in angle [deg]
u	Aircraft X-velocity $[\mathrm{m}\cdot\mathrm{s}^{-1}]$
v	Aircraft Y-velocity $[\mathrm{m}\cdot\mathrm{s}^{-1}]$
V_{ind}	Induced velocity $[\mathrm{m}\cdot\mathrm{s}^{-1}]$
$V_{ind_{ax}}$	Axial induced velocity $[\mathrm{m}\cdot\mathrm{s}^{-1}]$
V_{ind_t}	Tangential induced velocity $[\mathrm{m}\cdot\mathrm{s}^{-1}]$
V_∞	Free-stream velocity $[\mathrm{m}\cdot\mathrm{s}^{-1}]$
w	Aircraft Z-velocity $[\mathrm{m}\cdot\mathrm{s}^{-1}]$
ω_n	Eigenmotion natural frequency [-]
X_b	Body frame force in X [N]
X_p	Propeller frame force in X [N]
Y	Propeller normal force [N]
Y_b	Body frame force in Y [N]
Y_p	Propeller frame force in Y [N]
Z_b	Body frame force in Z [N]

Contents

List of Terms and Acronyms v

List of Symbols vii

1 Introduction 1

2 Theoretical Background 5
2.1 Lifting Line . . . 5
2.2 Propeller Forces Calculation Methods. . . . 7
2.3 Tip-mounted Propeller - Wing Interaction . . . 11
2.4 Flight Dynamics . . . 14
2.4.1 Reference Frames . . . 14
2.4.2 Discrete Time-response Simulation . . . 16
2.4.3 Simplified Linearised Eigenmotions . . . 16
2.4.4 Controllability . . . 18

3 Numerical Model Setup 19
3.1 Wing-induced Flow Field . . . 19
3.1.1 Lifting Line Solver Implementation . . . 19
3.1.2 Induced Velocity Verification. . . . 19
3.1.3 CFD Validation. . . . 25
3.2 Propeller Forces with Blade-element Analysis. . . . 29
3.2.1 Evaluation Tool Selection . . . 30
3.2.2 Isolated Propeller Performance . . . 31
3.2.3 Propeller Force Parameter Definition . . . 32
3.3 Implementing Propeller Forces into a Non-linear Flight Mechanics Model . . . 34
3.3.1 Verification by a Trim Analysis . . . 38

4 Analysis of Propeller Force Inputs 39
4.1 Parametric Propeller Force Dataset Visualisation . . . 39
4.2 Assumptions Review . . . 43
4.3 Propeller Forces' Contribution to Control . . . 46

5 Sensitivity Analysis of Stability Contribution 49
5.1 Static Stability Analysis . . . 50
5.1.1 Directional . . . 50
5.1.2 Longitudinal . . . 51
5.2 Dynamic Stability . . . 52
5.2.1 Motion Damping and Frequency Extraction Approach. . . . 52
5.2.2 Dutch Roll . . . 54
5.2.3 Phugoid . . . 58
5.2.4 Short Period . . . 59

6 Typical Stability and Control Contribution Assessment 63
6.1 Static Stability. . . . 64
6.2 Dynamic Stability . . . 66
6.3 Directional Control Comparison . . . 67

7 Conclusion & Recommendations 73

A Propeller Forces Post-processing 75

B Phugoid Sensitivity Analysis (cntnd.) 77

Bibliography 79

1

Introduction

With increasing concern for environmental impact of aircraft, design focus shifts to energy efficiency and noise. To achieve a high propulsive efficiency, air should be accelerated by a small amount. With its large blades, a propeller is capable of accelerating a large area by a small amount. Hence, a propeller is an efficient means of propulsion. This propulsive efficiency can even be enhanced by placing the propeller in the wing-tip vortex. This efficient placement will first be discussed, followed by why this efficient placement is not yet widely incorporated and why it might be in the future. This will lead to the definition of a research gap, followed by a research objective to fill this gap. Finally, a reference aircraft to apply the tip-mounted propellers to is presented that will be used for assessment throughout this thesis.

The Tip-mounted Propeller

Due to its simplicity, as a propeller is basically a rotating wing, early aircraft were driven by propellers. These already had propulsive efficiencies up to 82% [1]. With the rise of jet engines combined with low fuel prices, propeller development stagnated. When fuel prices started to rise in the eighties, development of propellers continued, focussing on interaction with the wing. A propeller leaves behind a swirl, which inherently means an efficiency loss. This should be kept to a minimum. An idea investigated by Snyder and Zumwalt [2] is to position the propeller in front of the wing tip, in such a fashion that the propeller swirl and wing tip vortex cancel each other out. This would then effectively lead to a change in the downwash pattern of the wing. The fashion of propeller rotation (pro or counter-vortex) would then respectively increase or decrease induced drag. Since the trailing vortex is shifted outboard, the effective aspect ratio of the wing is increased [3]. Induced drag reductions can be as high as 30% [4].

The effect of tip-mounted propellers has been modelled numerically and measured experimentally numerous times. Examples include: lifting line models Miranda and Brennan [5], VLM methods [6] and CFD methods [7, 8]. Aerodynamic and aeroacoustic interaction effects for tip-mounted propellers specifically have been researched in an experimental fashion [9], for both tractor and pusher configurations.

An aircraft that has been designed using this tip mounted propulsion concept is the Vought V-173 (see Fig. 1.1). It has flown numerous test flights where many problems were solved, yet was not a success due to continuing vibration problems caused by the propeller gearboxes and interconnecting drive shafts [10]. This shaft was installed so that in case of an engine failure, no asymmetric thrust condition would arise. The shaft connected the two radial engines. To indicate the complexity, and therefore loss in efficiency, reliability and maintenance ease, the system for its successor (Chance Vought XF5U-1) is depicted in Figure 1.2. Such a system (albeit less complex than the XF5U-1 system) is also used by tilt-rotor aircraft that have a larger span than the Vought V-173. One can imagine that for a larger span, hence larger bending moment and larger tip deflection, this system becomes even heavier. For both tilt-rotor and the V-173 the disk loading on the propellers is much lower than for a conventional aircraft. Even though the benefits of tip-mounted propulsion are clear, they have not been implemented on conventional aircraft.

Design Space Enlargement by Electric Propulsion

An important factor that inhibits the implementation of tip-mounted propellers is the moment produced in case of a one-engine-out situation. This resultant moment has to be overcome by for example a triple slotted

[1] https://airandspace.si.edu/collection-objects/vought-v-173-flying-pancake ; Accessed 14-12-2018

Figure 1.1: Vought V-173 "Flying Pancake" [1]

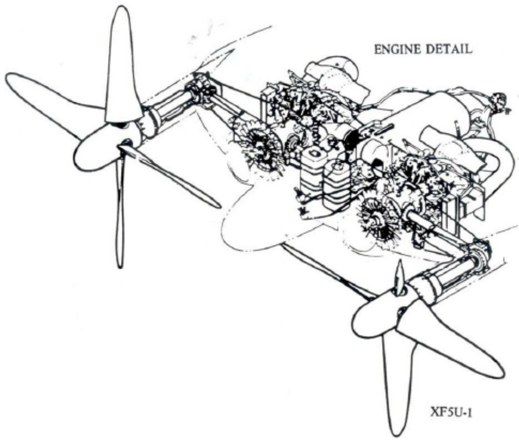

Figure 1.2: XF5U-1 engine detail [10, p. 25]

rudder, or multiple engines on the wing so a one-engine-out situation would be less critical [4]. The last solution requires engine scalability. This can be achieved by applying electric propulsion. Other potential benefits of electric propulsion with respect to jet fuel are listed below, which are exhaustively described by Brelje and Martins [11].

- Carbon emission reduction.
- Cost per unit energy reduction.
- Decoupling fan placement and power source. A fan can be placed on aerodynamically favourable positions to achieve installation drag reduction, high lift augmentation or swirl cancellation, or in positions where noise is shielded more effective. Also, the bypass ratio can be increased [12].
- Engine scalability [13, 14]. Distributed electric propulsion (DEP) concepts are enabled, giving rise to boundary layer ingestion concepts, and leading to less critical engine failures. Therefore total excess thrust (e.g. one engine inoperative climb requirements) and one engine inoperative yawing moment can be decreased [15].
- Energy recuperation [16].

Since conventional constraints are not necessarily valid anymore, a large design space has opened up. Aircraft fuel is around 50 times more energy dense than a battery, making all-electric systems heavy. Using the aforementioned advantages and the large design space weight reductions are still claimed to be possible [17] (using a jet fuel - electric hybrid architecture).

Research from the eighties already suggested to extract rotational energy from the flow around the wing tip using turbines [5, 18]. Power circuits to support recuperation have recently been suggested [16]. Tests employing this concept using a propeller that was optimised for recuperation showed 19% reduction in energy consumption for 1000ft climb and descent manoeuvres, and 27% increase in the number of traffic pattern circuits that could be flown [19].

The commercial viability of personal electric aircraft has been shown by Pipistrel[2], who are producing electric aircraft since 2007. The Alpha Electro model is a double seat trainer for basic circuit training with recuperation abilities. This aircraft allows for 13% of energy recuperation on every approach[3].

State-of-the-art

Challenges that arise from implementing tip-mounted propellers can be split in control and structural challenges. The latter challenge can be solved by using lightweight electric engines. Electric engines also reduce vibrational issues. With respect to control, in a OEI situation both propulsive devices have to be switched off as the resulting moment due to thrust of the operable engine is too large. One could rely on other engines to counter this moment, yet NASA's X-57 (Fig. 1.4) does not as the DEP system is only designed as a high lift device [20]. It relies on a redundant electrical system, so power can always be supplied to the tip engines. If a OEI situation would arise, the advice would be to land as soon as possible, or scale the thrust of

[2] https://www.pipistrel.si/about-us/history ; Accessed 14-12-2018
[3] https://www.pipistrel-aircraft.com/aircraft/electric-flight/alpha-electro/#tab-id-1 ; Accessed 04-03-2019

the remaining engine to 50%, which would yield a torque that can be trimmed by the rudder. The DEP system makes for a $C_{L_{max}}$ of 4.48, without the need of a heavy slotted fowler flap system [20]. This results in a reduction factor of the wing area of 2.5, yielding a high cruise efficiency. Then, the tip mounted engines are the main propulsors, effectively countering the wing tip vortex. Using this configuration a cruise efficiency multiplier of approximately 4.8x better than the stock aircraft (Tecnam P2006T) is expected [21].

Figure 1.3: Agusta Westland AW609 [4]

Figure 1.4: NASA X-57 Maxwell [20]

The large moment resulting from a TMP can also be used for directional control. DEP concepts have proven to be able to remove the need for a vertical tailplane, as for example the Lilium jet [5]. An example of a tilt-rotor aircraft that uses propellers on the tip for directional control is the Agusta Westland AW609, depicted in Figure 1.3. The figure gives a clear view of the vertical tailplane, where no rudder is installed. By changing the pitch of the blades, directional control is obtained. This aircraft does apply a shaft to interconnect the engines.

If tip-mounted engines are not interconnected by a shaft, and wished to be used for directional stability and control, the most stringent case is OEI. The moment introduced by the operational engine is too large to counteract, obliging the operational engine to be switched off.

Research Definition

With the conclusion that synergistic propulsion integration and application should be explored for electric aircraft [11, 13, 22, 23] and the extremely active field of aerodynamic propulsion integration, the question arises whether propulsion can be used for other disciplines. Electric propulsion opens up new design spaces, yet such a system is heavy and therefore relies on synergistic engine placement to compensate the extra mass. More strategies to enhance synergistic performance should be explored. A currently unexplored synergy strategy is to use tip-mounted propellers for directional stability and control. If this is possible, the vertical tailplane can be reduced in size. This will reduce the drag and mass of an aircraft, decreasing the total energy consumption. Furthermore, the aircraft's descent angle can be controlled by recuperating propellers. This leads to the following question for this research:

Can tip-mounted propellers enhance the directional stability and controllability of an aircraft?

To answer this question, four objectives are specified:

1. Develop a program that calculates the forces on a propeller that resides in the wing-tip vortex.
2. Evaluate the static stability contribution of tip-mounted propellers.
3. Simulate the dynamic response to a perturbation of an aircraft fitted with tip-mounted propellers.
4. Compare the time-response of a conventional rudder deflection and a tip-mounted propeller deflection for both positive and negative input power.

[4] https://newatlas.com/agustawestland-aw609-tiltrotor/21466/ ; Accessed 14-01-2020
[5] https://lilium.com/the-jet ; Accessed 14-01-2020

The question and its corresponding solution-strategy can be summarised in the following research objective:

The objective of this research is to investigate the contribution of tip-mounted propellers to directional stability and control by applying propeller forces to an (existing) baseline aircraft.

Piper Seneca III as Baseline Aircraft

This baseline aircraft will be the Piper Seneca III, since a verified and validated flight mechanics model of this aircraft is available in-house [24]. It has been used in for example Ref. [25]. The general parameters of this aircraft are presented in Table 1.1, obtained from [26] except for the airfoil[6]. The Simulink flight mechanics model will be modified to incorporate tip mounted propellers.

Table 1.1: Input parameters Piper Seneca model

Name	Value	Unit
Span	11.86	m
Dihedral	7	deg
Chord	1.63	m
Airfoil	NACA 65-415	-

Whether a pusher or tractor propeller is used does not matter theoretically for the performance of the propeller-wing system [5]. Assuming that the propeller rotates contra-tip-vortex, a tractor configuration mainly enhances wing performance, where a pusher configuration enhances propeller performance. When rotating co-tip-vortex, for example when the propeller is recuperating, in a tractor configuration the wing performance will even degrade. The wing performance is verified and validated in the flight mechanics model, in a non-parametric fashion. Preferably, it should not be changed if that is possible within the scope of the thesis. These two reasons motivate the choice for a pusher propeller configuration.

Designing a tip-mounted propeller aircraft is outside the scope of this research. Therefore, the resultant forces of the propeller are directly applied to the flight mechanics model. This implies that the aircraft is not properly designed. This has no effect on our analysis; the improvement/reduction in stability and control is our focus. This choice does imply that statements about the aerodynamic flight performance of the aircraft (i.e. drag reductions due to tip mounted propellers) can not be made.

A drawing of the altered Piper Seneca is included in Figure 1.5.

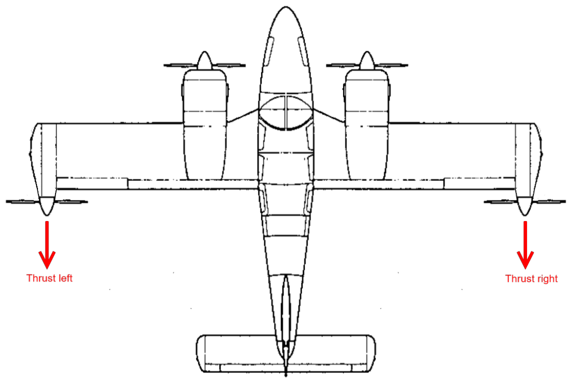

Figure 1.5: Top view artist impression of Piper Seneca III fitted with TMP

First background theory that is used throughout the thesis is presented in Chapter 2. The theory is implemented as a software package in Chapter 3. Resulting forces and its potential applicability to control are studied in Chapter 4. Static and dynamic stability will be evaluated in a parametric fashion in Chapter 5. A potential design is made and evaluated in Chapter 6.

[6] `http://www.aerofiles.com/airfoils.html` ; Accessed 4-12-2019

2

Theoretical Background

In this chapter underlying theory for the rest of this thesis is presented. The thesis focusses on tip mounted pusher propellers and its effect to flight mechanics. First a method to obtain wing-induced velocities is presented, to calculate the input flow field of the propeller. Then the theory of evaluating the forces on a propeller will be described, followed by a discussion on propeller-wing interactions. The chapter will conclude with the set-up of a non-linear flight mechanics model, and a simplified representation of some of its eigenmodes.

2.1. Lifting Line

Forces that act on a wing are pressure and shear due to the velocity and viscosity of air. These can be summed into a resultant force, which can be decomposed into lift and drag, or a normal force and an axial force. This is depicted for an airfoil in Figure 2.1.

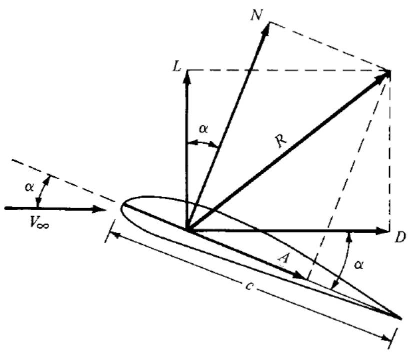

Figure 2.1: Forces on an airfoil [27, p. 20]

The airfoil can be extended into and out of the paper, resulting in a three-dimensional wing. The same forces apply to such a wing. To calculate the forces on this wing, Prandtl's classical lifting-line theory as described by Anderson [27, Ch. 5] is presented here.

A wing can be split into elements. Each element has a vorticity, which can be related to lift as in Equation (2.1) according to the Kutta-Joukowski theorem. This vorticity for each element is depicted in Figure 2.2 by curved arrows, where the wing is represented by a lifting line. Each element has two free trailing vortices which extend from the lifting line to infinity to the right, resulting in a horseshoe vortex. The free trailing vorticity is the difference in vorticity between two adjacent elements of the lifting line.

$$dL = \rho \vec{V}_e \times \vec{\Gamma} dr \tag{2.1}$$

Each of the trailing vortices will induce a flow downward on each of the sections. This is an induced angle of attack, and denoted by α_i in Figure 2.3. This induced angle of attack will reduce the local vorticity of the

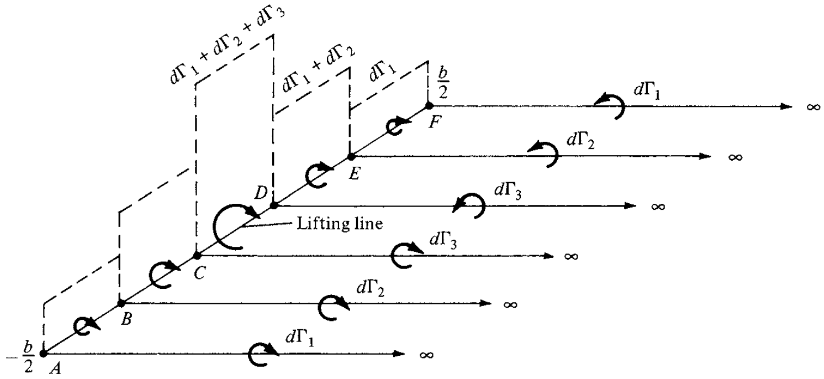

Figure 2.2: Vorticity distribution for a finite amount of horseshoe vortices [27, p. 426]

section. This in turn will alter the strength of the section's trailing vortices, which in turn will have an effect of the induced angle of attack. The induced velocity from any vortex line can be calculated using Equation (2.2).

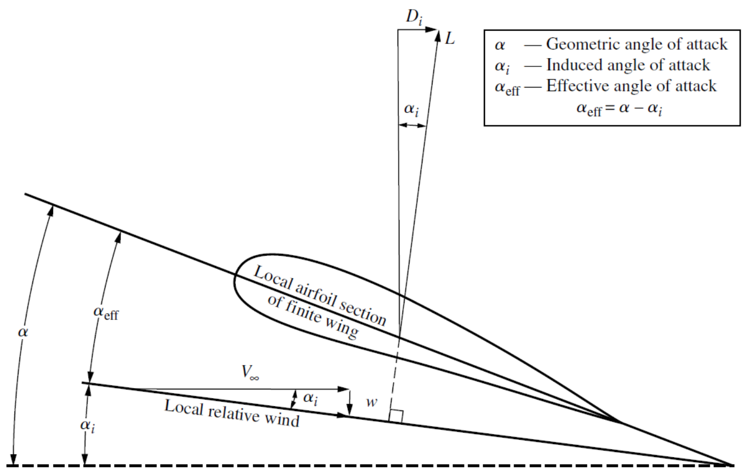

Figure 2.3: Effect of downwash on the angle of attack [27, p. 417]

$$\vec{v} = -\int \frac{\Gamma}{4\pi} \frac{d\vec{s} \times \vec{r}}{|\vec{r}|^3} \tag{2.2}$$

If the inflow to the wing is symmetric, some simplifications can be made. The downwash, denoted by w in Figure 2.3, which is responsible for the reduction in angle of attack, can be obtained from Equation (2.3). This can be converted to an induced angle of attack by Equation (2.4).

$$w(y_0) = -\frac{1}{4\pi} \int_{-b/2}^{b/2} \frac{\left(d\Gamma/dy\right) dy}{y_0 - y} \tag{2.3}$$

$$\alpha_i\left(y_0\right) = -\frac{w\left(y_0\right)}{V_\infty} \tag{2.4}$$

Now that the relation of the trailing vortices' strength on α_i, and the relation of α_i on the vorticity of the trailing vortices is defined, the system can be solved. For an analytical solution, the number of elements can be increased to infinite for a continuous vorticity distribution. For numerical applications an approximation with a large number of elements would suffice. The amount of sections that is needed for an accurate result depends on the wing, and has to be determined experimentally by a convergence study.

Now the total lift of the wing can be obtained by summing the lift contributions of all elements. The drag can be calculated using the downwash at the wing, i.e. the lifting line location. The downwash leads to an angle of α_i between the free-stream velocity V_∞ and the local relative wind. Since the lift is perpendicular to the local relative wind, the lift force is tilted by α_i as well. This tilting of the lift vector leads to the induced drag D_i. For clarification, this drag force D_i is depicted in Figure 2.3.

It is now known how the lifting line theory evaluates the performance of an arbitrary wing. The process presented here has excluded implementation details; these are described in more detail by Anderson [27, Sec. 5.3]. For a method to analyse an arbitrary wing with non-linear lift slope using the lifting line method, the reader is referred to Ref. [27, Sec. 5.4].

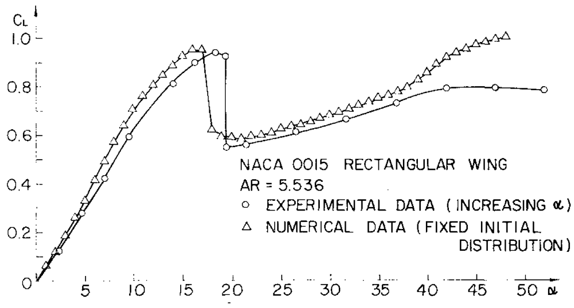

Figure 2.4: $C_L - \alpha$ plot of numerical results with fixed initial distribution and experimental results [28]

The theory presented above has been validated for the resulting lift in Ref. [28]. Figure 2.4 is presented here to illustrate the agreement between theory and experiments. One can see that the numerical values for this NACA 0015 rectangular wing the results are within 10% of the experimental values.

In the same fashion as the vorticity distribution of the wing is used to calculate the downwash at each of the sections, the system of vortices can be used to evaluate the direction and magnitude of the flow in any point of space. This can be done by applying Equation (2.2) to each of the vortex lines. If the induced velocity is evaluated for every point of a propeller disk, the inflow field of the propeller is determined and can be used for further analysis. This approach does neglect the influence of the propeller on the wing lift distribution.

The approach used by Anderson [27] limits the wing to be a straight line. If a wing would have a dihedral angle, or any sweep, the method could not be used. An adaptation to this method can be found in Ref. [29], where the influence of the neighbouring lifting line sections' vorticity is taken into account when evaluating the local α_i. The method is then applicable to both dihedral and sweep, where the lift coefficient of highly swept back wings (45 deg) is in agreement with experimental data. The drag coefficient however is more accurate than other methods as a panel method, yet over-predicts the drag by 25%, where the error was minimal for a straight wing. This method is implemented in the remainder of this thesis, adding the possibility of evaluating a wing with dihedral and/or moderate sweep with high accuracy.

2.2. Propeller Forces Calculation Methods

A propeller uses two or more rotating blades. These blades can be viewed as wings; each blade has a lift and a drag force. The forces of each blade combined result in a thrust force and a torque if the flow is parallel to the rotation axis. If this is not the case, in general one could say there would be forces and moments in all three axes. The propeller moments are small in comparison to the moments of an aircraft, and will therefore not be treated in detail [6]. The forces and moment that should be taken into account are depicted in Figure 2.5. These are:

- Thrust force, can be used for yaw control on tip mounted engines
- Normal force, has an influence on the lift coefficient and potentially rolling moment
- Torque, key driver for power consumption

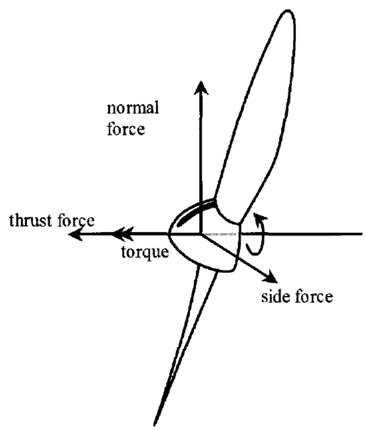

Figure 2.5: Most important forces and moments acting on a propeller [6]

In this research a propeller will be used when generating thrust, yet also when generating negative thrust, hence drag. This is a propeller that can be compared with a wind-mill, i.e. extracting energy from the airflow.

To understand how a propeller is evaluated, first actuator disk theory is presented. This is a momentum theory that does not take into account the

blade shape. This will then be combined with blade-element momentum
theory describes how the blade shape determines the performance. Finally, vortex theory describes the wake of the propeller, from which a more accurate expression of the drag can be derived.

Actuator Disk

Actuator disk theory is the basis theory of the propeller. It is profoundly described in numerous text books and articles, so only the assumptions and outcome will be stated here. The assumptions are as follows (McCormick [30]):

- The thrust loading is uniform over the propeller disk. This implies the limiting case of an infinite number of blades.
- There is no rotation imparted to the flow. This would be approximated by a pair of counterrotating propellers.
- A well-defined slipstream separates the flow passing through the propeller disk from that outside the disk.
- Far ahead of/behind the propeller disk the static pressure in and out of the slipstream is equal to the undisturbed free-stream static pressure.

The propeller and its slipstream inside a control surface is depicted in Figure 2.6. When applying conservation of momentum, using the difference of momentum flux in and out, one arrives at Equation (2.5) for the propeller thrust. The theoretical power needed for this acceleration of fluid can be obtained from conservation of kinetic energy.

$$T = \rho \pi r^2 V_2 (V_2 - V_0) \tag{2.5}$$

This theory gives insight in theoretical ideal propeller performance, as this can be used for ideal efficiencies and thrust variance with forward speed approximations. The theory does not depend on the propeller used; It assumes an infinitely thin actuator disk that does nothing but increase the total pressure of the flow across the disk. Therefore, for specific propeller performance evaluation the theory should be extended with some propeller characteristics. For more information on actuator disk theory, the reader is referred to Refs. [30–32].

Blade-Element Momentum Theory

In order to analyse the propeller itself, its geometry must be analysed. From this geometry, one can split the propeller into finite elements, calculate the performance of all sections and sum them together. This can be done with the following assumptions.

- The blade is split up into aerodynamically independent strips.
- Only axial and angular velocity components exist.

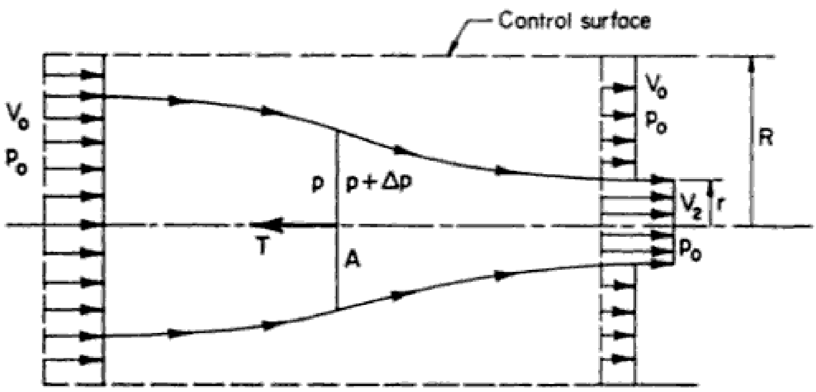

Figure 2.6: Idealised propeller model for classical momentum theory [30]

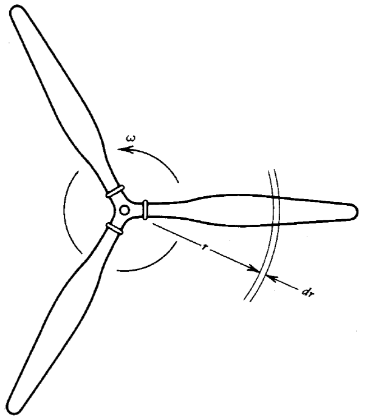

Figure 2.7: Blade element indication on propeller [33, p. 348]

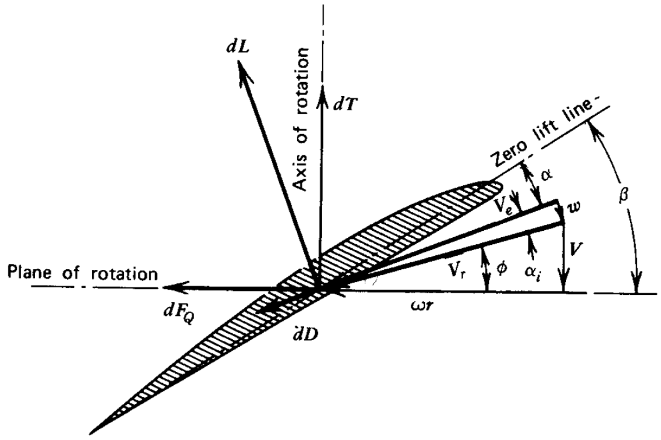

Figure 2.8: Blade element section forces and velocities [33, p. 348]

Blade element momentum theory splits a blade into elements. Such an element is illustrated in Figure 2.7, at radius r with width dr. The forces and velocities acting on such an element are depicted in Figure 2.8, and will be described below.

These elements (airfoils) have their own lift and drag characteristics, indicated with dL and dD. These should be calculated or measured, and tabulated. For each element, the local angle of attack is calculated and its element's performance evaluated. These can then be summed over the span and multiplied by the amount of blades, and a total propeller performance results. This idea was first described by Drzewiecki [34].

When a propeller has no forward velocity, there is still air moving through the propeller. In the theory as described above, there is no explanation for that. This problem can be solved when combining the blade element and momentum theories, as is most likely first done by Orville and Wilbur Wright [1]. When using this approach induced axial and tangential velocities need to be solved for. This induced velocity is indicated by w in Figure 2.8. As the effective angle of attack for the airfoil is reduced by the induced velocity, aforementioned lift and drag characteristics are altered. The characteristics corresponding to the effective angle of attack need to be obtained from the aforementioned tabulated values, which leads to a new induced velocity. This process needs to be repeated until a solution is found.

This method does not take the loss of lift at the blade tips into account. One way to incorporate this effect is to either neglect the outboard 3-5% of the blade, or force the lift to zero at the tip using some tip correction [35]. Furthermore, if angular momentum is taken into consideration, the slipstream rotation can be modelled.

For a more detailed explanation and implementation-ready equations the reader is referred to text books as written by Theodorsen [31] and McCormick [30, 33].

Combined Blade-Element Momentum Vortex Theory

At the basis of the vortex theory for propellers is Prandtl's classical lifting-line theory, as described in Section 2.1. This theory assumes that a wing can be split in elements that have their own circulation and two trailing vortices. When these are all summed, this leads to a lift of the wing and an induced drag due to the downwash. This theory was extended for ideal propellers by Goldstein [36] by solving a potential flow problem of a helix immersed in a uniform stream.

When applying the lifting line theory to a propeller, a helicoidal vortex sheet will form since the propeller is a rotating wing. An illustration can be found in Figure 2.9. The trailing blade vortex sheet is indicated right behind the propeller. In the far-field this sheet will have rolled up into a set of tip vortices and a central vortex in opposite direction as indicated, yet this is not accounted for in the numerical analysis as its influence is small.

As an elliptically loaded wing passes through the air, the resulting far-field wake is a line moving down. The same holds for an ideally loaded propeller, only in a helicoidal form as described by Wald [32]. In other words, if the propeller is ideally loaded, the wake sheet will not deform, hence the trailing blade vortex sheet from Figure 2.9 will remain as-is. This can be formulated in a potential function. Goldstein found a solution to this potential problem, and tabulated his results [36]. Prandtl devised an approximate solution to the potential flow problem, which became known as the "tip loss factor". Especially for lower advance ratios and

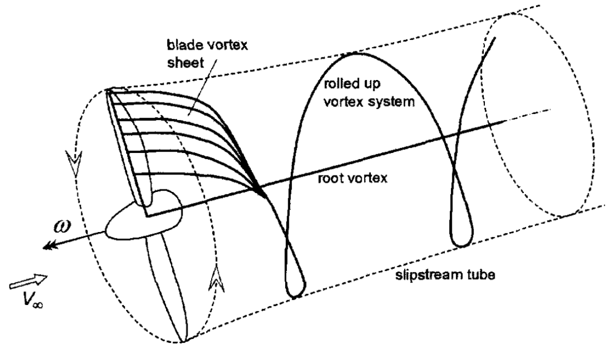

Figure 2.9: Helicoidal trailing vortex sheet [6, p. 17]

a higher blade number it is a good approximation.

If the ideal propeller assumption is not valid, the wake will deform, as all radial stations of the propeller do not necessarily have the same downwash velocity. This would imply that the blade vortex sheet drawn in Figure 2.9 would not be valid anymore. However, if one assumes that for every radial station the trailing vortex sheet does not deform, performance calculations on the propeller are still possible. When compared to experiments, this assumption appears to be valid [37]. As with the original lifting-line method, an iterative method is used to solve for the downwash at each radial station.

For the full solution procedure the reader is referred to the works of Wald [32], where methods for ideal propeller design, off-design performance and interaction with other bodies are given. It must be stated that his work is rather complete, yet extremely compact.

Empirical Non-axial Inflow Effect Estimation

The theory mentioned above is not necessarily applicable to account for non-axial inflows. Certainly, at each of the blade elements a velocity component can be added by assuming the flow will flow in at the same angle as the general angle of attack of the free-stream. Whether this is true still has to be validated.

Another way of obtaining the propeller thrust and normal force is by applying empirical relations by De Young [38] based on the works of Ribner [39]. The equations formulated in these papers are obtained from the method described above, hence propagating free-stream velocity correction angles through a theoretical propeller model. This method will give a mathematical proportionality relation, where a scaling factor is still needed. The scaling factor is then determined empirically, leading to the following equations. The accuracy is good, especially for angles of attack smaller than 30%. After this point divergence occurs, depending on the blade shape. As the method is an empirical one, the normal and thrust force trends of an propeller subjected to an angle of attack are captured. For this thesis, where the thrust and normal force variations of a propeller with non-axial inflow should be modelled accurately, the method is applicable. Yet if the highest accuracy of the resulting forces is wished for, one should either follow the method proposed and determine the statistical parameters for that exact propeller, or divert to some other more accurate method.

First of all, the following relations use imperial units. The exact definitions and units of the symbols can be obtained from Ref. [38]. The thrust force and power of the propeller due to some propeller angle of attack α_p are determined by Equations (2.7) and (2.8). Key parameters are the advance ratio's for zero thrust and zero power, the blade pitch β_p, the propeller angle of attack with respect to the free-stream α_p, and the effective blade solidity σ_e. The zero thrust and zero power advance ratio's can either be determined experimentally or by empirical relations. σ_e follows from geometrical relations of the blade, and depends on the span wise chord distribution, the diameter and the number of blades.

$$\sigma_e = \frac{\bar{b}'}{b'_{0.75}} \left(\frac{4R}{3\pi} \frac{b'_{0.75}}{D} \right) \tag{2.6}$$

$$\begin{aligned} \frac{C_T(\alpha_p, J\cos\alpha_p)}{C_T(0, J\cos\alpha_p)} = 1 + \frac{3(J\cos\alpha_p/J_{0T})^2}{4\left(1-\left(J\cos\alpha_p/J_{0T}\right)\right)} \sin(\beta_p+5)\Big[\tan(\beta_p+5)+ \\ \sigma_e\left(1+\left(1+(2/\sigma_e)\tan(\beta_p+5)\right)^{1/2}\right)(1-\cos\alpha_p)\Big]\tan^2\alpha_p \end{aligned} \tag{2.7}$$

$$\frac{C_P(\alpha_p, J\cos\alpha_p)}{C_P(0, J\cos\alpha_p)} = 1 + \frac{3(J\cos\alpha_p/J_{0P})^2}{4\left(1-\left(J\cos\alpha_p/J_{0P}\right)\right)}\sin(\beta_p+5)\left[\tan(\beta_p+5)+\right.$$
$$\left.\sigma_e\left(1+\left(1+(2/\sigma_e)\tan(\beta_p+5)\right)^{1/2}\right)(1-\cos\alpha_p)\right]\tan^2\alpha_p \quad (2.8)$$

In the following equations a prime, e.g. $T_{C'}$, denotes that the coefficient is nondimensionalised with respect to free-stream conditions and the propeller disk area, hence dividing by $q\cdot\pi\cdot(D/2)^2$. If a coefficient denotes no prime, as C_Y, the coefficient is nondimensionalised by the propeller properties as $\rho n^2 D^4$. The propeller normal force Y can be obtained from (2.9).

$$\frac{C_Y(\alpha_p, J\cos\alpha_p)}{C_{Y_{\alpha_p}}(0, J\cos\alpha_p)} = \tan\alpha_p \quad (2.9)$$

$$C_{Y'_{\alpha_p}} = \frac{4.25\sigma_e}{1+2\sigma_e}\sin(\beta_p+8)\left(1+\frac{3T_{c'}}{8\left(1+\frac{2}{3}T_{c'}\right)^{1/2}}\right) \quad (2.10)$$

This method only takes into account a single propeller angle of attack. It is inherently a 2D method. Since the method will be used in a 3D problem, velocities should be compiled to a single magnitude and an inflow angle, and the output decomposed again.

Sense of rotation

One should note that when the propeller advance ratio progresses into the wind-milling region (where the local angle of attack on the blade becomes less than 0°) the rotation direction of the wake reverses. So if the propeller is delivering thrust and the swirl direction is counter-tip-vortex, then when the propeller is recuperating the swirl direction will be co-rotating with the tip vortex [5]. This means that induced drag will be increased, which is detrimental to the energy efficiency of the aircraft. A possible solution could be to rotate the blades in such a fashion that the propeller will start turning in the opposite sense; the angle of attack once again becomes positive. For clarity, Figure 2.10 depicts this process. Since this is a feasibility study both positive and negative angle of attack should be researched. Practical implications as a system that is able to rotate a blade for such a large angle and flight mechanics during transition of propeller rotation direction are left for future research.

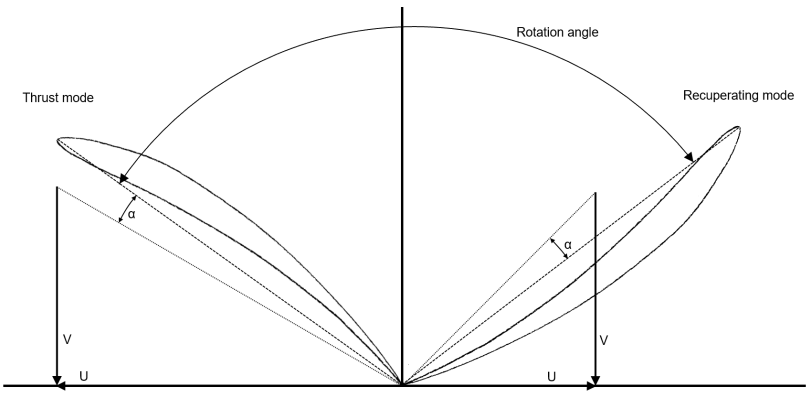

Figure 2.10: Propeller blade rotation for maximum efficiency

2.3. Tip-mounted Propeller - Wing Interaction

For the sake of completeness, let us briefly review the general tip-mounted propulsion theory. As a propeller leaves a helical vortex as wake this inherently means an efficiency loss. The rotational loss might be recovered using swirl recovery vanes [40], or counter this tip vortex by creating another vortex in opposing direction. The most prominent vortex on an aircraft is its tip vortex, which might be (partially) compensated by the propeller swirl. In this section we will focus on the propeller-wing interaction, how it has been modelled in previous research and the effect of a pusher propeller on the wing lift distribution.

The simplest method the author was able to find is presented in Ref. [5], where the wing is modelled as an elliptically loaded lifting line, and the tip-mounted rotor modelled as an elliptically loaded vorticity tube. Still, numerical results showed the same trend as the experimental results, and are surprisingly accurate considering the aforementioned assumptions. Their comparison of experimental NASA results and their numerical results can be found in Figure 2.11. Numerous assumptions and simplifications were made, starting with assuming that the propeller and wing load distributions are ideal, yet the theoretical results have the same trend as the experimental results. By the definition of the vorticity tube as propeller, the location of the propeller was irrelevant.

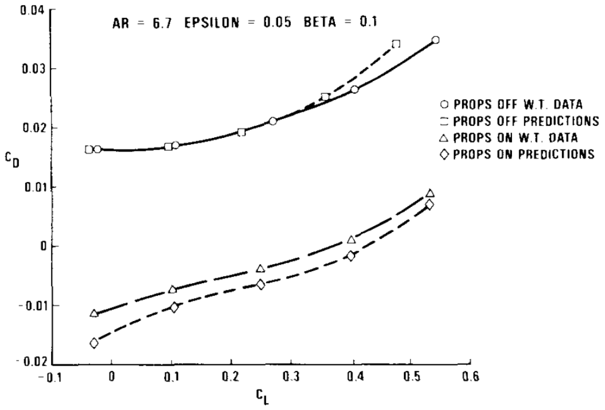

Figure 2.11: Comparison of experimental and numerical results of ideal tip mounted propulsion model [5]

Let us now continue with some well-known propeller-wing interaction works at the TU Delft. Aerodynamic interaction effects between a tractor propeller and wing have been tested experimentally and compared to numerical results from a vortex lattice method (VLM), a panel method and RANS simulations by Veldhuis [6]. The VLM calculation already appears to accurately predict the overall propeller-wing combination performance. When specific small scale interaction effects are needed, RANS simulations show very accurate results. This research led to an optimisation scheme to optimise the coupling between a tractor propeller and wing if the spanwise position of the engine was already chosen. Interaction effects for tip mounted propellers specifically have been researched in an experimental fashion by Sinnige [9]. The focus of this research was on aerodynamic and aeroacoustic interaction effects, for both tractor and pusher configurations. It should be noted that this research is not intended as a comparative analysis between pusher and tractor configurations. This was used as validation data of numerical methods by Stokkermans et al. [8]. Different models were used and compared for propeller and wing, resulting in an accurate RANS CFD model that is capable of modelling the performance of a wing tip mounted tractor propeller. Sinnige et al. [41] continued with an experimental campaign to gain more insight into the aerodynamic interaction effects of tip-mounted propellers for tractor configuration. This was done by local force measurements and flow field evaluations. Furthermore, a validation dataset is provided. Latest research also focusses on the negative thrust regime, where a tractor propeller is evaluated experimentally and numerically, by Sinnige et al. [42].

Tractor propeller

A tractor propeller is positioned upstream of its support. This configuration has numerously been researched, as for example in Refs. [2, 3, 6, 9, 41, 43]. Its key interaction effects are listed in Table 2.1. Each interaction effect has a consequence, which is relevant to some index. From this table the performance aspects are of interest for the research. A schematic overview of the altered lift distribution and interaction of vortices is given in Figure 2.12. With respect to numerical analysis by lifting line, especially the slipstream wash is a very complex point when taking yaw angles into consideration: this will lead to asymmetric loading conditions and might prove to be not negligible. Furthermore, recent research shows that in this tractor configuration, the wing performance is significantly reduced when recuperating [42].

Table 2.1: Key tip mounted tractor propeller-wing interaction effects [9, p. 21]

Interaction effect	Consequence	Relevance
Slipstream wash	Lift augmentation	Increased performance
	Scrubbing drag	Decreased performance
	Separation delay (low Re)	Increased performance
Swirl recovery	Induced-drag reduction	Increased performance
Tip-vortex attenuation	Induced-drag reduction	Increased performance
Slipstream impingement	Unsteady wing loading	Increased vibrations
Blockage and upwash	Unsteady propeller loading	Increased Noise

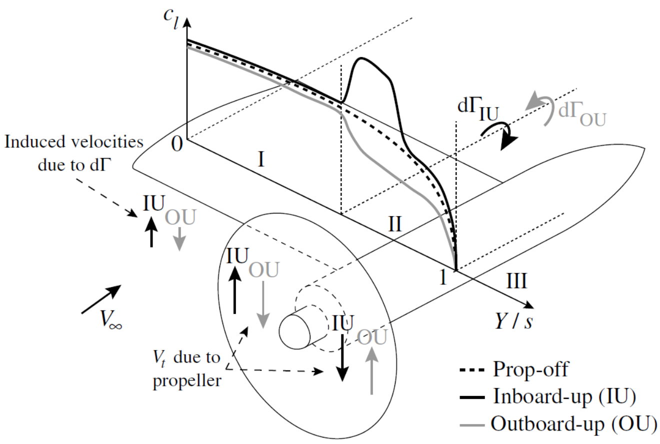

Figure 2.12: Lift-distribution variation due to shed vorticity [41]

Table 2.2: Key tip mounted pusher propeller-wing interaction effects [9, p. 26]

Interaction effect	Consequence	Relevance
Wake impingement	Unsteady propeller loading	Increased noise
Tip-vortex recovery	Propeller power reduction	Increased performance
Propeller suction	Unsteady pylon loading	Increased vibrations
	Separation delay	Increased performance
	Drag penalty (high-speed)	Decreased performance

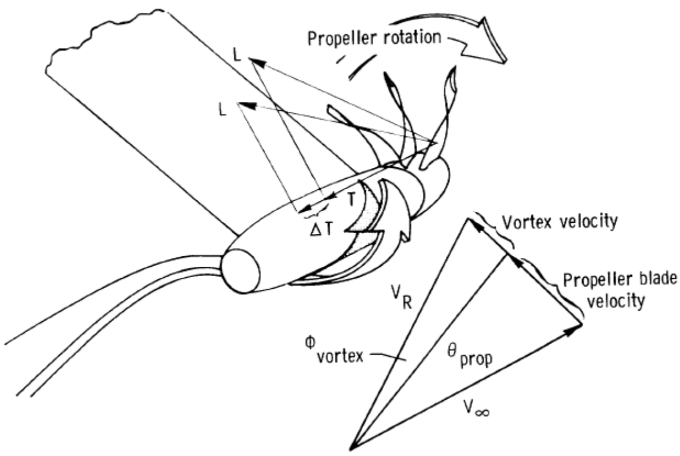

Figure 2.13: Schematic overview of wing tip vortex and propeller [44, p. 12]

Pusher propeller

Numerous studies into the pusher configuration are conducted as well, as in Refs. [4, 7, 9, 44]. A schematic overview of the interaction between tip vortex and the propeller is given in Figure 2.13. One can see the increase in local blade angle of attack, leading to a more forward tilted lift vector, causing more thrust for the same amount of power input. Hence, the same amount of thrust can be produced for less power. In Table 2.2 the interaction effects of the pusher propeller are given. The main penalty of using a pusher configuration is its noise increase. For low thrust loading this noise penalty could be as severe as 24 dB [9].

The performance aspects are once again of importance for this research. Wake impingement effect (responsible for the noise penalty) on time-averaged performance is negligible [9, ch. 8]. In this case, rotational flow can be readily modelled using the methods as described in Section 2.2. The propeller suction, which alleviates the adverse pressure gradient at the trailing edge, has been documented for different pusher propeller positions on a 2D wing (wall-to-wall wind tunnel test) [45]. Furthermore, this research suggests that for a take-off thrust setting the increase in c_l is only 0.2 of the affected wing area for the most favourable interaction position, where the largest effect of the propeller suction was on the trailing edge of the wing.

In this research, the propeller will provide drag forces and thrust forces. A tractor configuration significantly degrades the performance of the wing when the propeller is recuperating. A pusher configuration will lead to increased noise, and has a small effect on the wing performance. Since the effects of the propeller forces on directional stability and control are wished to be known, where an increase in noise does not affect our ability to answer the research question, a pusher configuration is chosen for this research. This implies that the effect of the wing-induced flow-field must be taken into account, and that the effect of the propeller on the wing can be neglected.

2.4. Flight Dynamics

Forces and moments act on the aircraft. These have an influence on the motion of the aircraft. In this section a theory is presented to calculate the motion of an aircraft when subjected to some force and moment, and to keep track of the aircraft in space. This theory is then linearised, to obtain information on what parameters determine the eigenmotion behaviour of the aircraft.

2.4.1. Reference Frames

In this thesis, four reference frames will be used. First, the body-fixed reference frame which is depicted in Figure 2.14. The centre is located at the quarter chord point of the wing, located at its MAC. The X-axis is aligned with the nose of the aircraft, the Y-axis is directed to the right wing and the Z-axis is downward, aligned with the symmetric plane. Inflow angles angle of attack (α) and side slip angle (β_s) are also indicated in the figure. The state of the aircraft is defined in the body-fixed frame. Hence, u, v, w are the X, Y and Z velocities in the body-fixed frame, and p, q, r are the X, Y and Z angular velocities in the body-fixed frame.

Figure 2.15 denotes the definitions of the lifting line reference frame (LL) and the propeller reference frame (p). The body reference frame is also indicated with its orientation, as just explained the centre of the body-fixed reference frame is at the quarter chord of the MAC line. In this figure it is drawn at the same point as the propeller reference frame, to indicate the definition of the toe-in angle ϵ_{TMP}.

For the lifting line reference frame, the X-axis points toward the tail of the aircraft, the Y-axis is aligned with the body-fixed Y-axis, and the Z-axis is upward in the plane of symmetry. The propeller reference frame's Z-axis is aligned with the body-fixed Z-axis, yet the X- and Y-axis of the propeller reference frame are rotated by ϵ_{TMP}, which is defined as a counter-clockwise rotation on the right wing tip. On the left wing tip, it is defined as a clockwise rotation. Hence, a positive toe-in angle rotates both propellers inwards.

The last reference frame is the 2D propeller reference frame. It is used to apply the empirical non-axial inflow equations from the previous section. The reference frame is depicted in Figure 2.16. The thrust T is aligned with the rotational axis of the propeller, and the normal force Y is normal to that. The angle between the inflow and the rotational axis is the propeller angle of attack α_p.

Rotating back and forth between these reference frames is done using Euler angles and their corresponding transformation matrices. This matrix complies with the following Equation (2.11), where $\mathbb{T}_{21}$ is the transformation matrix.

$$\begin{bmatrix} v_x^2 \\ v_y^2 \\ v_z^2 \end{bmatrix} = \mathbb{T}_{21} \begin{bmatrix} v_x^1 \\ v_y^1 \\ v_z^1 \end{bmatrix} \tag{2.11}$$

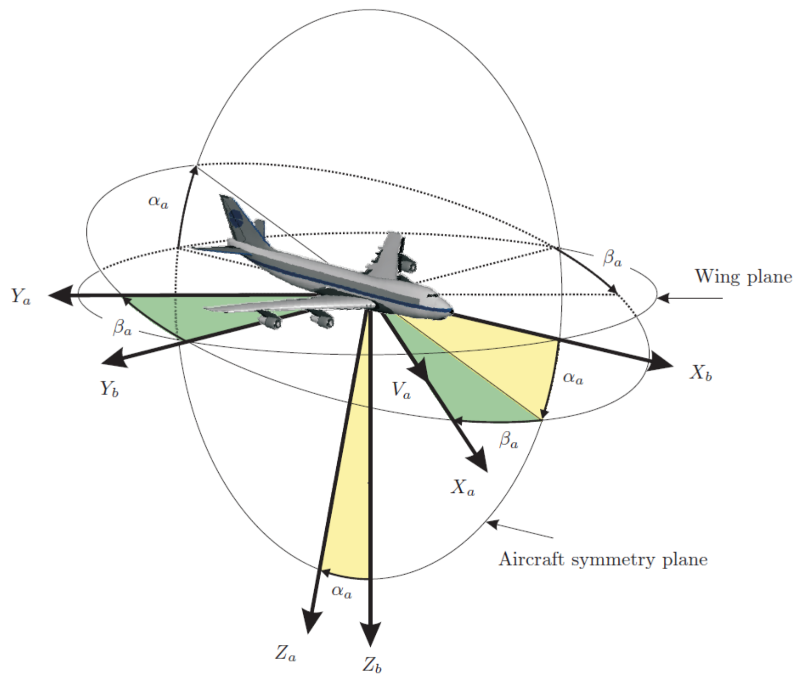

Figure 2.14: Body-fixed reference frame definition [46]

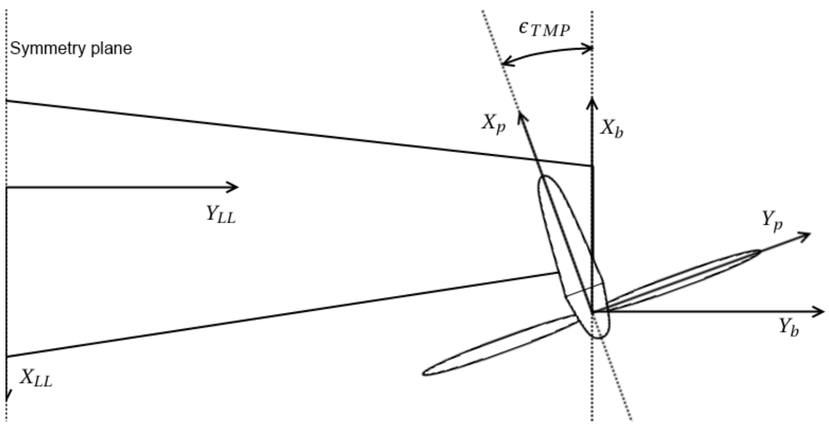

Figure 2.15: Lifting Line (LL) and Propeller (p) reference frame definition

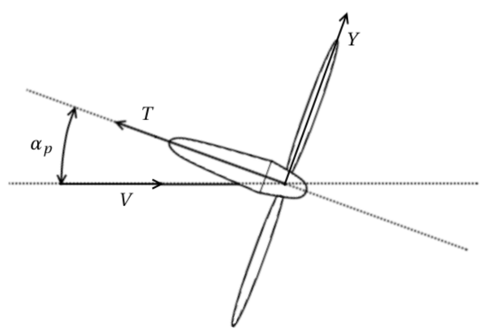

Figure 2.16: 2D propeller reference frame definition

This matrix is composed of three rotations, multiplied with each other. The matrix depends on the order of rotation. So, if the rotation is as $\phi_z \to \phi_y \to \phi_x$, one should multiply Equations (2.12) - (2.14) in that order. ϕ is in this case the right-handed rotation angle over that axis, and the shown rotation matrices are valid for a right-handed axis system.

$$\mathbb{T}_x = \begin{bmatrix} 1 & 0 & 0 \\ 0 & \cos\phi_x & \sin\phi_x \\ 0 & -\sin\phi_x & \cos\phi_x \end{bmatrix} \tag{2.12}$$

$$\mathbb{T}_y = \begin{bmatrix} \cos\phi_y & 0 & -\sin\phi_y \\ 0 & 1 & 0 \\ \sin\phi_y & 0 & \cos\phi_y \end{bmatrix} \tag{2.13}$$

$$\mathbb{T}_z = \begin{bmatrix} \cos\phi_z & \sin\phi_z & 0 \\ -\sin\phi_z & \cos\phi_z & 0 \\ 0 & 0 & 1 \end{bmatrix} \tag{2.14}$$

2.4.2. Discrete Time-response Simulation

The implemented flight mechanics model has a discrete time step. This means that the forces and moments acting on the aircraft are evaluated at every point in time, from which accelerations are obtained and propagated throughout the model. With this information, the next point is calculated. The cycle then repeats. This is mathematically stated for a 3D space in Equation (2.15). Here, a, v, r respectively denote acceleration, velocity and the position. α, ω, θ respectively denote the angular acceleration, velocity and position.

$$\begin{aligned} \vec{a} &= \vec{F}/m \\ \vec{v} &= \vec{v_{old}} + \vec{a}\Delta t \\ \vec{r} &= \vec{r_{old}} + \vec{v}\Delta t \\ \vec{\alpha} &= \vec{M}/\vec{I} \\ \vec{\omega} &= \vec{\omega_{old}} + \vec{\alpha}\Delta t \\ \vec{\theta} &= \vec{\theta_{old}} + \vec{\omega}\Delta t \end{aligned} \tag{2.15}$$

The Piper Seneca model is implemented into Simulink in this fashion. This will lead to accurate motion simulations if the time step is small enough. Unfortunately, this method does not give any insight into the motions in advance. The model, in this case, behaves as a 'black box'. Inputs go in, and some time-response follows as output.

2.4.3. Simplified Linearised Eigenmotions

To gain an insight into the behaviour of the model, a model can be linearised. This means that one assumes that deviations from the original state can be calculated in a linear fashion. A linearisation procedure for an aircraft is done in Ref. [46]. First the equations of motion for the aircraft are obtained, followed by obtaining the derivatives of the states with respect to its inputs. These can then be written in a matrix form. Since the linearised equations will not be used in the thesis, except to help understand what parameters are important in the eigenmotions, only the assumptions and the output matrix are shown here. For the full linearisation procedure and state-space discussion, the reader is referred to Ref. [46].

The linearisation assumptions used in the method are stated below.

- The vehicle is a rigid body
- The vehicle does not vary in mass
- The earth is flat
- The earth does not rotate
- The body-fixed reference frame is chosen in such a way that I_{xy} and I_{yz} are zero
- Effects of rotating masses are neglected

The linearised asymmetric equations of motions are given in Equation (2.16). The symmetric version is given in Equation (2.17). From the left-hand matrices eigenvalues can be obtained, leading to the eigenmotions. Subscripts denote derivatives, so for example C_{X_u} denotes the nondimensional force in X, differentiated with respect to u. μ, K and D denote mass, inertia and time-differentiator respectively.

$$\begin{bmatrix} C_{Y_\beta}+\left(C_{Y_{\dot\beta}}-2\mu_b\right)D_b & C_L & C_{Y_p} & C_{Y_r}-4\mu_b \\ 0 & -\frac{1}{2}D_b & 1 & 0 \\ C_{l_\beta} & 0 & C_{l_p}-4\mu_b K_X^2 D_b & C_{l_r}+4\mu_b K_{XZ} D_b \\ C_{n_\beta}+C_{n_{\dot\beta}}D_b & 0 & C_{n_p}+4\mu_b K_{XZ} D_b & C_{n_r}-4\mu_b K_Z^2 D_b \end{bmatrix} \begin{bmatrix} \beta \\ \phi \\ \frac{pb}{2V} \\ \frac{rb}{2V} \end{bmatrix} = \begin{bmatrix} -C_{Y_{\delta_a}} & -C_{Y_{\delta_r}} \\ 0 & 0 \\ -C_{l_{\delta_a}} & -C_{l_{\delta_r}} \\ -C_{n_{\delta_a}} & -C_{n_{\delta_r}} \end{bmatrix} \begin{bmatrix} \delta_a \\ \delta_r \end{bmatrix} \tag{2.16}$$

$$\begin{bmatrix} C_{X_u}-2\mu_c D_c & C_{X_\alpha} & C_{Z_0} & C_{X_q} \\ C_{Z_u} & C_{Z_\alpha}+\left(C_{Z_{\dot\alpha}}-2\mu_c\right)D_c & -C_{X_0} & C_{Z_q}+2\mu_c \\ 0 & 0 & -D_c & 1 \\ C_{m_u} & C_{m_\alpha}+C_{m_{\dot\alpha}}D_c & 0 & C_{m_q}-2\mu_c K_Y^2 D_c \end{bmatrix} \begin{bmatrix} \hat{u} \\ \alpha \\ \theta \\ \frac{q\bar{c}}{V} \end{bmatrix} = \begin{bmatrix} -C_{X_{\delta_e}} & -C_{X_{\delta_t}} \\ -C_{Z_{\delta_e}} & -C_{Z_{\delta_t}} \\ 0 & 0 \\ -C_{m_{\delta_e}} & -C_{m_{\delta_t}} \end{bmatrix} \begin{bmatrix} \delta_e \\ \delta_t \end{bmatrix} \tag{2.17}$$

Eigenmotions in the asymmetric equation are two aperiodic modes, the heavily damped aperiodic rolling motion and the aperiodic spiral motion, and one periodic mode which is the Dutch roll. From these three only the Dutch roll motion will be discussed here, as TMPs will have a large influence on this motion, and requirements on this motion are strict. The rolling motion is of little interest, since the propellers will not be used for roll. General eigenmotions for the symmetric equation are the short period oscillation and the phugoid oscillation.

Heavily simplified state-space systems will now be used to obtain the most important parameters for each of the motions. The assumptions to obtain this solution will be stated, along with equations to obtain the damping factor ζ and the natural frequency ω_n. As said before, these simplified formulas will only be used briefly to discuss the most important parameters affecting each motion. Therefore the full derivation of these simplified equations are not stated. The full derivation can be found in Ref. [46, Ch. 5 & Ch. 6].

Dutch roll

The Dutch roll is a motion where the aircraft sideslips, yaws and rolls. The motion can be approximated by assuming that the aircraft does not roll in this motion, as the involvement of roll in the Y and N equations is small. Hence, $\phi = \frac{pb}{2V} = 0$. This leaves the state-space system as in Equation (2.18).

$$\begin{bmatrix} C_{Y_p}-2\mu_b D_b & -4\mu_b \\ C_{n_p} & C_{n_r}-4\mu_b K_Z^2 D_b \end{bmatrix} \begin{bmatrix} \beta \\ \frac{rb}{2V} \end{bmatrix} = \vec{0} \tag{2.18}$$

The eigenvalues can then be written as in Equations (2.19) and (2.20). From this linearised version the parameters C_{n_β} and C_{n_r} are the most important, and C_{Y_β} is involved as a second order parameter.

$$\zeta = \frac{\sqrt{2}\left(2K_Z^2 C_{Y_\beta}+C_{n_r}\right)}{4\sqrt{K_Z^2\left(C_{Y_\beta}C_{n_r}+4\mu_b C_{n_\beta}\right)}} \tag{2.19}$$

$$\omega_n = \frac{V}{4b}\sqrt{2\frac{C_{Y_\beta}C_{n_r}+4\mu_b C_{n_\beta}}{\mu_b^2 K_Z^2}} \tag{2.20}$$

Phugoid

The phugoid mode is a slow oscillation in height and velocity. Since the mode is so slow, and variations in α are very small, the pitch rate and α are set to zero. Hence, $\dot{q} = \alpha = 0$. The reduced state-space system is presented in Equation (2.21).

$$\begin{bmatrix} C_{X_u}-2\mu_c D_c & C_{Z_0} & 0 \\ C_{Z_u} & 0 & 2\mu_c \\ 0 & -D_c & 1 \end{bmatrix} \begin{bmatrix} \hat{u} \\ \theta \\ \frac{q\bar{c}}{V} \end{bmatrix} = \vec{0} \tag{2.21}$$

The eigenvalues than become as in Equations (2.22) and (2.23). In these equations C_{Z_0} will not be affected by the TMPs, as the aircraft should still provide the same amount of lift. Therefore, C_{X_u} and C_{Z_u} are the driving parameters for this motion.

$$\zeta = \frac{-C_{X_u}}{2\sqrt{C_{Z_u} C_{Z_0}}} \tag{2.22}$$

$$\omega_n = \frac{V}{\bar{c}} \sqrt{\frac{C_{Z_u} C_{Z_0}}{4\mu_c^2}} \tag{2.23}$$

Short period

The short period mode is a heavily damped mode with a high frequency, where α and q vary. Since the motion is so quick, the airspeed and the flight path angle can be assumed constant. Hence, V = constant and γ = constant. This leaves the state-space system as in Equation (2.24).

$$\begin{bmatrix} C_{Z_\alpha} + \left(C_{Z_{\dot{\alpha}}} - 2\mu_c\right) D_c & C_{Z_q} + 2\mu_c \\ C_{m_\alpha} + C_{m_{\dot{\alpha}}} D_c & C_{m_q} - 2\mu_c K_Y^2 D_c \end{bmatrix} \begin{bmatrix} \alpha \\ \frac{q\bar{c}}{V} \end{bmatrix} = \vec{0} \tag{2.24}$$

Eigenvalues are then obtained from Equations (2.25) and (2.26). According to the formulae, $C_{m_{\dot{\alpha}}}, C_{m_q}, C_{m_\alpha}$ are the key parameters for this motion.

$$\zeta = -\frac{C_{m_{\dot{\alpha}}} + C_{m_q}}{2\sqrt{-2\mu_c K_Y^2 C_{m_\alpha}}} \tag{2.25}$$

$$\omega_n = \frac{V}{b} \sqrt{-\frac{C_{m_\alpha}}{2\mu_c K_Y^2}} \tag{2.26}$$

2.4.4. Controllability

Dynamic stability of an aircraft can be determined using the equations in the previous section. This is then the response of the aircraft to for example a gust. In some sense, one could also argue that the deflection of control surfaces is a disturbance. A very stable aircraft would therefore not respond very well to its control surfaces, unless the resultant force or moment would be very large due to a large control surface. An unstable aircraft on the other hand would respond very quickly to control inputs. Therefore, design choices have to be made whether the aircraft should be very stable and suitable for e.g. beginner flights, or very controllable and designed for e.g. air combat.

If one would add an extra control device, the output of the device should be formatted as a resultant force and a resultant moment. These should then be added to $\vec{F}$ and $\vec{M}$ respectively in Equation (2.15).

3
Numerical Model Setup

In this chapter the setup of the tip-mounted propeller forces model will be discussed. In the end, the forces of the propeller have to be integrated into a non-linear flight mechanics model. Therefore, first the wing evaluation program will be described, which gives a velocity distribution around the wing. This distribution is then used as a velocity field input to the propeller disk, and the propeller forces evaluation will be discussed next. Finally, the implementation of the propeller forces into the flight mechanics model is explained.

3.1. Wing-induced Flow Field

In order to estimate the inflow field for the propeller, a lifting line solver is written. This section includes a brief description of the program and its implementation details, the verification process and its validation, where the resulting lifting line velocity field is compared with a CFD velocity field.

3.1.1. Lifting Line Solver Implementation

The theory of the lifting line as presented in Section 2.1 is implemented in a Python program. Lifting line equations are solved using the numerical lifting line implementation scheme presented by Anderson [27, Sec. 5.4]. This scheme is graphically represented in Figure 3.1. At first a Γ distribution is assumed, from which V_{ind} is calculated. Combined with V_∞, this leads to an effective angle of attack on the wing section α_e. XFOIL then returns a lift coefficient c_l. Using the local velocity at that airfoil, a new Γ is obtained. If the maximum absolute error of the old and new Γ distributions is larger than some predefined limit, Equation (3.1) is applied to acquire a new Γ distribution, and the cycle is repeated. If, on the other hand, the error is smaller than that predefined limit, the Γ distribution is returned and the program is terminated. D in Equation (3.1) is a damping factor. Anderson [27] suggests a value of 0.05. This works well, yet sometimes unnecessarily low and therefore can result in slower convergence. Therefore, it is implemented as a dynamic varying factor for faster convergence. The maximum error for convergence is set to 1e−3 for the rest of this thesis, unless specifically mentioned otherwise.

$$\Gamma_{input} = \Gamma_{old} + D\left(\Gamma_{new} - \Gamma_{old}\right) \tag{3.1}$$

Using the solution of the program described above, the induced velocity due to the lifting lines can be calculated at any point in space. A collection of points on the propeller disk can then be evaluated, and used as input for the propeller forces evaluation program XROTOR, which will be properly introduced in Section 3.2 .

3.1.2. Induced Velocity Verification

In order to verify the code, Python tests have been written. The most relevant tests for our purposes are described in this section. This includes the induced velocity due to a single horseshoe vortex, a swept back lifting line and a dihedral lifting line. To be clear, the theory as presented in Section 2.1 is implemented. This theory is valid for swept and dihedral wings [29].

All cases are wings, represented by a lifting line as discussed in the previous section. Simple unit test cases are drawn up and tested in the program. In all of the upcoming cases, the wing consists of two lifting lines.

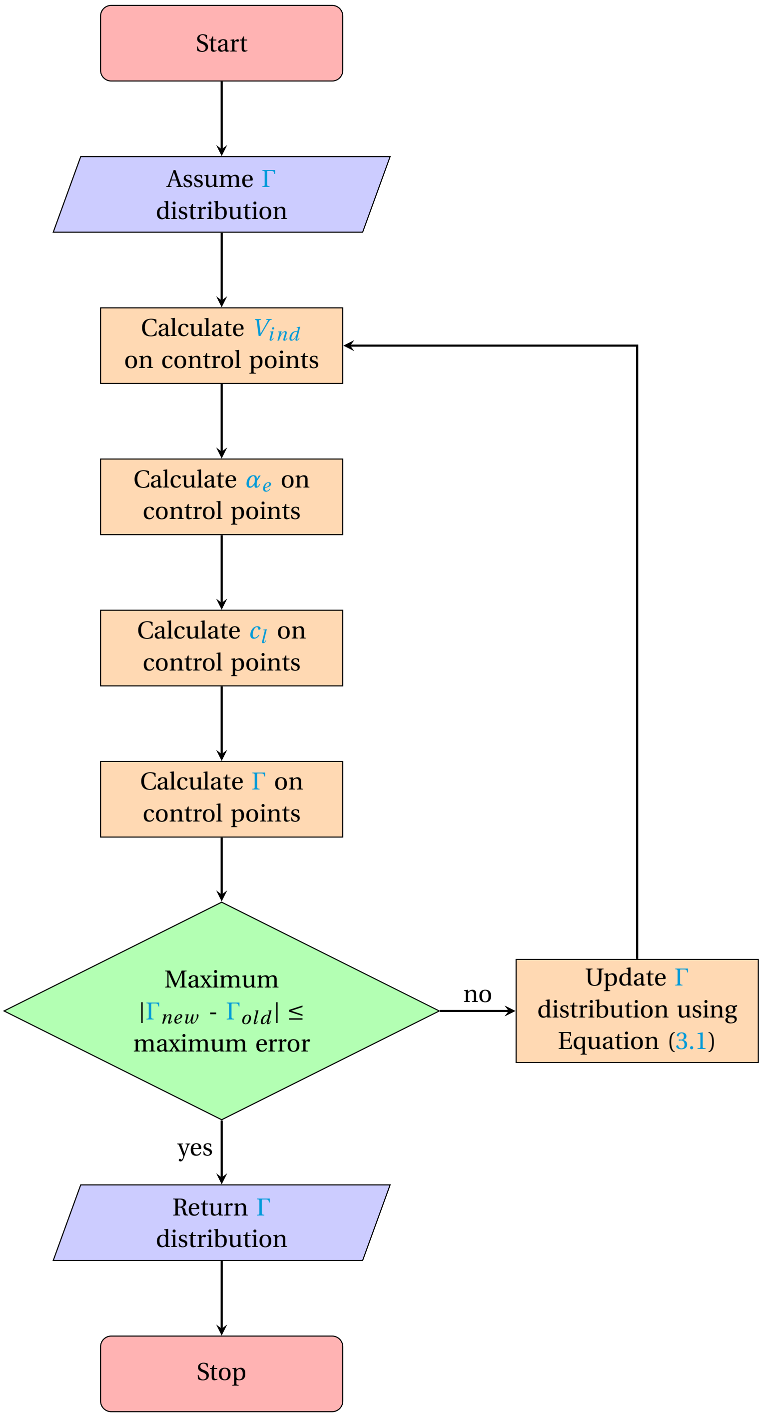

Figure 3.1: Lifting line method solver flowchart

For example, in Figure 3.3 a verification case is depicted. One lifting line, consisting of one section, is defined from the left tip (most negative y point) to the origin. The other lifting line is defined from the origin to the right tip. For each of the lifting lines, the amount of sections per lifting line $N = 1$. Hence, the lifting line is not split up in multiple sections. Equation (3.2) is used to draw up unit test values.

$$\Gamma = \frac{V_\infty \cdot c \cdot c_l}{2} \tag{3.2}$$

The values to fill this equation are given in Table 3.1. Now an airfoil is needed with $c_l = 1$ at $\alpha = 0°$. In that way, the trailing vortices that stretch into infinity are aligned with the x axis, to simplify calculations. The value h is a span parameter, and will be indicated in a figure corresponding to a verification case.

Table 3.1: Unit test values

Variable	Value
V_∞	1
c	1
c_l	1
h	1
Γ	$\frac{1}{2}$

The most basic case is a single horseshoe vortex with strength Γ and semi-span h, as drawn in Figure 3.2. The induced velocity by the lifting line is evaluated at point A. The total velocity at point A is $V_\infty + V_{ind}$. This is calculated analytically by hand and numerically by the program. A similar comparison is made for a sweep case depicted in Figure 3.3, and a dihedral case displayed in Figure 3.4. The results of the comparison are stated in Table 3.2. The analytical results are expressed as exact numbers if space permitted; Otherwise rounded to six decimals. As one can see in the rightmost column, the difference, obtained as analytical number divided by the numerical number times 100, is zero and therefore the lifting lines themselves are considered to be verified.

Table 3.2: Lifting line verification velocity values at point A

Case	Axis	Analytical	Numerical	Difference [%]
Basic	x	1	1.0	0
	y	0	0.0	-
	z	$-\frac{1}{4\pi}$	-0.079577	0
Sweep	x	1	1.0	0
	y	0	0.0	-
	z	-0.129789	-0.129789	0
Dihedral	x	1.071176	1.071176	0
	y	-0.045016	-0.045016	0
	z	-0.090032	-0.090032	0

The solver is verified by entering a value for the lift coefficient at zero angle of attack c_{l_0} and the lift curve slope c_{l_α}. The margin to solve is set to $1\mathrm{e}{-7}$, whereas Anderson [27] indicates that 0.01 is enough. This is done to increase verification accuracy. c_{l0} is chosen in such a fashion, that the downwash produced by a lifting line of strength $\Gamma = 0.5$ will result in $c_l = 1$. For example, in the basic case the local angle of attack due to the downwash is $\tan^{-1}\left(\frac{-0.079577}{1}\right) = -4.55°$. The lift curve slope C_{l_α} is an arbitrary value of $0.11\,\mathrm{deg}^{-1}$. Therefore, $c_{l_0} = 1 + 4.55 \cdot 0.11 = 1.5005$. The results are presented in Table 3.3. One can see in the rightmost column that the difference is marginal, and therefore the solver is considered verified.

Convergence of number of sections

In the past few cases only one section was used per lifting line. In reality, to obtain a satisfactory lift distribution from the lifting line method, a line has to be split into numerous sections. Let us determine how many sections are needed for a whole wing. The result will be used throughout the thesis.

Table 3.3: Solver verification velocity values at point A

Case	c_{l0}	C_{l_α} [deg^{-1}]	Axis	Analytical	Numerical	Difference [%]
Basic	1.500500	0.11	x	1	1.0	0
			y	0	0.0	-
			z	$-\frac{1}{4\pi}$	-0.079577	9.830e-4
Sweep	1.813453	0.11	x	1	1.0	0
			y	0	0.0	-
			z	-0.129789	-0.129789	6.619e-5
Dihedral	1.560375	0.11	x	1.071176	1.071176	-3.978e-7
			y	-0.045016	-0.045016	-5.987e-6
			z	-0.090032	-0.090032	-5.987e-6

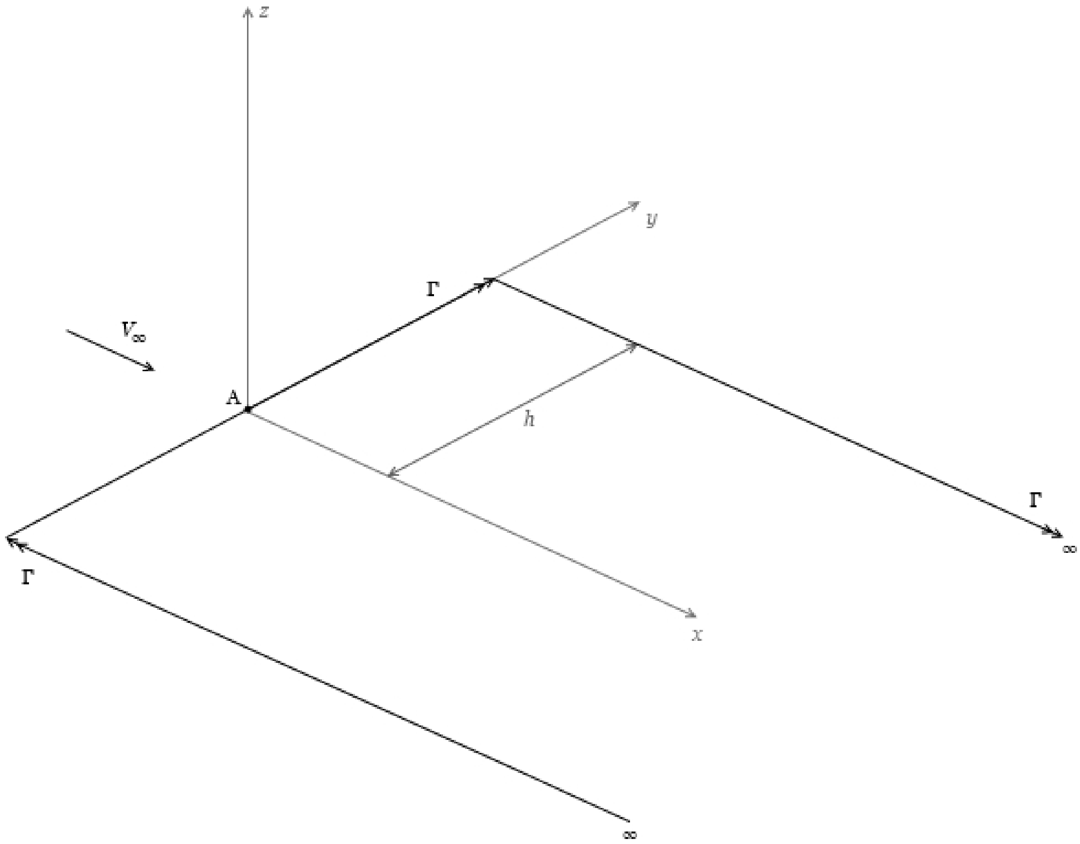

Figure 3.2: Basic horseshoe vortex verification configuration

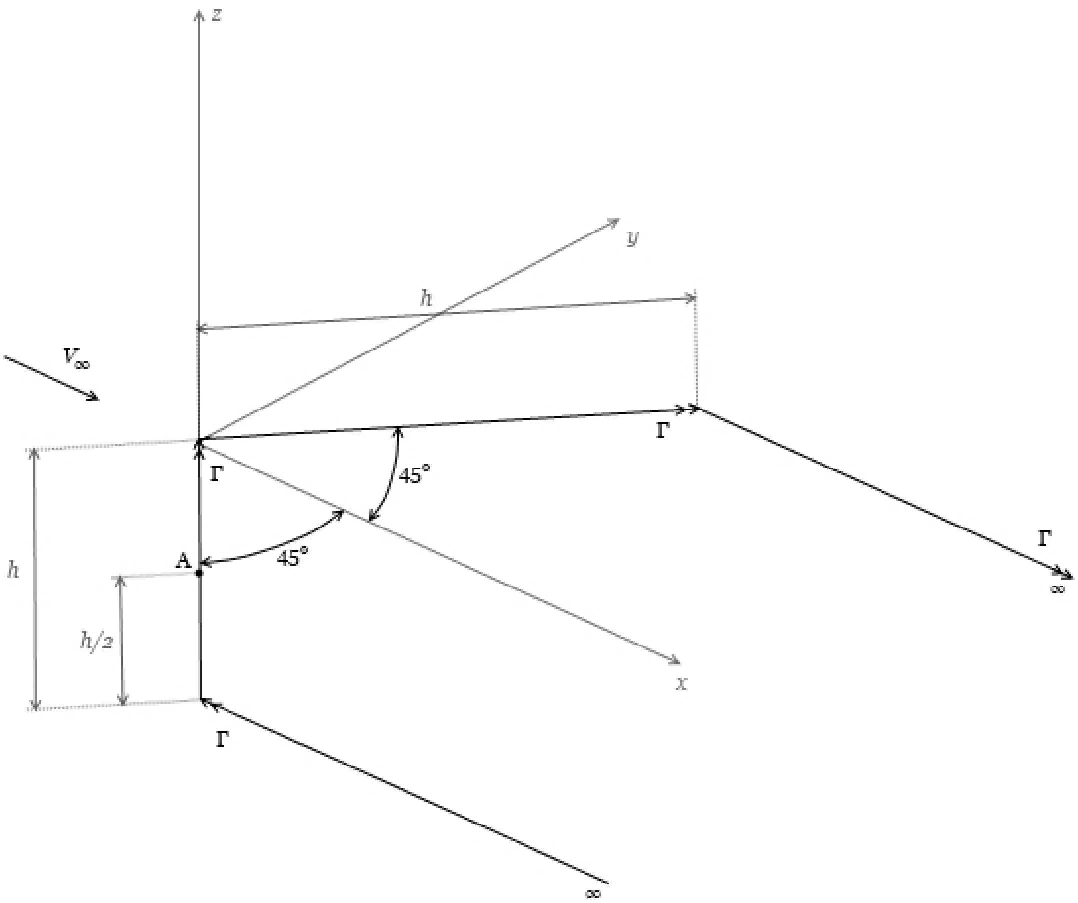

Figure 3.3: Sweep horseshoe vortex verification configuration

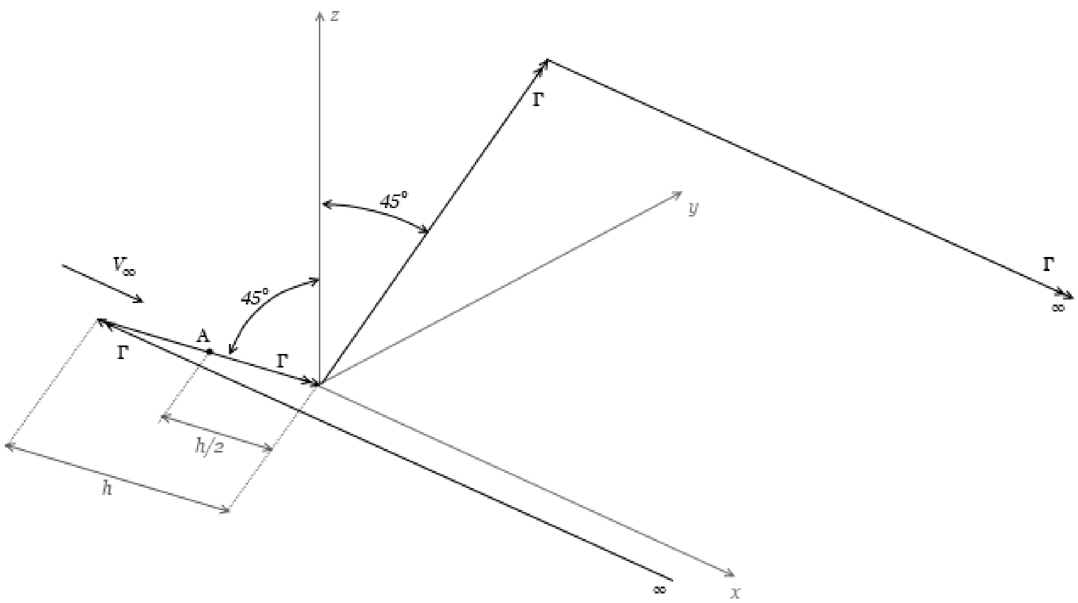

Figure 3.4: Dihedral horseshoe vortex verification configuration

In order to be able to estimate the amount of sections needed for the whole wing, convergence for an elliptic wing is studied. The maximum residual, obtained by comparing the exact Γ solution and the numerical one, after the solver converged (where the convergence criteria was set to 1e−4) is shown in Figure 3.5. Since the computational time increases for larger N, the accuracy increase after N= 60 is not considered to be worthwhile for our applications. Therefore, for a whole wing 60 sections is assumed to be enough for an accurate solution.

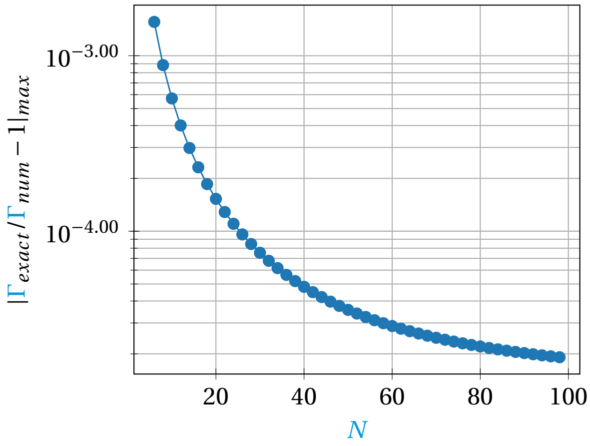

Figure 3.5: Residual convergence for an elliptic wing

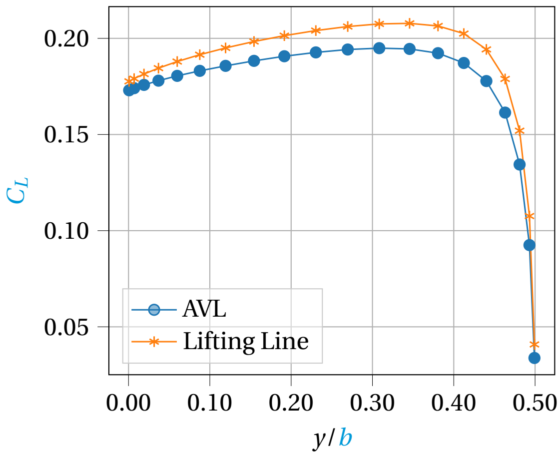

Figure 3.6: Symmetric AVL verification

AVL roll- and yaw-rate verification

The lifting line code has also been compared with a vortex-lattice method solver , AVL [1], to verify a rolling and yawing wing solution. It is verified with AVL since an analytical solution for these cases would be hard to obtain. The evaluated wing has a span of 10 m, a root chord of 1.5 m and a tip chord of 0.5 m. A NACA 2404 airfoil is used at an angle of attack of 0 deg, without any twist, dihedral or sweep. The thin airfoil is used as an attempt to reduce thickness effects to a minimum, which are neglected by AVL. As this will never truly succeed, the lifting line code will overestimate C_L with respect to AVL. A thicker profile will increase the lift slope by attaining higher velocities over the airfoil. The symmetric inflow wing lift distribution is shown in Figure 3.6.

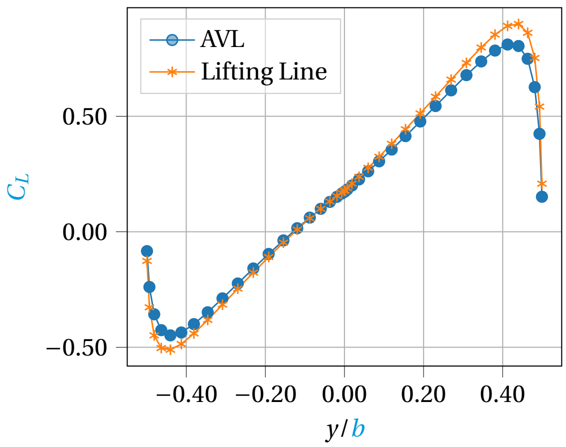

Figure 3.7: Asymmetric p AVL verification

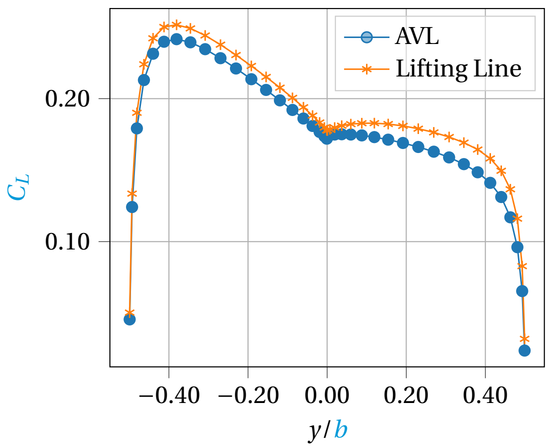

Figure 3.8: Asymmetric r AVL verification

As one can see there is a small discrepancy between the lifting line and AVL. The lifting line structurally over-estimates the lift coefficient, as is expected. Since the lifting line method will be validated in the

[1] http://web.mit.edu/drela/Public/web/avl/ ; Accessed 16-01-2020

upcoming section, no further attention will be directed to this discrepancy since it is not relevant for our case. The goal of this section however, is to compare roll rate and yaw rate behaviour. Resulting lift distributions due to roll and yaw rate are depicted in Figures 3.7 and 3.8 respectively. In both cases, the lifting line code overestimates the lift distribution slightly. This only confirms the trend set in the symmetric case.

For the rolling wing, $p = 20$ [deg$\cdot$s^{-1}]. The right wing is going downward, increasing its angle of attack. This will lead to an increased lift coefficient on the right wing. The left wing will have a negative lift distribution, as confirmed in Figure 3.7. A small discrepancy is visible, yet is comparable with the discrepancy for the symmetric case. Therefore the solution with respect to roll rate is considered verified.

For the yawing wing, $r = 20$ [deg$\cdot$s^{-1}]. The left wing will have extra velocity, increasing its lift coefficient with respect to V_∞. The right wing will have less velocity, and a decreased C_L. This behaviour is confirmed in Figure 3.7. A small discrepancy is visible, yet is comparable with the discrepancy for the symmetric case. Therefore the solution with respect to yaw rate is considered verified as well.

3.1.3. CFD Validation

As the lifting line solution will be used to calculate the inflow field on a tip-mounted propeller, the flow field around the tip of a lifting line wing should be compared to the flow field around the tip of a real wing. Since such measurements on a full scale wing are very hard to attain, the lifting line solution is compared with a CFD case. This will lead to discrepancies, as CFD is a viscous simulation, whereas the lifting line is a potential method, where only sectional viscous effects are incorporated. This CFD solution has been used in Ref. [47], for the analysis and design of a wing-tip mounted pusher propeller. The that is analysed is the wing of the Tecnam P2012 Traveller. A top view, where three lifting lines are indicated, is presented in Figure 3.9. This top view is an altered image from Tecnam[2].

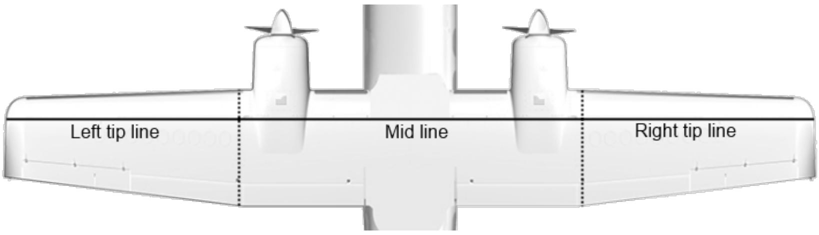

Figure 3.9: Validation wing top view including three lifting lines

To be able to validate the lifting line model of the Tecnam wing, the convergence of the model needs to be determined. Any discontinuities in a wing alter the smoothness of the lift distribution. Therefore, the node grid needs to be denser near discontinuities. The wing is split up into three lines, called the left tip line, mid line and the right tip line. Each line then ends at a discontinuity. It is split into sections using cosine spacing, increasing grid density at the line ends.

The flow field around the wing is largely dependent on the lift distribution. C_L convergence is first checked in Figure 3.10. N is the number of sections per lifting line. Since the wing consists of three lifting lines in this case, $N = 20$ means a total of 60 sections over the whole wing. As concluded before, in the convergence study for the number of sections, 60 sections indicates a converged lift distribution.

Lift distributions resulting from CFD analysis and the lifting line model is presented in Figure 3.11. The lifting line model overestimates the C_L somewhat, however it is close and the shapes are the same. This indicates that the vorticity created by the wing in both models is comparable, which builds confidence in the reliability of calculated induced velocities.

Flow Field Comparison

Now that the convergence of the lifting line method for the validation wing is established, the velocity fields resulting from CFD and the lifting line can be compared. Since the tip area of the wing is relevant to this research, the centre point of the analysis is defined as $0.07x/c$ behind the trailing edge of the left tip. By comparing the induced velocity at different locations behind the wing, the error between the induced velocities for the CFD and the lifting line case was largest just behind the wing. Therefore this point just

[2] `https://p2012.tecnam.org/technical-specs/specifications/`; Accessed 12-01-2020

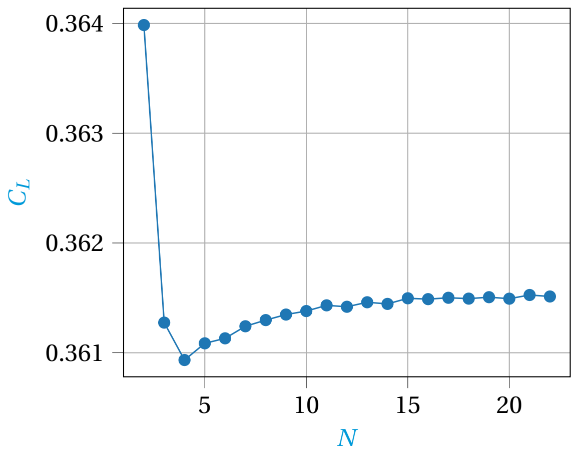

Figure 3.10: C_L convergence

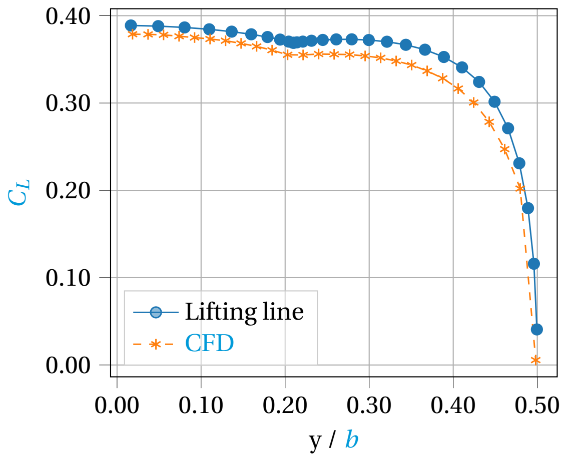

Figure 3.11: Spanwise lift distribution

behind the wing tip has been chosen, to show the worst case here. Around this centre point tangential and axial velocities are depicted in Figures 3.12 - 3.15.

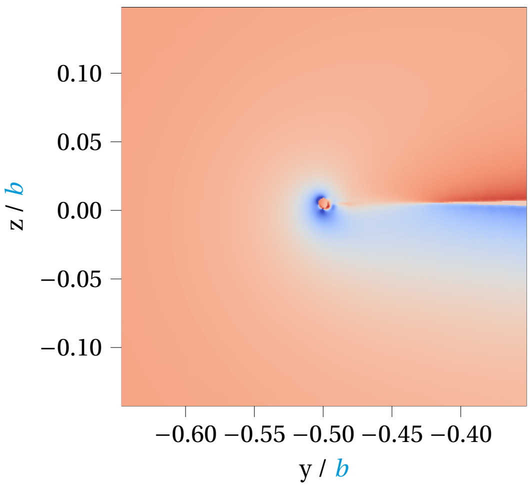

Figure 3.12: CFD induced velocities in t at $x/c = 0.07$

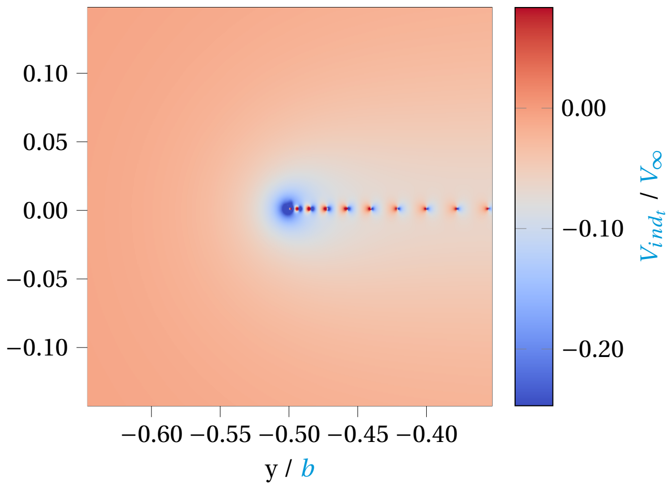

Figure 3.13: Lifting line induced velocities in t at $x/c = 0.07$

Tangential velocities are quite comparable between the two models. The same trends and shapes are shown, where a circumferential shape can be distinguished for the tangential velocity in Figures 3.12 and 3.13. This does not hold for the wake of the wing. In the CFD case, a wake can be seen in the axial velocity plots, whereas this wake is not present in the lifting line case. This is because CFD runs a viscous simulation where a wake forms, and the lifting line method is a potential method, and therefore does not. The 'wake' of the lifting line case however, which are the trailing vortices, can be clearly seen in the tangential case. Discontinuities are clearly visible in Figure 3.13. Let us asses the influence of the singularities resulting from the lifting line code, by comparing the induced velocity of the lifting line code to the CFD case. This is done by choosing a line from the centre point outwards, where the radial coordinate is described by r/b and the angle by ξ, as in Figure 3.16, and evaluate the induced velocity on each point of that line.

For $\xi = 0, \pi/4, -\pi/4$ V_{ind_t} has been evaluated in Figures 3.17 - 3.19. As expected, for $\xi = 0$[rad] the singularities have a large influence on V_{ind_t}. The trend is the same as the CFD line, yet sharp peaks arise. For $\xi = 0.79$ or $\xi = 5.5$, the discontinuities caused by the trailing vortices are absent.

At this point, it is not clear whether the singularities will influence the solution of the propeller force evaluator. Let us therefore investigate what the influence is on the average cylindrical induced velocity distribution. Two approaches can be used, and both will be tested further on. The first is to simply average the induced velocities including the velocities close to the singularities, and the second one is to filter them

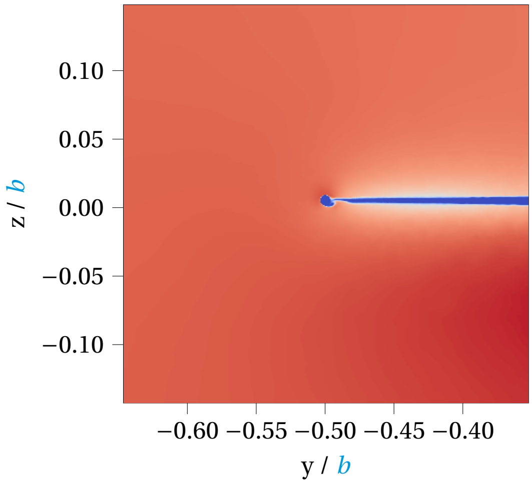

Figure 3.14: CFD induced velocities in z at $x/c = 0.07$

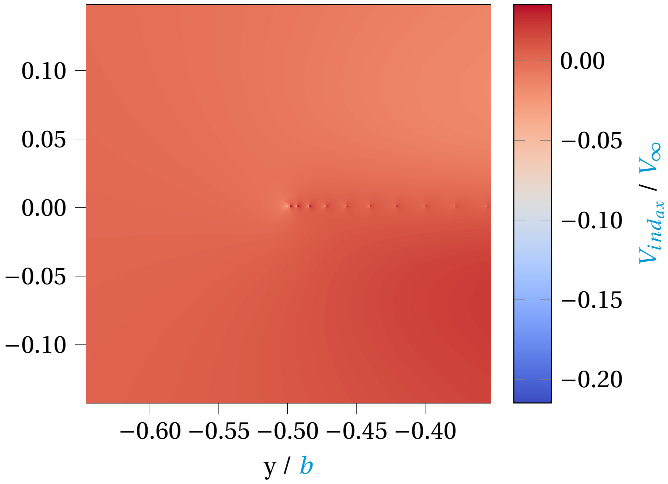

Figure 3.15: Lifting line induced velocities in z at $x/c = 0.07$

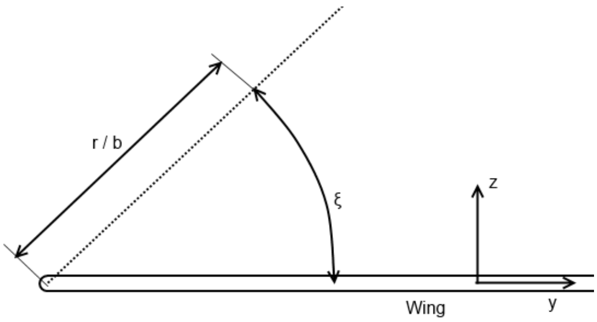

Figure 3.16: Induced velocity plots definitions

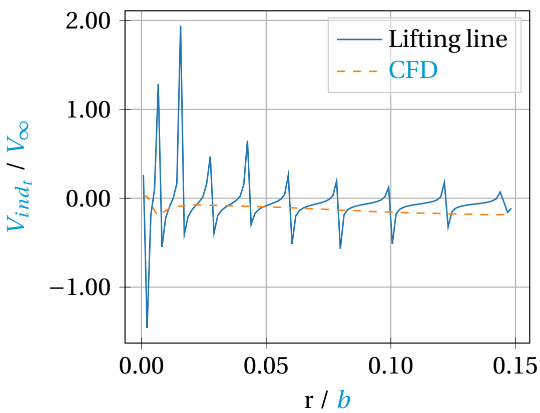

Figure 3.17: Induced velocities in t at $x/c = 0.07$ and ξ=0.0 [rad]

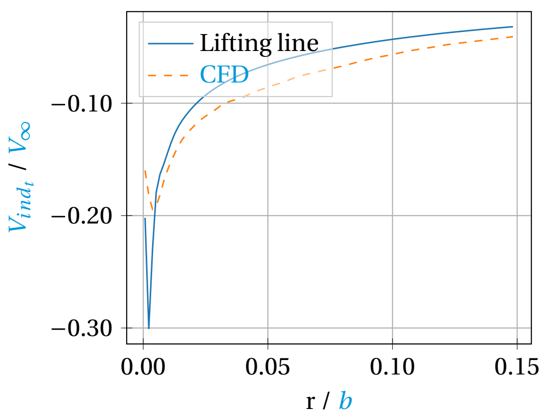

Figure 3.18: Induced velocities in t at $x/c = 0.07$ and $\xi = \pi/4$ [rad]

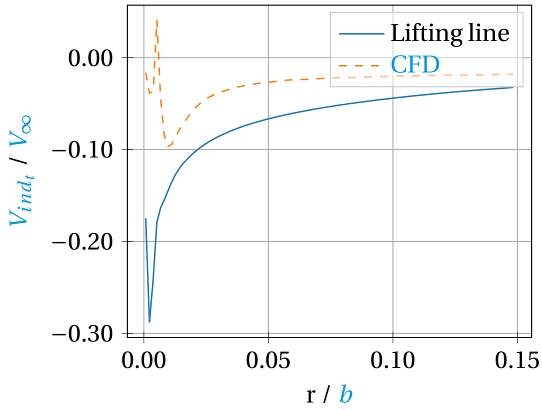

Figure 3.19: Induced velocities in t at $x/c = 0.07$ and $\xi = -\pi/4$ [rad]

out. In the filtered version, since at $\xi = \pi/4$ and $\xi = -\pi/4$ the influence of the singularities is absent, t and z velocity components are cylindrically averaged between $\xi = \pi/4$ and $\xi = -\pi/4$. This filtered version will be denoted by "Lifting line filtered" in the following analysis.

In Figures 3.20 and 3.21, the averaged cylindrical velocities in t and z are displayed. As expected from the contour figures, the trend of the average velocities in t is the same as for the CFD case, except very close to the tip vortex' core. Around r/b= 0.01, the three lines nearly overlap. With increasing r, lifting line and CFD agree more and more, where the filtered lifting line is underestimating V_{ind_t} compared to CFD. Even though discontinuities due to the trailing vortices are clearly visible, the unfiltered lifting line seems to perform better than the filtered version.

With respect to the axial velocity component, these do not match as well since the turbulent wake is not present in the lifting line model. However, the effect of the axial component with respect to the free-stream is very small. The largest is error is also near the vortex core. At larger values of r the induced axial velocity is degrading, and the lifting line and CFD method indicate it to reduce to 0.

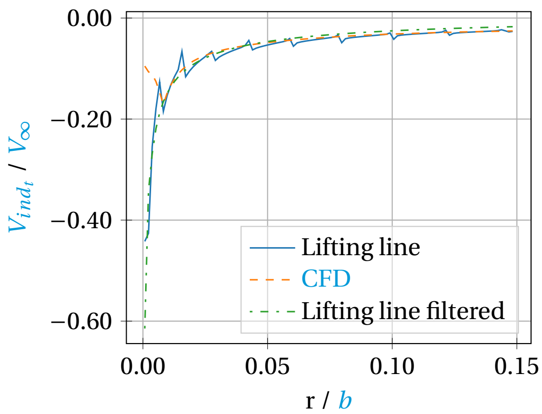

Figure 3.20: Averaged induced velocities in t at $x/c = 0.07$

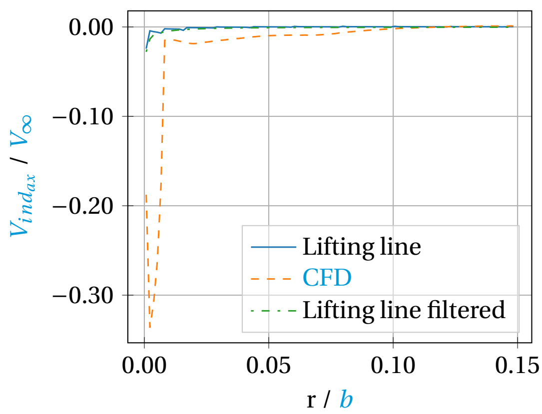

Figure 3.21: Averaged induced velocities in z at $x/c = 0.07$

The effect of the discrepancy between the CFD induced velocity solution and the one obtained by the lifting line solver will be evaluated by comparing the solution of the resulting propeller force and power due to these two inflow fields. The propeller force and power will be evaluated using a program, which is defined in the following section. This program is XROTOR, where a combined blade-element momentum vortex method is used. Even though the program has not yet been properly introduced, it will be used to evaluate the thrust and power coefficient on the propeller to compare the CFD and lifting line inflow fields. In this thesis the decision is made to first close the lifting line subject, before moving on to the propeller. If the reader wishes more information about XROTOR before this comparison, the reader is referred to Section 3.2.

Effect on XROTOR output

The flow fields (filtered and unfiltered) due to the lifting line wing are known. The validation data from CFD is also a flow field, which differs slightly from the lifting line flow field. Since the flow field is used for propeller force and power estimations, these force and power parameters will be used to quantify the impact of differences in the induced flow-fields on the resulting computed propeller forces.

The flow fields have been averaged into single values per radial station, which is the input format for XROTOR. Since the error is largest for a small propeller diameter and close to the wing, the analysis is done at X=1.13 (around 10cm behind the wing trailing edge), with a propeller diameter of 1m and a propeller blade pitch of 30 [deg]. The following flows are analysed:

- CFD
- Lifting line
- Lifting line (filtered)
- Uniform inflow field of V_∞

C_T and C_P values for the previously described propeller and location for the aforementioned flow fields can be found in Tables 3.4 and 3.5 respectively.

Table 3.4: XROTOR C_T values for different inflow fields at X=1.13

	J=1.0	J=1.2	J=1.4	J=1.6	J=1.8
CFD	0.27011	0.17574	0.07925	-0.02463	-0.13931
Lifting line	0.26736	0.17148	0.07321	-0.03299	-0.14959
Lifting line (filtered)	0.26551	0.16964	0.07141	-0.03484	-0.15115
None	0.23951	0.14029	0.03748	-0.07298	-0.19307

Table 3.5: XROTOR C_P values for different inflow fields at X=1.13

	J=1.0	J=1.2	J=1.4	J=1.6	J=1.8
CFD	0.34782	0.24037	0.14318	0.03546	-0.08785
Lifting line	0.34533	0.23647	0.13738	0.02718	-0.09855
Lifting line (filtered)	0.34309	0.23421	0.13501	0.02457	-0.10121
None	0.31246	0.20208	0.09687	-0.02014	-0.15311

For both the positive as the negative C_T regime, the values correspond quite well, where the thrust coefficients from the unfiltered lifting line inflow field correspond best with the CFD inflow field. Furthermore, one can conclude that it is worthwhile to include the inflow field for the propeller analysis as the uniform inflow field is structurally off in C_T and C_P estimation. A normal operating condition for this propeller would be an advance ratio of 1 and a blade pitch of 30 [deg]. At that point the discrepancy between the lifting line method and CFD is very small. Larger errors are introduced when the blade is far off its normal operating point. In that case the blade angle is far into the negative regime, and XROTOR is working with stalled polars. Small fluctuations in V_{ind_t} and $V_{ind_{ax}}$ will be amplified at this point by XROTOR. Even so, the trend is still correct.

The induced velocity fields by the lifting line method and CFD are comparable with a small discrepancy. This small discrepancy leads to a 3e−3 error in C_T for normal operating conditions, and a 1e−2 error for extreme off-design operating conditions. For the scope if this study such errors are considered to be small, as only low-fidelity tools will be used. The accuracy of this method does not prevent us from drawing credible conclusions from trends of parameter sweeps. For a quantitative analysis of the inflow field the lifting line method is therefore considered validated.

3.2. Propeller Forces with Blade-element Analysis

From the lifting line model in the previous section a velocity field is obtained. This has to be used as input for XROTOR [3], which will evaluate the thrust and power of the propeller. The resulting force and power can then be applied to a flight mechanics model.

In this section first a tool will be selected with which the forces and the power on the propeller can be evaluated. All the inputs will then be defined, along with the fashion in which outputs are handled and saved.

[3] http://web.mit.edu/drela/Public/web/xrotor/ ; Accessed 16-01-2020

3.2.1. Evaluation Tool Selection

Section 2.2 presented multiple methods to evaluate the forces on a propeller. These methods have been implemented in computer programs, that allow for quick evaluation of propeller forces. As both thrust and drag (reverse thrust) are important parameters for this thesis, a method should be selected that calculates thrust and drag in an accurate manner. Tools that incorporate these methods from Section 2.2 are JavaProp, XROTOR and an in-house tool. JavaProp uses a simple blade element momentum method. XROTOR incorporates multiple options; A graded momentum formulation that is suitable for low advance ratios and/or many blades, and a potential formulation that is more computationally expensive. This incorporates an extension of Goldstein's two and four blade solution for the helically-symmetric potential flow about a rigid helicoidal wake. Furthermore, a BEM program is available as presented by Veldhuis [6] in his doctorate thesis, which (in contrast to JavaProp and XROTOR) can handle yawed inflow angles. This tool however is not as widely used as XROTOR.

A comparison between blade-element models of propellers has been done by Gur and Rosen [35]. This is an in-depth validation of methods described by Theodorsen, McCormick, a simplified momentum, and a lifting line method. The article recommends to use the simplified-momentum model, as it is computationally efficient with reasonably high quality results. One should turn to the lifting line free wake method for highly loaded propellers or in static operation as the wake is then more important. As stated previously, XROTOR incorporates both methods.

XROTOR has been used extensively at the TU Delft. Examples of this tool being used in-house can be found in Ref. [48, p. 31] and Ref. [49, p. 8]. Here, XROTOR is validated with respect to test measurements of the N250 propeller, and shows deviations of C_T and C_P of 10% at most. JavaProp has been tested as well, and shows worse performance than XROTOR. XROTOR evaluates a propeller in a matter of seconds, which enables large design space explorations and allows accurate tabulation of aerodynamic forces and derivatives. Therefore, XROTOR is chosen as the propeller evaluation tool.

Theoretically, the methods presented in Section 2.2 are valid for both propulsive as drag-generating/recuperating propellers. The differences are that for recuperating propellers the local blade angle of attack generally is negative, and that the slipstream is expanding instead of contracting. Therefore, theoretically, the tools mentioned above should be valid in the recuperative regime. XROTOR has been compared with CFD in a recuperating regime. In Figure 3.22 one can see that discrepancies for C_T are small (i.e. within 10%), however deviations for C_P are larger. For this research the extracted power from the flow is not relevant. For further validation data the reader is referred to Ref. [50], where the propeller used is described in Ref. [51].

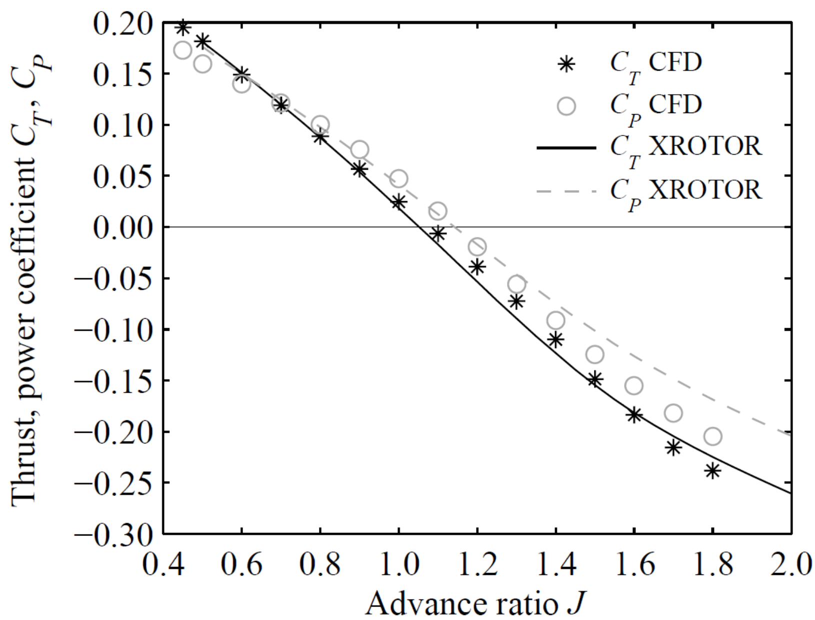

Figure 3.22: Wind-milling propeller performance CFD - XROTOR comparison [42]

3.2.2. Isolated Propeller Performance

Since the research is a feasibility study, and general forces are important, the propeller should be applicable to the situation chosen. It does not necessarily have to be the propeller of the base-line aircraft, as the aircraft is modified and not redesigned. It is important that the propeller geometry is known, and that its performance can be validated. Therefore, the N250 propeller geometry is chosen as it is available in-house and used for multiple studies (e.g. Ref. [52] and the references mentioned above). It is depicted in Figure 3.23, where the mentioned dimensions are in millimetres. For our purposes the propeller is scaled along all axes to some diameter.

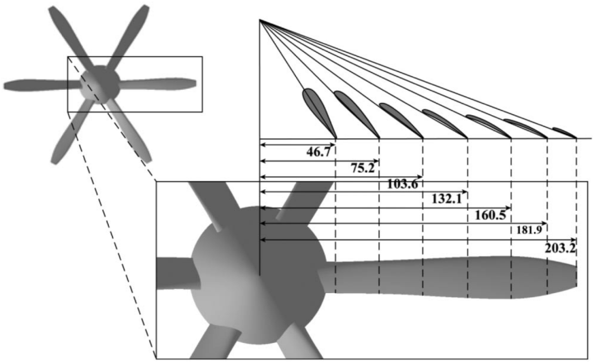

Figure 3.23: N250 propeller layout from Ref. [52]

The propeller will be evaluated over a large range of β_p and J. To be able to judge whether calculated thrust is feasible, the isolated propeller should first be evaluated. This will also give an indication of the intended operation range of the propeller.

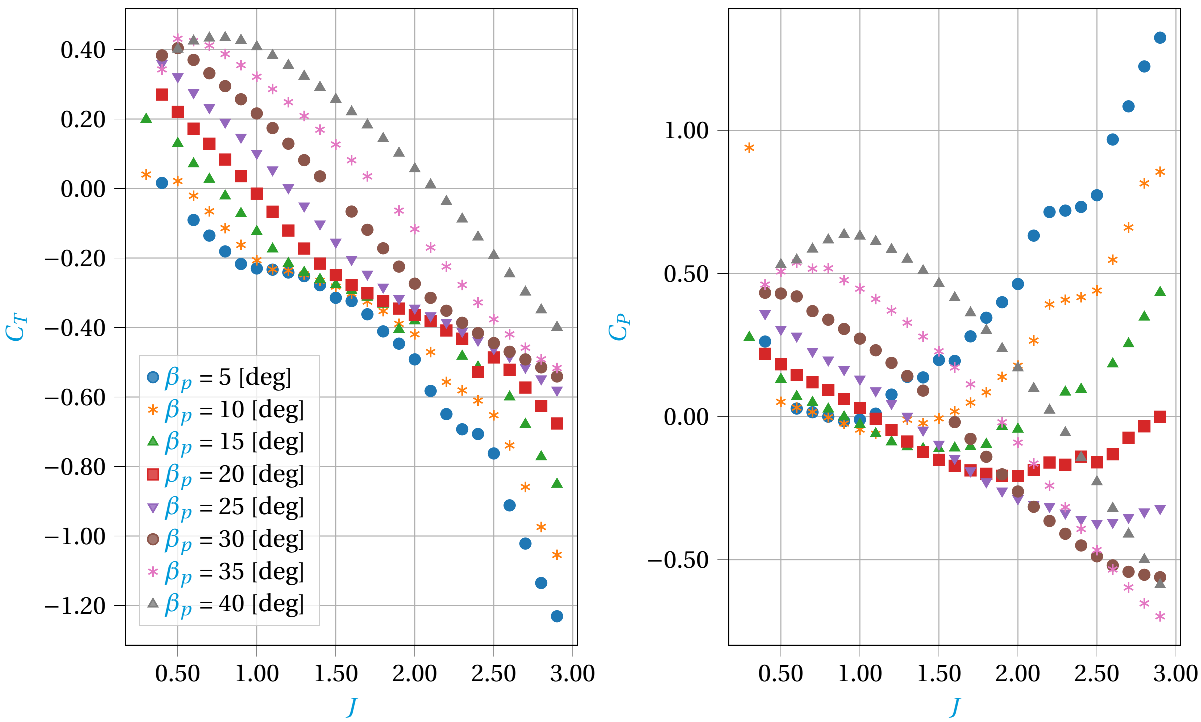

Figure 3.24: Isolated N250 performance parameters

In Figure 3.24 the performance (C_T and C_P) of the N250 propeller is depicted. Used parameters are D= 1[m], and V_∞= 40[m/s]. It becomes clear that XROTOR is capable of solving a wide range of β_p and J. In the right graph, C_P is plotted. The slope is quite linear at some points, yet it begins or ends with a curve. When

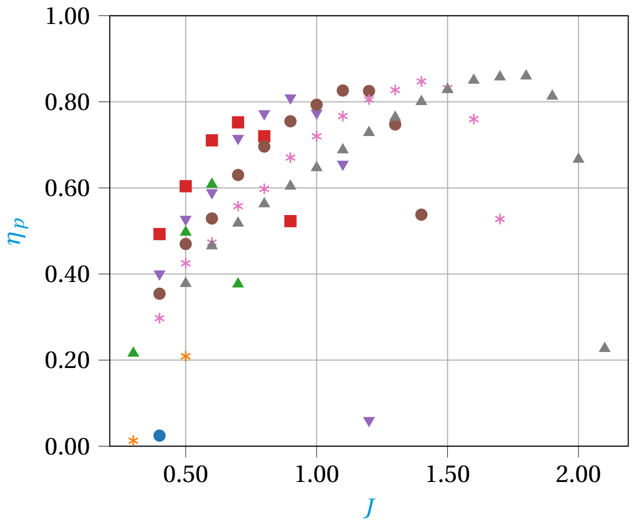

Figure 3.25: Isolated N250 efficiency

the line starts to curve, the blade is starting to stall. First of all, the stalled range is inefficient and should therefore not be used. However, within the stalled regime the BEM method's accuracy becomes questionable as 3D effects become more prominent. Therefore, bounds are introduced on β_p and J to remain confident in the results for the propeller's performance. These are tabulated in Table 3.6, and selected by the suspected reliability of convergence, based on the variability of neighbouring solutions. The values are obtained by inspection from Figure 3.24.

Table 3.6: N250 propeller operating boundaries

β_p [deg]	$J_{min}[-]$	$J_{max}[-]$
5.0	0.5	1.5
10.0	0.5	1.8
15.0	0.5	1.8
20.0	0.5	2.3
25.0	0.5	-
30.0	0.5	-
35.0	0.5	-
40.0	0.5	-

$$\eta_p = J \cdot \frac{C_T}{C_P} \tag{3.3}$$

Propeller efficiency η_p is plotted in Figure 3.25 using Equation (3.3). The legend of Figure 3.24 is applicable to this figure as well. Lower blade pitches are more efficient at low advance ratio's, and higher blade pitches at higher advance ratio's. This graph can be used during this thesis to check whether an operating point of the propeller is a nominal operating point or not. According to this graph, anywhere between J= 0.7 and J= 1.8 nominal operating points can be obtained by varying β_p.

3.2.3. Propeller Force Parameter Definition

The wing's lift distribution alters the inflow field of the propeller. An inviscid vortex method is used to calculate the flow field around the wing, to alter the inflow of the propeller. The output of this flow field should be compatible with the input format of XROTOR. This format is described in Table 3.7, where radial profiles of axial and tangential induced velocity without circumferential variations are indicated. Therefore the wing flow field needs to be converted into this format, by one of the following two options.

1. Sum all trailing vortices to two wing tip trailing vortices and use the velocity field resulting from these vortices

2. Calculate the velocity field from the trailing vortices as in Section 2.1, and average the input to a single radial distribution

Since the lifting line method is the chosen method to evaluate the wing, where its trailing vortex sheet can be readily evaluated for the second method, this method is chosen. The images of Section 3.1.3 show that circumferentially averaging the tangential and axial velocities is a good option.

Table 3.7: XROTOR slipstream input format [4]

R(1)	$V_{axial}(1)$	$V_{tang}(1)$
$\vdots$	$\vdots$	$\vdots$
R(N)	$V_{axial}(N)$	$V_{tang}(N)$

Propeller forces need to be obtained for the dataset to be filled. This needs to be done with respect to the input of the wing flow field, which is a function of α, p and V_∞, and all propeller geometry and thrust setting inputs. Except for blade pitch angle β_p and diameter D, these inputs can be formatted to a short form, as the speed vectors, rotations around the rotational axis, and RPM input can be compiled into a propeller angle of attack α_p and advance ratio J. Effects of rotations normal to the rotational axis are assumed to be small in comparison with the incoming flow velocity. The propeller inputs are summarised in Equation (3.4). The outputs are thrust T, power P and normal force Y. The normal force does not necessarily have to be in the y direction as the normal force can always be expressed as a single force magnitude. Pitching and yawing moments produced up to an angle of attack of 30° are considered negligibly small [53].

$$T, Y, P \rightarrow f\left(\alpha(t), p(t), V_\infty(t), \beta_p(t), \alpha_p(t), J(t), D\right) \tag{3.4}$$

A limitation of XROTOR is that it can not be used for yawed inflow angles. An engineering method is presented by De Young [38] based on the work of Ribner [39]. This empirical method is compared with experimental values for the normal force coefficient [6] as in Figure 3.26. The experimental values are obtained from the references indicated in this figure, where R1 denotes the propeller used in the reference indicated by R1. One can see that for R1 and R3 results are accurate; Unfortunately the document of R2 could not be retraced. Table 3.8 gives the parameter range in which this method is acceptable (typical errors within 15%). The values in this table appear to be determined experimentally. It should be noted that negative values for the thrust coefficient are outside of the parameter range. The formulas presented are obtained from Ref. [39], where no limitations are imposed on the empirical formulae. It is therefore assumed that negative values are simply not tested. For validation data for this method the reader is referred to Refs. [38, 39, 53–57].

Table 3.8: Yawed propeller inflow estimation method parameter range [6, p. 46]

Parameter	Range
Number of blades, B	$2 \leq 10$
Effective solidity, σ_{eff}/B	$0 \leq \sigma_{eff}/B \leq 0.08$
Propeller effective AoA, α_p	$\alpha_p \leq 20$[deg]
Mach number, M	$M \leq 0.4$
Thrust coefficient, C_T	$C_T > 0$
Blade pitch angle, β_p	$\beta_p \geq 5$[deg]
Loading	Low to moderate

XROTOR is called from a Matlab wrapper. By varying all input parameters over some range using a Python object, a 7D table is filled containing T, P and Y. The axes of this table are the variables on the right hand side of Equation (3.4). The table will only be evaluated for the right wing tip, since the left hand side can then be simply mirrored to extract the corresponding forces.

Output Dataset Post-processing

When the dataset is evaluated, XROTOR sometimes fails to solve the propeller situation. These are values that should be readily solvable by XROTOR, however apparently are not. Such values are interpolated, since

[4] http://web.mit.edu/drela/Public/web/xrotor/xrotor_doc.txt ; Accessed 04-10-2018

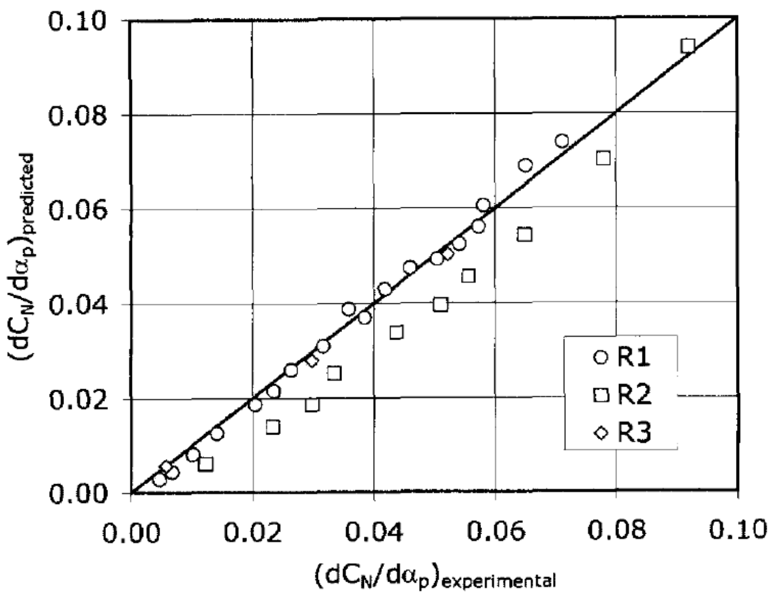

Figure 3.26: Normal force coefficient variation with angle of attack. R1=Ref.[54], R3=Ref.[55]. Obtained from [6, p. 47]

the trends in the propeller forces will appear to be very predictable in Chapter 4. This interpolation is done in a cubic fashion in a plane of J and β_p, using SciPy's interpolation software [5]. Before this interpolation is performed, first data points outside of the propeller boundaries determined in Table 3.6 are deleted. For blade pitches that are not incorporated in the table, the corresponding advance ratios have been linearly interpolated. Then, only holes that have larger and smaller solved values in J and/or β_p are interpolated. An example is given in Appendix A. The corrected dataset as defined here is used in the remainder of this report.

3.3. Implementing Propeller Forces into a Non-linear Flight Mechanics Model

Propeller forces should be implemented in the flight mechanics model. This is done by generating a dataset in the fashion described by the previous section. The inputs of this database, as stated in the aforementioned section and defined in Equation (3.4), should be linked to the states that are available within the aircraft's flight mechanics model. This is a modelling step. Therefore, first we will discuss what effect the aircraft state has on the force of the propeller. We then arrive naturally at the assumptions, which then is followed by how the remaining effects are implemented in what fashion. The section will be concluded by the transformation of the propeller forces to the aircraft's body frame.

Influence of the Aircraft State on the Propeller Forces

In the used flight mechanics model, there are 12 aircraft states. The ones relevant for this section are listed below.

- u : Aircraft X-velocity in the body frame
- v : Aircraft Y-velocity in the body frame
- w : Aircraft Z-velocity in the body frame
- p : Aircraft angular velocity along X-axis in the body frame
- q : Aircraft angular velocity along Y-axis in the body frame
- r : Aircraft angular velocity along Z-axis in the body frame

The remaining six state variables, which are the aircraft's orientation in space, are not directly relevant for the forces on the propeller.

[5] https://docs.scipy.org/doc/scipy/reference/generated/scipy.interpolate.griddata.html ; Accessed 12-12-2019

Angles are easier to visualise than decomposed velocities. Therefore V_∞, α and β_s offer a more natural perspective of discussion, and these will be used in this section as state variables instead of u, v and w. For each of the relevant state variables, the effect on what the propeller experiences is stated in Table 3.9.

Table 3.9: State variable implications on propeller forces

State	Effect
V_∞	The free-stream airspeed directly influences the mass flow through the propeller disk. Furthermore, if the propeller RPM is kept constant, the advance ratio is affected. Finally, the free-stream airspeed directly influences the induced velocities around the wing.
α	Alters the wing lift distribution, and hence the induced velocities. Furthermore, the angle of attack on the propeller is influenced.
β_s	Alters the wing lift distribution by introducing extra downwash on the lee semi-wing, and hence the induced velocities. Furthermore, the angle of attack on the propeller is influenced.
p	Alters the wing lift distribution and hence the induced velocities by increasing the local angle of attack on the down-going wing, and decreasing the local angle of attack on the up-going wing. Furthermore, the angle of attack on the propeller is influenced. Finally, influences the thrust on the propeller due to rotational motion.
q	Influences the thrust on the propeller due to rotational motion.
r	Alters the wing lift distribution, and hence the induced velocities by adding velocity to the forward-going wing and decreasing velocity on the aft-going wing. Also influences the velocity felt by the propeller, and therefore its advance ratio and thrust.

Propeller Model Assumptions

The state of the model has to be linked to forces on the propeller by the input variables as described in Section 3.2. Some assumptions have to be made with respect to the interaction of the wing and propeller, where the largest effects are incorporated into the model. Other assumptions are included to keep the size of the dataset manageable, where also the largest effects are taken into account. All assumptions will be checked for their validity in Section 4.2. These assumptions are listed below, followed by a brief discussion on the expected effect of these assumptions:

- **The propeller has no influence on the flow field around the wing.** This means that the upstream effect of the pusher propeller is neglected, resulting in an incorrect circulation over the wing. The error is expected to be small, since most velocity effects are right in front of the propeller [45]. In Ref. [45] section measurements are done with a pusher propeller with a high thrust setting to simulate take-off conditions, where the increment in c_l was between 0.1 and 0.2.
- **The angle of attack of the propeller with respect to the free-stream is equal to the wing angle of attack.** As the tip vortex of a wing folds up, it generally travels in the direction of the free-stream [29]. Therefore, the effect of this assumption is deemed small
- **The yaw angle of the whole aircraft is the same as the local yaw angle at the propeller.** According to lifting line theory as described in Section 2.1, whether a wing is in yaw or not does not change the airflow. The flow will not be axially accelerated by the trailing vortices of the lifting line, yet the flow will be accelerated in spanwise directions (outboard acceleration on the lower side of the wing, and vice versa on the top side of the wing). Therefore the average local angle of sideslip over the propeller disk will be equal to β_s.
- **The propeller inflow field is not influenced by yaw-rate.** As the tip speed variation due to yaw-rates with respect to the free-stream is small, the influence on the lift distribution is small as well. However, the advance ratio J that the propeller feels is different, resulting in a different thrust. Therefore, the variation of J due to r will be implemented in the model, yet the induced velocity inflow field for the propeller will not be implemented. By converting yaw-rate to a new J, the resulting thrust alterations due to r are believed to be captured.

These assumptions will be reflected upon in Section 4.2.

Obtaining Propeller Input from State Variables

As the effect of the states on the propeller inflow field is now known, one can move to deciding how to incorporate each of these effects, or whether an effect is too small and therefore can be neglected. The propeller input needs to be calculated from the aircraft's state. This step is the modelling step, and hence a crucial one. Therefore the implementation of obtaining the propeller inputs from the aircraft's state are described in Table 3.10 for a clear overview on this modelling step. The variable 'wing induced velocities' denotes the inflow field which is used by XROTOR to calculate the propeller forces, and which is a result of the induced velocities due to the lift of the wing.

Table 3.10: Propeller input modelling description with respect to state variables

Variable description	Modelling description	Simplifications
Wing induced velocities	The wing lift distribution is obtained using the aforementioned lifting line method in Section 3.1. The lift distribution depends on α, p, V_∞ and ρ, where the last two are used to calculate Re. V_∞ is also used to obtain the induced velocities V_{ind}.	Effect of the propeller on the wing lift distribution is neglected.
Propeller inflow speed	Equal to V_∞. Is used to nondimensionalise the wing-induced velocities.	Total airspeed changes due to p, q and r are neglected so the velocity inflow field remains the same as assumed. These effects are small in comparison to V_∞.
Propeller advance ratio	Depends on the local true airspeed of the propeller and the rotation speed of the propeller. The local true advance ratio is obtained by correcting the free-stream airspeed using r, as in Equation (3.9).	-
Propeller angle of attack	Must be a total, absolute angle of attack. It depends on the angles α, β_s, ϵ_{TMP}, and the angle resulting from p. All these angles are compiled to a single absolute propeller angle of attack.	As the effect of q is marginal due to the small moment arm, it is neglected. Since the contribution of r to the total velocity is neglected, the contribution in the total angle of attack is neglected as well.

Now that the modelling and implementation is described, the mathematical relations that are implemented into the flight mechanics model are presented here. All parameters that are an input for the dataset resulting from (3.4), are listed below. As said before, the dataset is generated for the right wing tip only. Therefore the following list will describe how the inputs are linked for the right wing tip. For the left wing tip v, p, r is the right tip value multiplied by -1. The subscript t denotes the tip, where the axis system is oriented as a body fixed frame, yet translated to the wing tip.

- α : From Equation (3.5).
- V_∞ : From Equation (3.6).
- p : From aircraft state.
- α_p : The total propeller angle of attack is obtained from Equation (3.7), where the subscript t denotes the wing tip. u, v, w are obtained from Equation (3.8).
- β_p : From the input variables.
- J : From Equation (3.9), where n and D are input variables.

$$\alpha = \arctan\left(\frac{w}{u}\right) \tag{3.5}$$

$$V_\infty = \sqrt{u^2 + v^2 + w^2} \tag{3.6}$$

$$\arctan\left(\frac{\sqrt{v_t^2+w_t^2}}{u_t}\right) \tag{3.7}$$

$$\begin{aligned} u_t &= u * \cos(\epsilon_{TMP}) - v * \sin(\epsilon_{TMP}) \\ v_t &= u * \sin(\epsilon_{TMP}) + v * \cos(\epsilon_{TMP}) \\ w_t &= w + p \cdot b/2 \end{aligned} \tag{3.8}$$

$$J = \frac{v_\infty - r \cdot b/2}{n \cdot D} \tag{3.9}$$

Resultant Force and Moment in Aircraft Body Frame

Propeller thrust T, normal force Y and power P can now be calculated. Since the dataset only contains values at the nodes of the dataset, the values need to be interpolated. This is done linearly by Matlab, using the built-in function griddedInterpolant[6]. If the aircraft goes outside of the range determined by the dataset, values are extrapolated only if at least the last two entries of the dataset in that axis are filled.

These values returned by the dataset are magnitudes without a direction. The forces are decomposed in the propeller reference frame by Equation (3.10). To avoid a singularity in Simulink, the decomposition of Y is only used if it is larger than 1e−13.

Now they need to be rotated back to the body fixed frame. This is done using Equation (3.11). Corresponding moments are evaluated using Equation (3.13), where the tip mounted force is defined as in Equation (3.12). For the left wing, Y_b is multiplied by -1.

$$\begin{aligned} X_p &= T \\ Y_p &= \begin{cases} Y \cdot \frac{v_t}{\sqrt{v_t^2+w_t^2}}, & \text{if } Y \geq 1\text{e}{-13} \\ 0, & \text{otherwise} \end{cases} \\ Z_p &= \begin{cases} Y \cdot \frac{w_t}{\sqrt{v_t^2+w_t^2}}, & \text{if } Y \geq 1\text{e}{-13} \\ 0, & \text{otherwise} \end{cases} \end{aligned} \tag{3.10}$$

$$\begin{aligned} X_b &= X_p \cdot \cos(\epsilon_{TMP}) - Y_p \cdot \sin(\epsilon_{TMP}) \\ Y_b &= X_p \cdot \sin(\epsilon_{TMP}) + Y_p \cdot \cos(\epsilon_{TMP}) \\ Z_b &= Z_p \end{aligned} \tag{3.11}$$

$$\vec{F_{TMP}} = \begin{pmatrix} X_b \\ Y_b \\ Z_b \end{pmatrix} \tag{3.12}$$

$$\vec{M_{TMP}} = \left(\vec{r_{TMP_{left}}} - \vec{r_{cg}}\right) \times \vec{F_{TMP_{left}}} + \left(\vec{r_{TMP_{right}}} - \vec{r_{cg}}\right) \times \vec{F_{TMP_{right}}} \tag{3.13}$$

The output force and moment of these equations can be readily used as an input for the original Simulink Piper Seneca model.

The whole method described above has another benefit. The TMP forces and moments are implemented as a module, which can be easily enabled, disabled and parametrised. This makes it easy to implement on any other aircraft that is defined in Simulink. Furthermore, since the original model is untouched, the relations between the verified and validated aircraft model, and the propeller model are very clear. This enhances confidence in the model's accuracy, as the neglected influence of the propeller on the rest of the aircraft is small.

On the other hand, this limits the ability to parametrise aircraft parameters in the model. The original model is based upon Ref. [24], which does not state the fashion in which all force and moment coefficients are obtained. Therefore, if any changes to the aircraft itself are wished to be made, all other parameters have to be re-evaluated.

[6] `https://nl.mathworks.com/help/matlab/ref/griddedinterpolant.html`; Accessed 29-12-2019

3.3.1. Verification by a Trim Analysis

The flight mechanics model is verified by selecting multiple points from a flight path, and calculating the inputs for the TMPs by hand from the aircraft's state. The values found matched the ones that were used as input for the propeller forces in the model. Then, the dataset interpolation at these points was compared with values from Python, which also were the same. Finally, the resultant forces and moments for both the left as right are cross-referenced in Python and Matlab. These matched as well.

To see whether the new forces were integrated correctly in the trim module, a trim analysis is performed. In Figure 3.27 one can see trimmed required roll angle ϕ for a steady side-slipping flight with β_s= 20[deg] on the left, and the trimmed flight path angle for β_s= 0[deg] on the right, where in both cases the original engines are set to idle. In both analysis the blade pitch β_p is varied as the control variable for the propeller. The flight speed is set to 40 m/s, corresponding to the landing speed. The dotted line indicates the trimmed angle of the original aircraft, denoted by a propeller diameter of 0 in the legend.

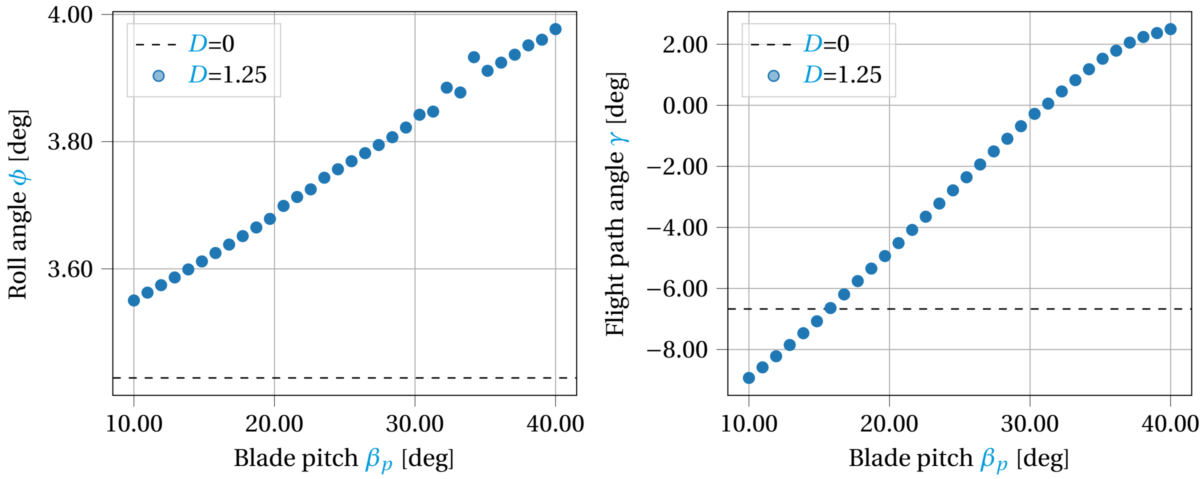

Figure 3.27: Trimmed flight angle variations due to β_p

In the left figure, where the roll angle is denoted, one can see that more roll angle is needed with respect to the original aircraft, irrespective whether the propeller is generating thrust or drag. More thrust does indicate more roll angle in a linear fashion, which is favourable for control purposes as stated in Ref. [58]. At propeller pitch angles between 30[deg] $\leq \beta_p \leq$ 35[deg] the trimming routine attains other local minima, where apparently the normal force in the dataset is a bit lower. Since the rest of the graph is so extremely linear, outliers are spotted quickly and will not form a problem.

The right figure shows the trimmed flight path angle without any sideslip. The minimum attainable glide slope gives an idea of TMP as air brakes. According to the slope of the graph when approaching β_p= 10 deg, the slope can be even lower if the propeller is set to a finer pitch setting.

4

Analysis of Propeller Force Inputs

The model to obtain propeller forces in Section 3.2 is evaluated, resulting in a 7D dataset. This dataset will be applied to the flight mechanics model. In order to understand what is happening in the flight mechanics model, we need to understand the sensitivity of the propeller forces to the different variables considered. These variables are defined in the previous chapter, and are as follows:

- α, wing angle of attack
- V_∞, magnitude of the free-stream velocity
- p, aircraft roll rate around the x-axis in the body frame
- D, propeller diameter
- α_p, local propeller angle of attack
- β_p, propeller blade pitch
- J, propeller advance ratio

This chapter will provide insight into the behaviour of the propeller dataset, and discuss its viability and limitations. Then the forces will be converted to a yawing moment, to discuss the control force potential of tip-mounted propellers.

4.1. Parametric Propeller Force Dataset Visualisation

The forces dataset that is passed to the flight mechanics module is a 7D table. If the dataset is simply integrated to the flight mechanics model, the table becomes a black box. Therefore it is important to verify the found values, and to locate potential flaws.

To see the influence of different parameters on the resulting propeller force, a parametric sweep is done along all the seven axes. Since propeller parameters might give a different behaviour in different flight situations, multiple flight cases are evaluated. During flight the speed will vary, which is why a slow and a fast case are evaluated. However, as the propeller might be counter- or co-rotating with respect to the wing-tip vortex (explained in Section 2.2), the two rotation senses are evaluated as well. This will therefore lead to four different cases:

- Slow flight (40 m/s), counter-rotation
- Fast flight (80 m/s), counter-rotation
- Slow flight (40 m/s), co-rotation
- Fast flight (80 m/s), co-rotation

The corresponding flight speeds have been obtained from the Piper Seneca aircraft manual [26], where the slow speeds are obtained from the landing phase, and fast speeds from the fast cruise point. At these typical flight points, the sensitivity to parameters is the most important. This is indicated by the equations in Section 2.4.3, where the simplified linearised eigenmotion solutions indicate what force and moment derivatives influence the eigenmotions. To show the force variation throughout the range of the dataset, one parameter is varied over the range of the dataset, and the other variables are kept constant at some predefined point in the dataset. This is insightful, yet will not offer insights in the interactions between parameters. All ranges are composed in such a way that the entire flight envelope should be reachable. The ranges and initial values are tabulated in Table 4.1. Initial, mid point values are determined arbitrarily, such that feasible numbers will be obtained.

Table 4.1: Initial values and bounds for propeller dataset

	Unit	Low speed	High speed	Range min	Range max
α	[deg]	5.0	0.0	0.0	15.0
V_∞	[m/s]	40.0	80.0	30.0	80.0
p	[rad/s]	0.0	0.0	-0.52	0.52
D	[m]	1.25	1.25	0.5	2.0
α_p	[deg]	0.0	0.0	0.0	60.0
β_p	[deg]	30.0	40.0	10.0	40.0
J	[-]	0.9	1.4	0.4	2.5

All parameters are nondimensionalised in the upcoming visualisation. This is done by applying Equation (4.1), where f is the parameter fraction, and p_{eval} is the to-be evaluated parameter value. Since this parameter fraction will be used throughout the thesis, let us review its working with a short example. In Table 4.1 the range for α is defined from 0 [deg] till 15 [deg]. For this parameter, $f = 0$ denotes the minimum of the range, hence 0[deg]. On the other hand, $f = 1$ denotes the maximum point of the range, 15[deg]. A value of $f = 0.33$ would result in $\alpha = 5$[deg].

$$f = \frac{p_{eval} - p_{min}}{p_{max} - p_{min}} \tag{4.1}$$

Figures that result from this sensitivity analysis can be found throughout Figures 4.1 - 4.4. All data points are indicated with a marker. One should note that the gradient due to some variable should always be interpreted with respect to the range it is defined on. If in one of the graphs a line shows a steep gradient, this might be due to a large range for that parameter.

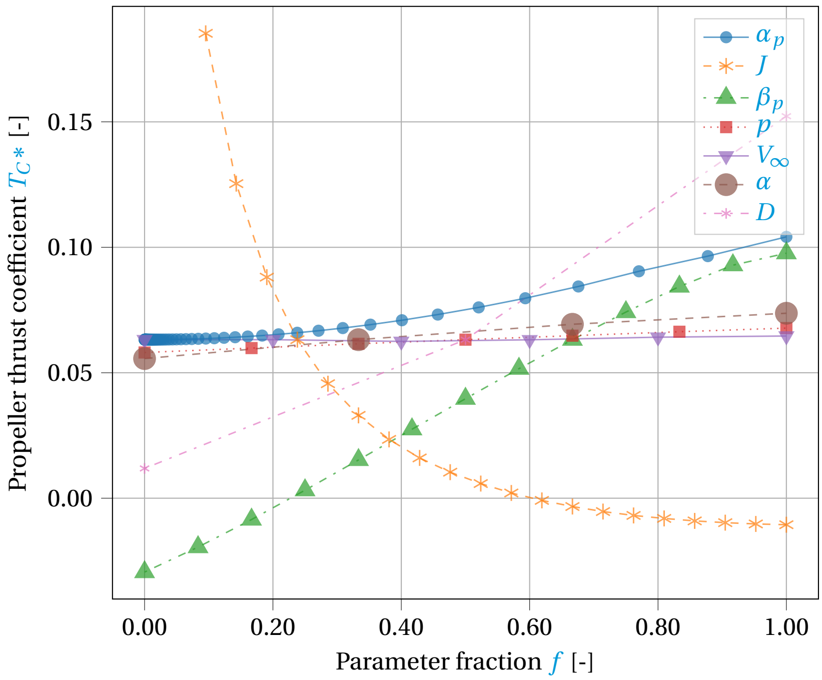

Figure 4.1: Low speed counter-rotating propeller force parameter sweep

The results provided in Figure 4.1 follow the expected trends. Table 4.2 summarises the trend for each parameter individually. When applying the expectations from this table with the aforementioned figure, all of the listed points behave as expected. At high β_p the T_C* response curve becomes curved due to stall onset.

Furthermore, at low J either no solution was found, or it was limited by the boundaries as defined by Table 3.6, where a confidence-region was defined for β_p and J combinations.

Table 4.2: Expected parameter effect on propeller thrust force for counter- and co-rotation

Parameter	Propeller force influence
α	A higher angle of attack will increase the local lift coefficient on the wing sections. Since the lift distribution will go to zero at the tips, the decay in lift distribution towards the tip will be stronger. This will result in a stronger tip vortex. Since the propeller is rotating in an opposite sense to the wing tip vortex, this will in turn increase the local blade angle of the propeller, and hence increase the thrust. In a co-rotation case, the opposite is expected.
V_∞	T_C* is nondimensionalised. The impact of V_∞ is therefore expected to be limited. However, as the flight speed does influence the Reynolds number, T_C* might change with V_∞. As generally a higher Reynolds number leads to a higher C_L, the circulation of the tip vortex will be increased. Furthermore, as the advance ratio is kept constant in this analysis, and the flight speed increased, the Reynolds number of the propeller will go up as well. This might also lead to additional thrust.
p	As the propeller is only evaluated at the right wing tip, the more positive p, the higher the local α at the right wing tip. As the wing tip vortex increases in strength with increasing α, the thrust is expected to increase with roll rate. The opposite will happen for the co-rotating case.
D	Increasing diameter will increase the propeller disk area. If all geometric and inflow properties stay the same, this will also scale the thrust. Also, if the diameter gets larger, the the tips of the propeller will be farther away from the wing tip vortex core. Since the propeller gains thrust performance with enhanced tip circulation, the farther away from the wing tip vortex core, the less thrust on that blade section. Therefore, enhancement of the propeller performance will degrade with increasing propeller diameter. If the propeller performance is degraded by the tip vortex, increasing the diameter will increase propeller performance.
α_p	The thrust is expected to increase with the local angle of attack on the propeller, following the applied empirical formulae obtained from Ref. [38].
β_p	The higher the blade pitch, the higher the local angle of attack on any blade section. Therefore the thrust of the propeller is expected to increase with blade pitch, until the blade section begins to stall. This stalling can happen for both positive and negative inflow angles. So stall can occur at both high and low β_p values.
J	Thrust decreases with increasing advance ratio, as the average inflow angle on the blade decreases.

Figure 4.2 shows a slightly sparser dataset. This is an indication to a limitation of the approach used. If values are out of bounds according to the N250 propeller limits as defined by Table 3.6, or were not solvable nor interpolatable, nan values are returned by the dataset. This occurs for example at low J values. Since T_C* due to some α_p is calculated from C_T at the effective advance ratio $J \cdot \cos\alpha_p$ as defined in Equation (2.7), the curve of α_p is also limited. With respect to the slow curve, the effect of p has decreased. This is because the parameter p is given as a dimensional parameter to the dataset creator. The nondimensionalised version $p \cdot b/(2 \cdot V)$ would have been better, yet the line that can be fitted through these points (for the slow case in Figure 4.1) is so straight that extrapolation is believed to be reliable. Since α is a nondimensional value, its effect is maintained for this fast case. One should note that the evaluated points are all parameter sweeps from some midpoint. Hence since β_s is now set to 40 [deg], low J values are not attainable. However, if the blade pitch is decreased, lower advance ratios will become available.

In the co-rotation case, the whole dataset is shifted down, since the propeller now rotates with the tip vortex instead. This is detrimental to the thrust, yet boosts the performance in the drag regime.

The trends for the input parameters are the same for co-rotation, except for α and p. The T_C* variations due to the input parameters are depicted in Figure 4.3. With increasing angle of attack, the tip vortex becomes stronger, and since the propeller is now rotating along with the tip vortex, the thrust will decrease. The same holds for p.

Figure 4.4 provides us with another insight. If the D line is followed, a slightly sharper slope change with increasing D than in Figure 4.2 is observed, hence the sensitivity of T_C* with D has increased. This can be explained that the tips of the propeller blade reside in air that is less influenced by the tip vortex, hence air

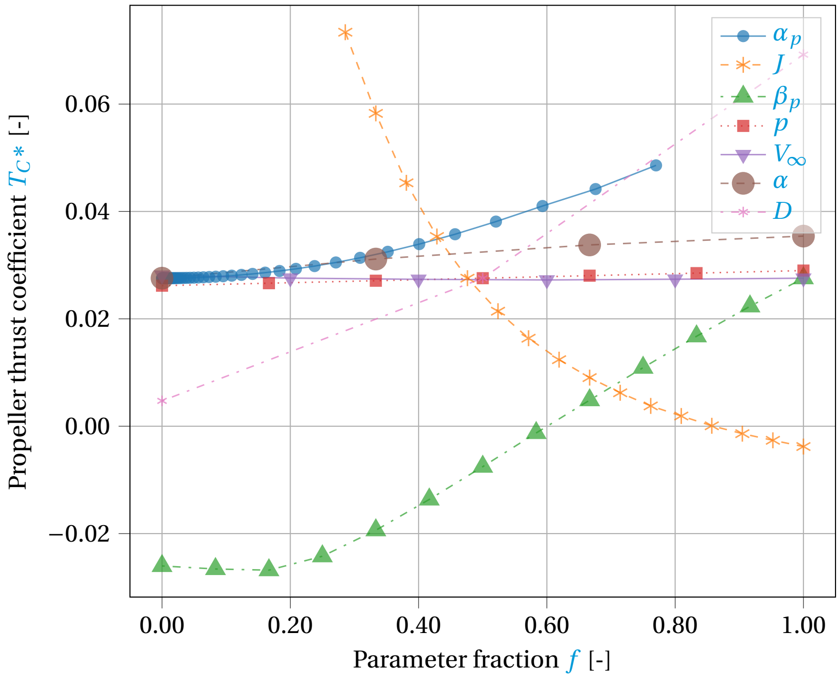

Figure 4.2: High speed propeller force variations, counter-rotation

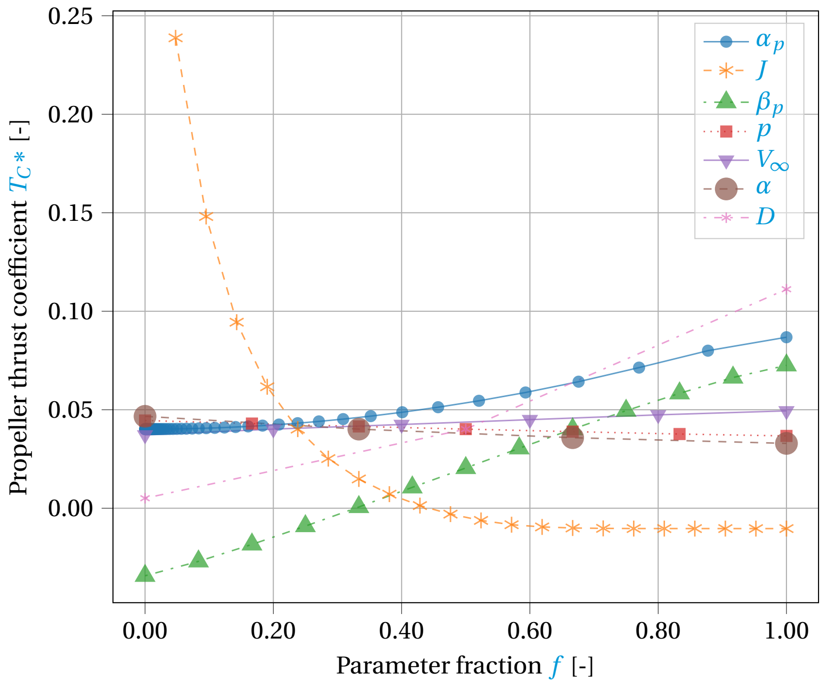

Figure 4.3: Low speed propeller force variations, co-rotation

with less negative effects of co-rotation, resulting in more thrust.

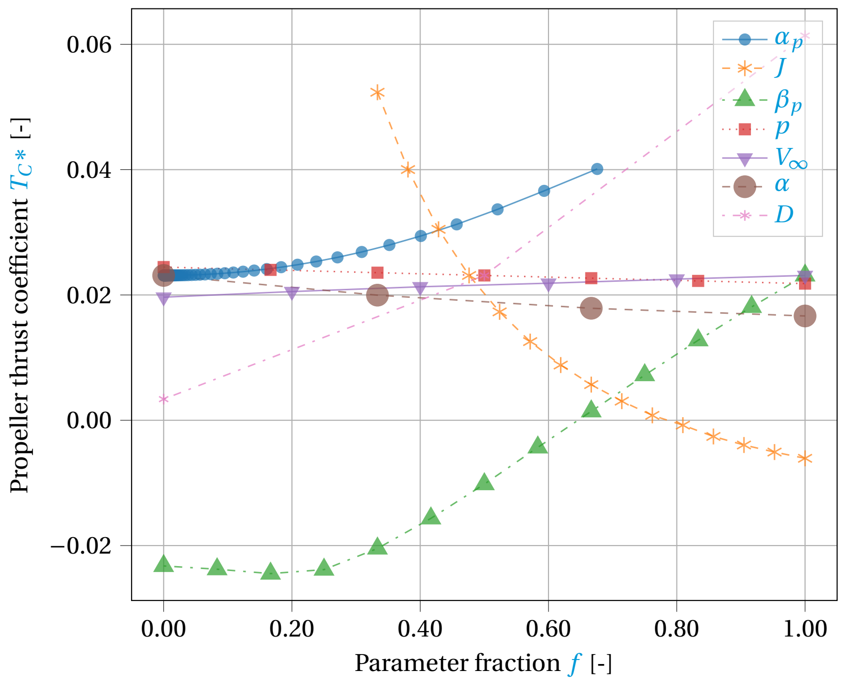

Figure 4.4: High speed propeller force variations, co-rotation

Since the parameters behave as expected, confidence is built to use these propeller forces in the upcoming analyses. As the magnitudes of the forces is now known, we can review the validity of the assumptions made to enhance our confidence in the propeller forces.

4.2. Assumptions Review

Now that the propeller forces are calculated, we can reflect on the assumptions stated in Section 3.3. In order to do so, a typical situation is chosen and evaluated to see whether the violation of the assumptions is within reasonable bounds. One has to note that this section is not meant as a definitive proof that the assumptions hold, yet more as a sanity check. Wherever applicable, simulations are done in this section with the original wing of the Piper Seneca, and/or the N250 propeller with D= 1.25[m].

Propeller influence on wing flow

As the propeller is situated behind the wing, the influence of the propeller on the aerodynamic forces on the wing is considered to be limited [45]. This assumption has effect on the lift and drag of the tip of the wing. The drag of the wing itself will affect the flight performance most and have limited effect on the stability and control behaviour. Therefore, we will focus on the wing lift change. A simple and rough calculation of the wing lift change and its implications will follow.

The lift change of the wing due to added velocity of a single TMP, hence for either the left or right tip-mounted propeller, can be calculated using Equation (4.2), where K denotes the fraction of total speed change occurs at the aerodynamic centre of the airfoil. As half of the airflow speed change occurs before the propeller, and half after, in the worst case K = 0.5. Since the top part of the fraction is largest when the aircraft is flying slow, an airspeed of 40 [m/s] is used in the following analysis.

$$\Delta L = \frac{D\left((V_{\text{inf}} + K \cdot \Delta V)^2 - V_{\text{inf}}^2\right)}{4} \rho C_L c \tag{4.2}$$

$$T = \dot{m} \cdot \Delta V \tag{4.3}$$

Combining this equation with Equation (4.3) for the speed change ΔV, and taking a total thrust of 2000[N], combined with a slow-flying cruise C_L = 1.05 at ground level, the change in lift is 971[N], which is 4.9% of the total wing lift. In symmetric situations, this is then comparable to a change of $\Delta\alpha = \Delta C_L / C_{L_\alpha} = (1.05 \cdot 0.049)/0.11 = 0.46$[deg]. Considering that this evaluation is the most extreme case encountered, neglects that the lift coefficient at the tips will drop, and takes the maximum value possible for K, this angle of attack change is considered small and hence negligible. The value of 2000[N] comes from taking the reference mass of the aircraft (2000[kg] [26]), dividing over a lift over drag ratio of 10. Now, considering that the increase in c_l for the wing section that is affected by the pusher propeller is limited to 0.2 according to Ref. [45], where the effect on c_l for a pusher propeller with a larger diameter than the chord was tested with take-off thrust settings, whereas in our example the c_l has increased with 1.05, the assumed factor K is greatly overestimated. Since even in the most extreme case the influence is negligible, the assumption is considered valid.

For an asymmetric case, only one engine provides the aforementioned thrust, and the other one zero thrust. Since the aircraft will now roll due to the asymmetric lift distribution, it is convenient to express the correcting roll moment by what angular roll velocity would be needed to achieve the same effect. Therefore balancing the moment due to roll velocity and the asymmetric lift results in Equation (4.4), assuming that the lift force for one semi-wing acts at $b/4$.

$$(\Delta C_L) \cdot \left(\frac{b}{2}\right) = 2 \cdot \left(p \cdot \frac{b}{4} C_{L_\alpha}\right) \cdot \left(p \cdot \frac{b}{4}\right) \tag{4.4}$$

Solving this equation for the roll rate yields p= 0.16[deg$\cdot s^{-1}$]. This is very small in comparison with the roll moment created due to the resulting yaw moment that this assumption is considered valid, especially considering the over-estimation of K.

Propeller angle of attack

According to the lifting line theory, the wake extends in the direction of the free-stream. Therefore the wing-tip vortex will extend in the direction of the free-stream. A suitable approximation might be to assume that the average angle of attack for a propeller in the wing tip vortex is equal to the free-stream angle of attack. To check this assumption using the lifting line theory, would yield a trivial case: Only right behind the lifting line, where the circulation due to the lifting line is strong, the flow would bend downwards, and follow the free stream afterwards.

Therefore, the angle of attack behaviour right behind the wing is checked for a single case using the CFD case from Section 3.1.3. The wing is subjected to α= 3 deg. In Figure 4.5 the local angle of attack is plotted in a polar plot, along a circle with $R = 0.47$[m]. The plot is drawn as a rear view image, and the centre of the image is located at the right wing tip. α is calculated by $\arctan(V_z/V_x)$. One can see that at the right of the image, the local angle of attack is more than six degrees, where the tip vortex increases the up wash. On the other hand, at the left part of the image, the angle of attack is -2 degrees, where the tip vortex enhances the down wash. One can see that, at the left hand side, the local angle of attack increases quickly below the wake. When averaging the angle of attack, an angle of attack of 3.2[deg] is returned. Therefore, one can say that in this case the global angle of attack is roughly the same as the angle of attack at the propeller disk.

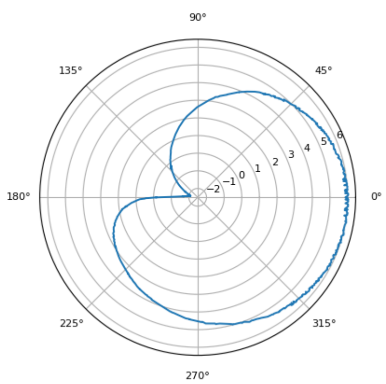

Figure 4.5: Polar graph of local α where $R = 0.47$[m], at right wing tip, rear view. Global α= 3 deg

This reference case is believed to be representative for the cases that have been evaluated in this thesis. The check here is just a single check, and it is not believed to be completely verified. However, since the average angle of attack is even more than the free-stream angle of attack, the assumption that the inflow on the propeller would always be parallel to the trailing edge of the wing is incorrect in this case. Furthermore, the velocity field change due to the tip vortex is far greater than the effect of this average angle of attack. Therefore, the effect of this assumption is small in any case. As for this case the free-stream angle of attack is close to the CFD solution, the assumption is considered acceptable for non-stalled attached flows.

Propeller yaw angle equals aircraft yaw angle

The trailing vortex sheet of a wing induces a flow outward over the top of the sheet, and inward over the bottom of the sheet. Therefore one could argue that yaw that the pusher propeller sees would be the same as the whole aircraft sees. As Figures 4.6 and 4.7 indicate, this is indeed the case.

This figure is set up in the same fashion as Figure 4.5, yet now denoting β_s. At the right side of the figure, one can clearly see the cross-over from outflow (lower β_s) to inflow (higher β_s), where $\beta_s = -V_y/V_x$. At the right hand side, the transfer is pushed down a bit by the downwash of the wing.

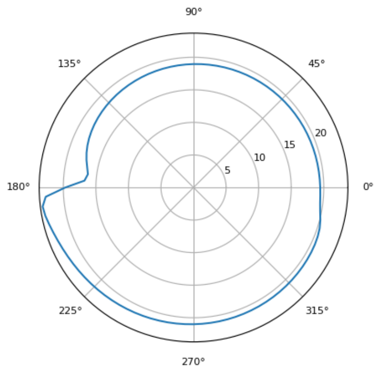

Figure 4.6: Polar graph of local β_s where $R = 0.47[m]$, at left wing tip, rear view. Global $\beta_s = 20\,\mathrm{deg}$

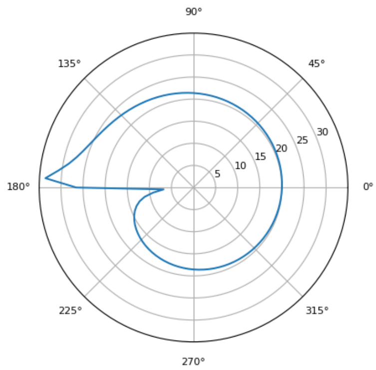

Figure 4.7: Polar graph of local β_s where $R = 0.47[m]$, at right wing tip, rear view. Global $\beta_s = 20\,\mathrm{deg}$

The assumption used will be valid as long as the inertial forces are more prominent on the airflow than the viscous forces. Therefore, for high Reynolds numbers, the assumption is considered to be valid. In the remainder of this thesis encountered Reynolds numbers are such that inertial forces dominate.

Yaw-rate's effect on the propeller

The effective advance ratio is changed in the model due to yaw rate, however the lift distribution along the lifting line is not. Therefore, to prove that this effect is small, the same tip mounted propeller is evaluated in two situations: One where the lifting line is a solution for some yaw rate, and one where this effect is neglected. The resulting thrust coefficients are shown in Table 4.3.

Table 4.3: Thrust coefficient variation with yaw rate

	No yaw rate	Yaw rate included
Yaw rate r [deg/s]	0.00000	-20.00000
C_T	0.31971	0.32228

As one can see, the C_T variation is less than 1%. This is comparable to the error obtained when evaluating the different inflow fields in Table 3.4. To place this value into context, refer for example to Figure 4.1. The variation in T_C* due to J is far larger than this minimal error concluded upon here. The largest effect is therefore believed to be captured. Furthermore, adding an extra dimensions would increase the size of the propeller dataset, and thereby significantly increase the amount of time needed to evaluate it. For this thesis, as 1% is a very small error taking into consideration the magnitude of forces involved, this assumption is deemed acceptable as well.

Now that all assumptions have been briefly checked for their validity in cases that are likely to be encountered in the rest of the thesis according to the situations sketched in this chapter, we can proceed and simulate the flight mechanical behaviour of the propellers when applied to a reference aircraft.

4.3. Propeller Forces' Contribution to Control

The propeller force can be used as directional control force. This would then indicate whether the aircraft can be controllable in certain situations, hence if enough control power is available. This control force can be directly related to the amount of directional control force the rudder is able to produce. Since the thrust force available in the recuperating power regime is important for failure safe modes, forces of the propeller will be depicted for all available power settings, with a contour drawn in the image to indicate the negative power regime. As J and β_s are viewed in this section as the input variables for control with a tip-mounted propeller, the other five parameters are constant at the same values as in the previous section, as defined in Table 4.1.

Using Equation (4.5) the propeller forces are converted to $C_{n_{TMP}}$, which is the nondimensional yaw moment coefficient due to TMP thrust. It is obtained by multiplying the propeller thrust by the semispan, which is the moment arm of the TMP.

$$C_{n_{TMP}} = \frac{Tb}{2qSb} = \frac{T}{2qS} \tag{4.5}$$

$$K_p = \frac{P_{req}}{P_{ref}} \tag{4.6}$$

In Figures 4.8 - 4.11 the yaw moment coefficients have been plotted with respect to the inputs β_p and J. The resulting values are only for the right tip-mounted propeller, where all forces on the left engine are equal to zero. Contour lines are indicating the calculated power needed by the propeller, as fraction K_P. This fraction K_P is defined as the input power required on the tip-mounted propeller with respect to the power that is available on a single engine of the reference aircraft. This factor is calculated using Equation (4.6), where P_{req} denotes the required input power to the tip-mounted propeller, and P_{ref} denotes the reference power of the original Seneca engine. This reference power is rated at $P_{ref} = 200$[BHP] [24, 26]. One has to note that the figures are made for a tip-mounted propeller of D= 1.25[m], whereas the propeller on the original engine has a diameter of 2[m]. To place the resulting $C_{n_{TMP}}$ into perspective, the average $C_{n_{\delta_r}}$ of the Piper Seneca is $-0.00095[\text{deg}^{-1}]$, and the maximum rudder deflection is 35 deg [24]. Therefore, the maximum C_n attainable by the rudder is ±0.03325.

When comparing the scales of all four figures, one can see that the range of $C_{n_{TMP}}$ is larger for lower speeds than for higher speeds. However, when the speed is high, the available range of positive values for $C_{n_{TMP}}$ is larger compared to lower speeds. This is as expected, as a positive $C_{n_{TMP}}$ indicates negative thrust on the right engine, which is easier to achieve at high speeds.

In Figures 4.8 and 4.10 the maximum absolute control power for a single propeller is three to four times as effective as the conventional rudder. One has to note that this is without taking the required power into account. More feasible would be to suggest that K_P has to be smaller than 1, indicating that the tip-mounted engine would have the same power available as the reference engine. This would yield a negative $C_{n_{TMP}}$ of -0.06.

In order to get the same yaw control power as the rudder, the yaw moment coefficient, summed for both engines, has to be $C_{n_{TMP}}$= 0.03325. From the previous analysis we know that matching the reference yaw moment with TMP possible, yet attaining this reference yaw moment with a feasible power setting is. Let us therefore review whether matching the reference maximum rudder yaw moment with TMP is feasible with respect to the power needed, expressed as a fraction of the reference aircraft's engine power K_P. The drag-generating engine can obtain a value of around 0.01 at J= 1. and β_p= 10[deg]. To then get the remainder, one needs to add thrust with the other engine. Since $C_{n_{TMP}}$ would have to be around 0.025, a value of around K_P= 0.2 is needed. Hence, matching the rudder control power of the reference aircraft is feasible with TMP for this slow case.

At high speeds the control power needed is easier obtained from a drag-generating propeller. According to the most positive value on the scale of Figure 4.9, $C_{n_{TMP}}$= 0.018 as maximum value. This leaves 0.015 to be obtained from the thrust generating engine. For K_P= 0.5 this seems feasible. However, any thrust needed to maintain cruise then has to be provided by other engines. Therefore, from this analysis, only if the required thrust for cruise is provided by some other means than TMP, using TMP as the only means of control is feasible.

If an engine is unable to produce thrust, only the regimes between the K_P= 0 lines can be used for control. This is assuming that both engines are restricted to negative input powers. For low speeds a single engine $C_{n_{TMP}}$ reduces to only a third of the maximum rudder yawing moment coefficient. Therefore, if one would only use TMP for directional control, control would be seriously limited in a OEI situation. It would

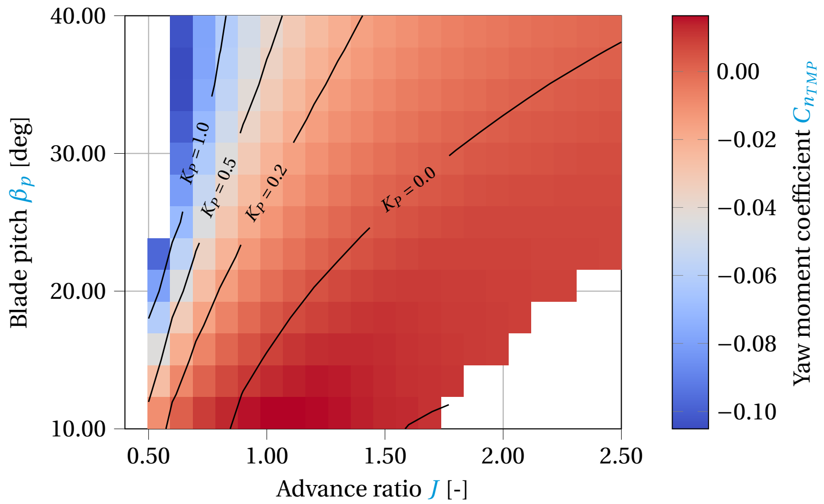

Figure 4.8: Low speed counter-tip-vortex rotation yaw moment coefficient map due to right TMP where K_P is the power fraction of the reference engine

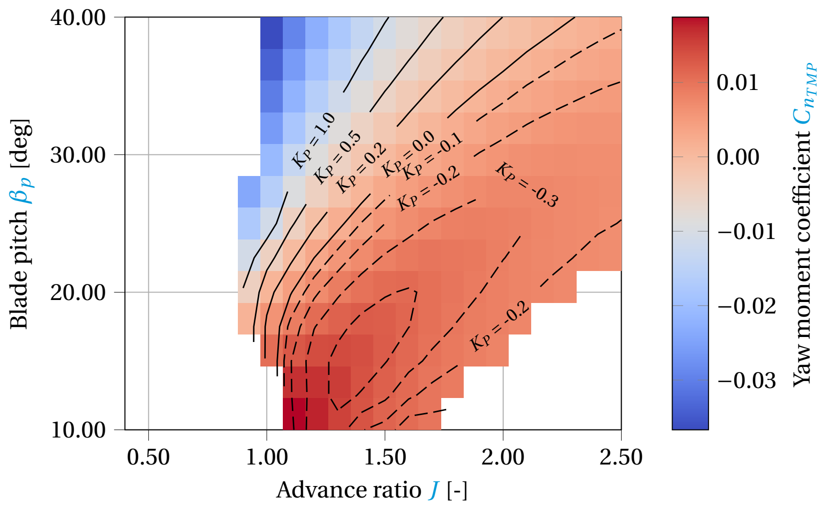

Figure 4.9: High speed counter-tip-vortex rotation yaw moment coefficient map due to right TMP where K_P is the power fraction of the reference engine

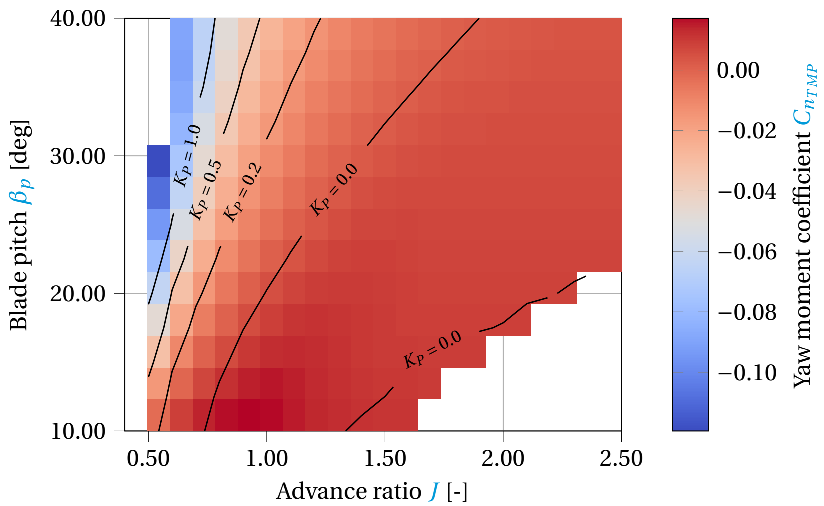

Figure 4.10: Low speed co-tip-vortex rotation yaw moment coefficient map due to right TMP with a where K_P is the power fraction of the reference engine

be a smaller issue in the high speed case, as the maximum $C_{n_{TMP}}$ is 0.018, which is more than half the original maximum rudder yaw moment coefficient. A possible workaround would therefore be to simply fly faster in OEI situations by increasing the descent angle, and accepting that the maximum control forces have degraded.

The co-rotating propellers in Figures 4.10 and 4.11 have more J and β_p combinations within the negative power regime, since this sense of rotation is more efficient when recuperating, as determined in Section 2.2. The maximum $C_{n_{TMP}}$ does not differ much from their counter-rotating counterparts. Therefore, if the sense of rotation would be set to co-rotation on descent, this would be done for more power output only, since the yaw moments that can be generated do not increase. If the thrust generating values are taken into account, the maximum $C_{n_{TMP}}$ has decreased as the engines can simply provide less thrust in the co-rotating case.

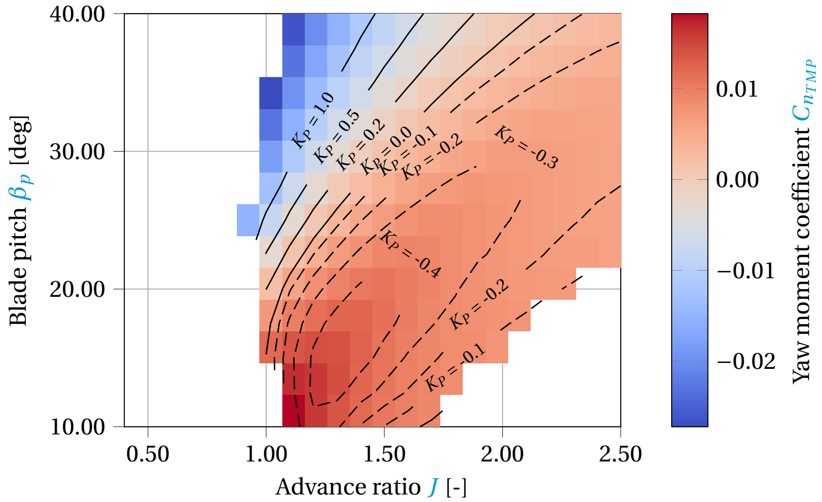

Figure 4.11: High speed co-tip-vortex rotation yaw moment coefficient map due to right TMP with a where K_P is the power fraction of the reference engine

The previous analyses show that tip-mounted propellers can be used as control devices. The effectiveness depends on the airspeed, the maximum power of the engine and the magnitude of the demanded yaw moment. If the engines are not necessarily required to provide thrust for sustained flight, the method seems feasible. However, if this is not the case, it will be up to the designer of the aircraft whether the TMP direction control authority is sufficient or not. If the designer decides that the available control power is insufficient, a hybrid solution of TMP and some other directional control actuating system can be implemented. As the maximal yaw moments attainable by the TMP configuration can enhance the reference maximum yaw moment, the rudder size can potentially be reduced.

5
Sensitivity Analysis of Stability Contribution

Stability is a requirement for an aircraft. If an aircraft is unstable, it will be impossible or uncomfortable for the pilot to fly. An aircraft also will not be certified if the aircraft is not statically stable longitudinally, or dynamically stable [58]. Therefore the effects of TMPs on the stability parameters of the reference aircraft will be reviewed in this chapter.

This is done in the same parametrised fashion as in Chapter 4. The variables for parametrisation are now the TMP geometric and control details: D, J, β_p and ϵ_{TMP}. First the chosen cases and parameter ranges will be explained, followed by an example of the fit method used to extract eigenvalues, after which the three eigenmotions and their corresponding analysis will follow.

The aircraft does not show the same behaviour in all flight situations. Since this is a first study to the non-linear behaviour of TMP on an aircraft, basic flight situations of cruise and descent are discussed. The slow- and fast flight cases are proposed in Chapter 4, and will be copied here. In that section, counter- and co-rotation cases have been discussed as well, where in this section only the counter-rotation case will be evaluated. The stability depends on the variation of a force due to some disturbance, hence the trend of a force with varying for example J. Since the trends for the different parameters in the counter- and co-rotation datasets have proven to be the same, except for a marginal influence of α and p, it does not seem worthwhile to embark on an investigative tour discussing marginal differences in stability for co- and counter-rotation cases. Since the tip mounted propellers can be used as spoilers, a recuperative condition might be interesting. Therefore cruise and descent cases will be evaluated.

To be able to do a parameter study, for each of the cases a suitable midpoint needs to be chosen, after which the ranges can be evaluated. The parametric fractions are evaluated as in Equation (4.1). The chosen midpoints and ranges can be found in Table 5.1. Since only three points exist in the dataset for the propeller diameter, this value is set to the middle value and is the same for all cases. The value of $D = 0$[m] is included, indicating no TMP, hence the reference case. For the cruise cases, a point is chosen where the thrust is just enough to sustain level flight, and where the power fraction of the engine K_P is smaller than 0.5. For the fast cruise case this was not possible, so the maximum thrust value with $K_P \leq 0.5$ is chosen. The descent cases have been chosen in order to extract maximum power from the airflow. The ranges are chosen in such a fashion that all values that are deemed realistic by the author are evaluated, or so far as the dataset permits.

Table 5.1: Parametric stability analysis midpoints and corresponding ranges

Phase	Unit	Cruise		Descent		Range min	Range max
V_∞	[m/s]	40.	80.	40.	80.	-	-
β_p	[deg]	30.00	40.00	12.50	15.00	10.00	40.00
J	[-]	0.90	1.80	1.20	1.40	0.40	2.00
D	[m]	1.25	1.25	1.25	1.25	0.00	2.00
ϵ_{TMP}	[deg]	0.00	0.00	0.00	0.00	-20.00	20.00

5.1. Static Stability Analysis

Static stability means that if an aircraft is in a steady flight, any disturbance will be corrected by the resulting forces and moments on the aircraft. For example, if the aircraft is subjected to a gust in v, which increases the angle of sideslip β_s, the resulting moment will be such that the β_s is decreased.

This will therefore result in a moment derivative due to some angle. The relevant moment is different for directional static stability than for longitudinal static stability. Both will be evaluated in the upcoming subsections. Derivatives are determined from the isolated propeller forces and its position with respect to the CG. Differentiation is done using the central differencing scheme. An example is given in Equation (5.1).

$$\left(\frac{\delta C_n}{\delta \beta}\right)_{\beta=0} = \frac{1}{\frac{1}{2}\rho V_\infty^2 S b}\frac{N_{\beta=\Delta\beta} - N_{\beta=-\Delta\beta}}{2\Delta\beta} \tag{5.1}$$

In the upcoming parametric analyses, the ranges and midpoint as defined in Table 5.1 are used. Especially the trend for this parameter sweep will be evaluated and discussed. As said before, the stability depends on the variation of forces while varying an aircraft state parameter. Since the propeller forces' variation due to inflow angles are the same for both thrust and drag-generating cases, by definition of the propeller incidence equations of De Young [38] and observed in Section 4.1, only the cruise cases will be evaluated for the static stability.

5.1.1. Directional

If an aircraft gets a positive sideslip angle, β_s becomes positive. To correct this motion, the nose should be pushed to the right, hence a positive moment. Therefore, $C_{n_\beta} > 0$ is necessary for directional static stability.

The reference aircraft is statically stable (otherwise it would not come through certification). If we assume that TMPs do not have an effect on the aerodynamic behaviour of the aircraft itself, C_{n_β} of the TMP aircraft would equal the summation of $C_{n_\beta ref}$ and $C_{n_\beta TMP}$.

This analysis results in Figures 5.1 and 5.2. Resulting curves are relatively smooth, yet especially at the end of the ϵ_{TMP} curves some small zig-zag patterns can be observed. This is due to the larger step size in ϵ_{TMP} for the propeller forces dataset at larger α_p. When the step size for determining the derivative ($\Delta\beta$ in Equation (5.1)) is smaller than the step size in the dataset, such zig-zag patterns can occur. This is why the pattern does not occur in the middle, as close to $\alpha_p = 0$[deg] the dataset is very dense according to for example Figure 4.1. As the trend shown is not broken, and the zig-zag small compared to the absolute value, this is not expected to give rise to any complications.

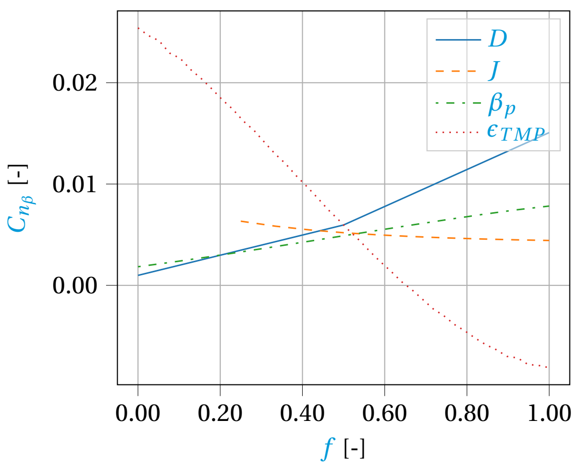

Figure 5.1: Slow cruise, TMP contribution to C_{n_β}

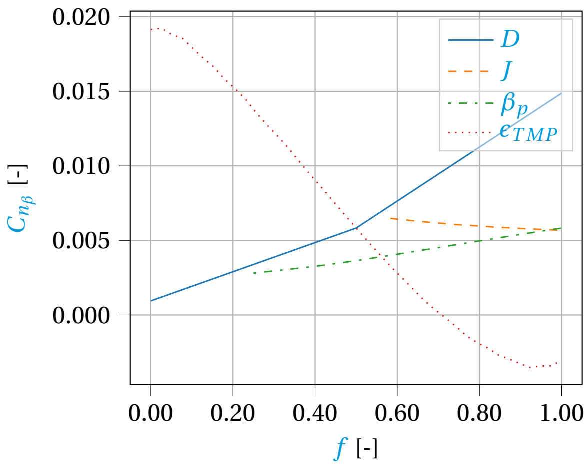

Figure 5.2: Fast cruise, TMP contribution to C_{n_β}

First of all, the magnitudes of C_{n_β} in the slow and fast cases are not equal. This is because the derivative is not nondimensionalised with respect to the propeller, but with respect to the aircraft parameters. This will imply that the flight mechanical behaviour of the propellers is different for both slow and fast cases.

In our case, the aircraft is fitted with pusher TMPs. Since a positive β_s will introduce normal forces on the engines to the left, which are located behind the CG, the correcting moment will be positive. This is indicated

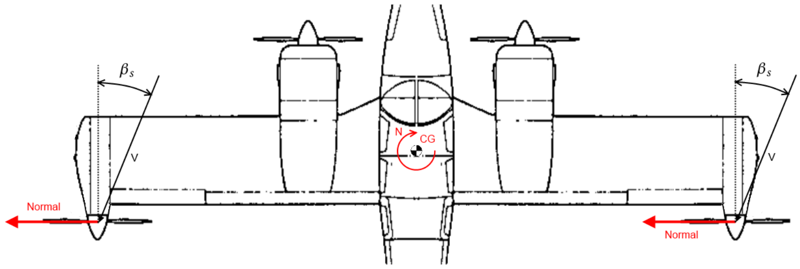

Figure 5.3: Restoring moment N due to positive β_s

in Figure 5.3. Hence, the mid-point contribution of the TMPs to C_{n_β} is positive. Let us shortly discuss the influence of the different parameters:

- ϵ_{TMP}: Larger α_p will amplify the thrust and normal force. For positive toe-in angles, for a positive sideslip, the left engine will decrease the angle of attack and the right engine will increase its angle of attack. Therefore the right engine will provide more thrust, and more normal force inward, and the left one the opposite. Therefore, if the thrust forces are dominant the resulting moment is negative, hence destabilising. When the normal forces are dominant (very high toe-in or toe-out angles), a toe-in angle will be stabilising.
- D: The diameter amplifies the absolute value of C_{n_β} by scaling the thrust and normal force. Whether increasing the diameter is stabilising or destabilising depends on the design point. If C_{n_β} is positive, increasing D will make C_{n_β} more positive, and vice-versa.
- β_p: Increasing the blade pitch increases the thrust and normal force slope with α_p, according to the empirical formulae incorporated [38], and is therefore stabilising.
- J: The advance ratio has a small effect on the thrust due to an angle of attack, and a larger effect of the normal force slope with α_p. High thrust values will increase both. Since increasing advance ratio decreases thrust, increasing the advance ratio is destabilising.

For all parameters the parametric sweeps show the same trends for all variables. The most apparent difference in the figures are the ends of the ϵ_{TMP} curves. According to the analysis above, where the lines are curving indicate a point where the normal forces are increasingly important. An optimum can be found for each flight situation with respect to ϵ_{TMP}.

To put the current numbers obtained into perspective, zero thrust $C_{n_\beta ref} = 0.000642[\text{deg}^{-1}] = 0.0368[\text{rad}^{-1}]$ for the reference aircraft for $\alpha = 4[\text{deg}]$ [24]. Therefore, the TMPs have a significant influence on the C_{n_β} of the whole aircraft, as the largest value of C_{n_β} found in Figure 5.1 is more than 67% of the aircraft's reference value.

5.1.2. Longitudinal

The same analysis as for directional stability is conducted, yet now for C_{m_α}. If a perturbation increases the angle of attack, this should be decreased. The pitching moment should therefore be downwards. This is a negative moment, hence $C_{m_\alpha} < 0$ for longitudinal static stability. Resulting figures from the analysis for both the slow and fast cases are shown in Figures 5.4 and 5.4 respectively.

Since the engines are positioned above the CG, an increase in α will increase the thrust (assuming that the aircraft flies at a positive angle of attack). This will push the aircraft over, hence produce a negative pitching moment which is stabilising. Furthermore, normal forces will increase, and also contribute with a pitch-down moment. Therefore, the mid-point contribution to C_{m_α} is negative. Let us, as with the directional static stability, shortly discuss the influence of the different parameters:

- ϵ_{TMP}: Larger ϵ_{TMP} will amplify the thrust and normal force, yet also decrease the propeller force in X_b. This force in X_b is a summation of the decomposed propeller thrust and normal forces. Therefore any increase in absolute ϵ_{TMP} will degrade the absolute C_{n_β} contribution, as in Figure 5.4. The opposite happens in Figure 5.5, since the propeller normal force variation is small with α_p (depends on T_C* according to De Young [38], which is lower now compared to the slow case). Due to this small normal force variation, the decomposed X_b force remains larger compared to the slow case. The slope of normal force variation does get bigger with larger α, as has been indicated in for example Figure 4.1, where the α_p curve get steeper on the right-hand side. Since the penalty on the X_b force is smaller,

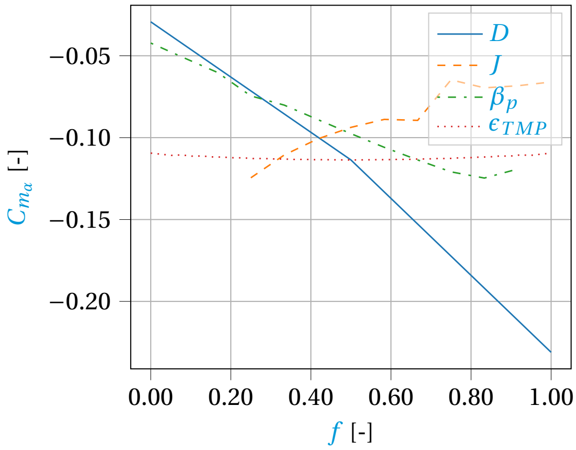

Figure 5.4: Slow cruise, TMP contribution to C_{m_α}

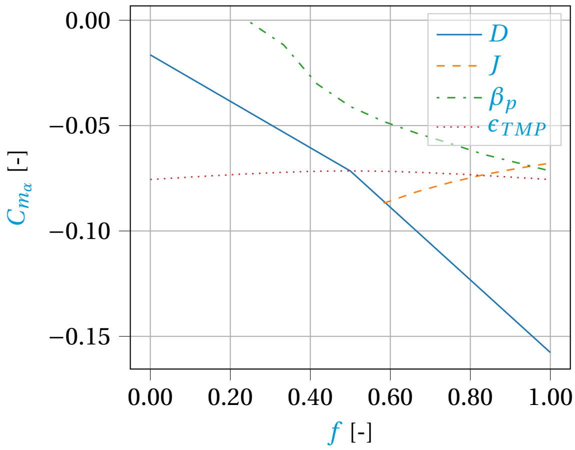

Figure 5.5: Fast cruise, TMP contribution to C_{m_α}

and the normal force slope get higher with α_p, increasing the absolute value of ϵ_{TMP} now actually increases the static stability. Therefore, for high T_C* values this parameter will be destabilising, and for low T_C* values increasing the absolute value for ϵ_{TMP} will be stabilising.

- D: The diameter amplifies C_{m_α} by scaling the thrust and normal force. Whether increasing the diameter is stabilising or destabilising depends on the design point. So if C_{m_α} is positive, increasing D will increase C_{m_α}, and vice-versa.
- β_p: Increasing the blade pitch increases the thrust and normal force slope with α_p, according to the empirical formulae incorporated [38], and is therefore stabilising.
- J: The advance ratio has a small effect on the thrust due to an angle of attack, and a larger effect of the normal force slope with α_p. High thrust values will increase both. Since increasing advance ratio decreases thrust, increasing the advance ratio is destabilising.

In this case, the last three variables yielded the exact same answer as for the directional stability case. The first variable, ϵ_{TMP}, did raise a very interesting issue, since the trend of increasing the absolute ϵ_{TMP} value in the slow case was opposite to the fast case. It has to be noted, in contrast to the directional stability, ϵ_{TMP} has a limited effect to C_{m_α}. The thrust variables are far more influential to C_{m_α}.

Figure 5.4 displays a kink in the line of J. According to Figure 4.1, $f = 0.6$ corresponds to the zero thrust value for $\alpha = 5$[deg]. Such a point is harder to solve for XROTOR, since both positive and negative local blade section lift coefficients can be obtained. This can lead to small sinus-like oscillations, and XROTOR may or may not converge to such a solution. The same holds for the β_p line in Figure 5.5, where just below $f = 0.4$ another non-linearity is indicated. This also corresponds to slightly negative values in Figure 4.2. Therefore, even though the trends shown in Chapter 4 are smooth, unexpected data-points can show up in the dataset. Fortunately, these are quite visible, and very small for the scale where they are applied upon.

5.2. Dynamic Stability

In this section the eigenmotions Dutch roll, phugoid and short-period will be evaluated, according to the flight situations defined in Table 5.1. The tip-mounted propellers will have the largest effect on the Dutch roll compared to a conventional lay-out, since the engines are now much more effective in this motion due to their large moment arm. As for the phugoid and short-period, the engines are now simply positioned at another lateral position, yet the longitudinal and vertical moment arms will not really change with respect to conventional configurations. Therefore the phugoid and short-period analysis will be included briefly in this section, to test the applicability of the method to longitudinal analysis. For phugoid this works rather well, since it is a first order motion like the Dutch roll, yet the second order short-period motion displays the limitations of the method used.

5.2.1. Motion Damping and Frequency Extraction Approach

When subjecting the trimmed and stable aircraft to a disturbance, a motion will be initiated. This motion is called an eigenmotion. If the motion is periodic, two parameters can be obtained: the damping factor ζ

and the natural frequency ω_n, which characterise the damped oscillatory motion. These can be obtained by fitting an exponential curve to a relevant state variable's time-response curve due to some disturbance.

The relevant state variable's time-response curve is fitted to Equation (5.2) using SciPy's optimisation package. This exponential curve has first and second order modes fitted, since in for example the Dutch roll β_s response, both the spiral motion and the Dutch roll motion are captured. An example of this fitting procedure is given in Figure 5.6, where β_s is the aforementioned relevant state variable. The three lines are the reference aircraft, denoted by 'No TMP', a TMP version, and its fitted curve. The error on the fitted curve is marginal as one can determine by inspection. Damping and the natural frequency have increased in the TMP flight path. After applying Equations (5.3) and (5.4), the values in Table 5.2 are obtained. Both the damping factor and the natural frequency changed as expected. By this analysis the method of fitting this curve to obtain ζ and ω_n is considered verified.

$$y = a \cdot \exp^{b \cdot t} \cdot \cos(c(t+d)) + e \cdot \exp^{f \cdot t} + g \tag{5.2}$$

$$\omega_n = \sqrt{b^2 + c^2} \tag{5.3}$$

$$\zeta = \frac{-b}{\omega_n} \tag{5.4}$$

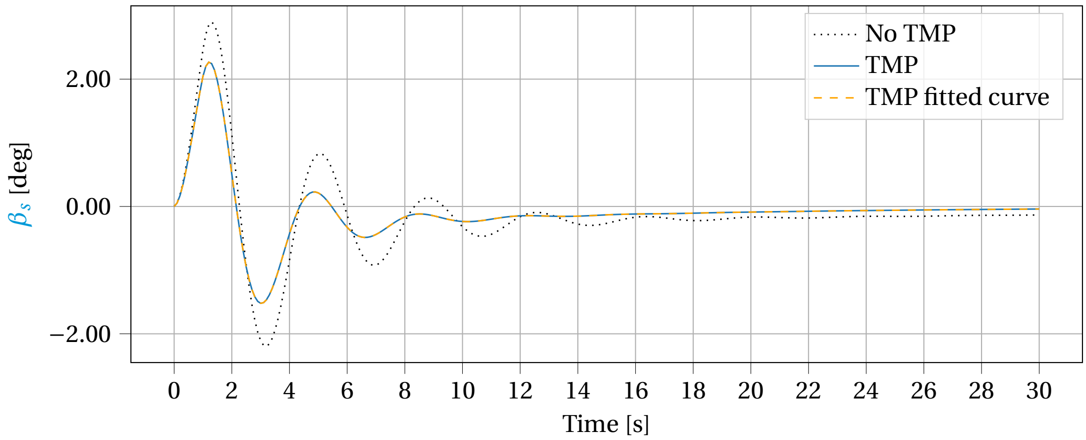

Figure 5.6: Dutch roll response curve fit example

Table 5.2: Dutch roll eigenvalues example

	No TMP	TMP
ζ	0.166	0.251
ω_n	1.697	1.791

This method of fitting a curve to the non-linear time response allows to include non-linear behaviour in the analysis. That this therefore is a better method than first linearising the model and consequently obtaining ζ and ω_n is defensible. However, it might be interesting to see how this method of fitting a curve compares to the Dutch roll eigenvalues from the linearised model. Since non-linearities are more common at low speeds than higher speeds, ζ and ω_n are compared for these two cases. The result is tabulated in Table 5.3.

The resulting ζ and ω_n are very comparable, where the largest error is obtained for ζ in the slow case. Since at higher speeds in a steady flight situation all lifting surfaces are in the linear regime and have clear measurable forces, the eigenvalues are expected to be very close to the linear solution. In the slow configuration the wing has separation at some points, and therefore introduces non-linearities. According to Table 5.3, ω_n for the non-linear case is still very close to the linear value, indicating that directional behaviour is rather linear in the non-linear flight model. ζ is less accurate, since the wing is prone to lose responsiveness at these speeds. In the remainder of this section only the non-linear model is used to obtain ζ and ω_n, since non-linearities will then be taken into account, increasing the accuracy of the model.

Table 5.3: Fit method verification for Dutch Roll

Case	Parameter	Linear	Non-linear
Slow	ω_n	1.6974	1.6973
	ζ	0.1743	0.1660
Fast	ω_n	2.7867	2.7700
	ζ	0.1895	0.1847

The flight situations as defined in the beginning of this chapter are dynamically evaluated in this section. These situations are listed in Table 5.1. For each of these situations, the aircraft is first trimmed, and consequently the aircraft's state time history after some disturbance is obtained. **For all cases, the original engines of the reference aircraft are set to idle**. This also means that in the upcoming analysis the aircraft state does not necessarily have to be the same. For example, if the TMPs are set to a high thrust setting, γ will be higher than for a low thrust setting. In all graphs, ζ and ω_n are obtained using the method described above. In all figures, the reference case of the unmodified aircraft is indicated as a dashed line, corresponding to $D = 0$[m], where its engines are set to idle.

5.2.2. Dutch Roll

Since the Dutch roll is the motion where the largest impact is expected for the tip mounted propellers, all cases from Table 5.1 will be shown and discussed here. First the motion's theory is discussed, after which the parameter sweep plots for ζ and ω_n will be shown. The motion here is introduced by a pulse rudder deflection of $\delta_r = 5$[deg] for 1s. Equation (5.2) is fitted to the time response of β_s, as graphically represented in Figure 5.6.

In the previous section the difference between linear and non-linear models is discussed, where it was concluded that a non-linear model includes more effects and is therefore more complete. The linear model does offer a significant advantage: using some simplifications an easy-to-use equation for the eigenvalues can be obtained. This equation in turn indicates the most important parameters. These parameters can then help us understand the time response of the aircraft. According to the simplified Dutch roll Equations (2.19) and (2.20) for ζ and ω_n respectively, C_{n_β} and C_{n_r} are the key drivers of the Dutch roll response, and C_{Y_β} is second order. In order to explain physically what is happening in the Dutch roll, the effect of TMP on the various parameters is tabulated in Table 5.4.

Now that the theory is established, the resulting parameter studies can be evaluated. The two thrust generating cases are depicted in Figures 5.7 and 5.8. The mid case, easiest to find by $f = 0.5$ for the ϵ_{TMP} line, shows an increase in ζ and ω_n with respect to the reference aircraft. The increase in ω_n is mainly due to the side-force of the propellers, increasing the static stability. The increase in ζ is mainly due to the damping of the propellers with yaw rate.

Both figures show the same parameter trends for each of the four variables. In general, the higher T_C* results in higher values for ζ and ω_n. Without a toe-in angle, C_{n_β} is always increased. Even so, the frequency for low blade pitches has decreased with respect to the reference case in Figure 5.8. This is since the blade is beyond stall, so the C_{n_r} due to TMP is positive, hence destabilising. In Figure 5.7, the points for $\epsilon_{TMP} = \pm 6.67$[deg] are omitted since these led to trimming problems, where the final speed of the aircraft would be 20% higher than intended.

Since the slopes of ζ and ω_n for all parameters except ϵ_{TMP} show the same trend in Figures 5.7 and 5.8, one can conclude that both C_{n_r} and C_{n_β} due to TMP have an impact on the Dutch roll motion: according to Equations (2.20) and (2.19), the frequency increases with C_{n_β}, and the damping factor decreases with C_{n_β}. Since both the damping factor and the natural frequency increase in the aforementioned figures, the absolute value of C_{n_r} must be increased by the tip mounted propellers. From Table 5.4 we know that this is true, especially for high values of T_C*.

For a further discussion on the applicability of these simplified Dutch roll Equations (2.19) and (2.20), a parametric TMP contribution to C_{n_r} analysis is included in Figures 5.9 and 5.10. When combined with C_{n_β} from Figures 5.1 and 5.2, all parameters of the simplified Dutch roll equation are present. Since ω_n depends on C_{n_β} only, this should reflect the exact same trends in Figure 5.7, which it does. The parametric line for J is

Table 5.4: TMP effect on Dutch roll parameters

Parameter	TMP force	TMP effect
C_{n_β}	Thrust X_p	If both the engines are aligned with the aircraft, no asymmetry due to sideslip will occur. However, when introducing a toe-in angle for the engines of ϵ_{TMP}, asymmetry will arise, and the moment arm to the engines will decrease. Let us consider a positive toe-in angle. If the aircraft gets a positive sideslip, the left propeller will lose thrust since α_p at that engine reduces, whereas the right propeller will gain thrust. Therefore, for positive ϵ_{TMP}, the thrust contribution to C_{n_β} is destabilising. For negative ϵ_{TMP}, the opposite will happen, and the stability will be increased.
C_{n_β}	Normal Y_p	Without any toe-in angle, the side force from both the propellers produce a restoring moment due to sideslip if the engines are located behind the CG. When a positive toe-in angle is introduced, the same will happen, yet the moment arm of the propeller side force has increased. A negative toe-in angle will decrease the moment arm. For pusher propellers, if the toe-out angle is increased to such an extent that the correcting moment switches sign, the contribution of the normal force can even become destabilising.
C_{n_r}	Thrust X_p	Consider ϵ_{TMP} is zero. If the aircraft has a positive yaw rate, the advance ratio on the left engine will increase, hence lose thrust. This results in a stabilising moment. Only when the blade is stalled, the resulting moment can be destabilising. In this case, a higher advance ratio will decrease the local angle of attack on the blade, allowing the flow to re-attach to the propeller and increase thrust instead of decrease thrust. A toe-in angle will decrease the arm of the thrust force and decrease the effective advance ratio change.
C_{n_r}	Normal Y_p	The normal force depends on the thrust coefficient and α_p. Let us consider a positive ϵ_{TMP}. For a positive yaw rate the thrust of the right engine is increased, increasing its normal force in negative Y direction, resulting in a destabilising moment. The opposite happens with $\epsilon_{TMP} < 0$.
C_{Y_β}	Thrust X_p	The contribution of the thrust force to Y_b will be negative for both positive as negative ϵ_{TMP}, unless the propellers are generating drag. No toe-in angle equals no contribution by definition.
C_{Y_β}	Normal Y_p	This contribution will always be negative. Toe-in or -out angles will reduce this effect.

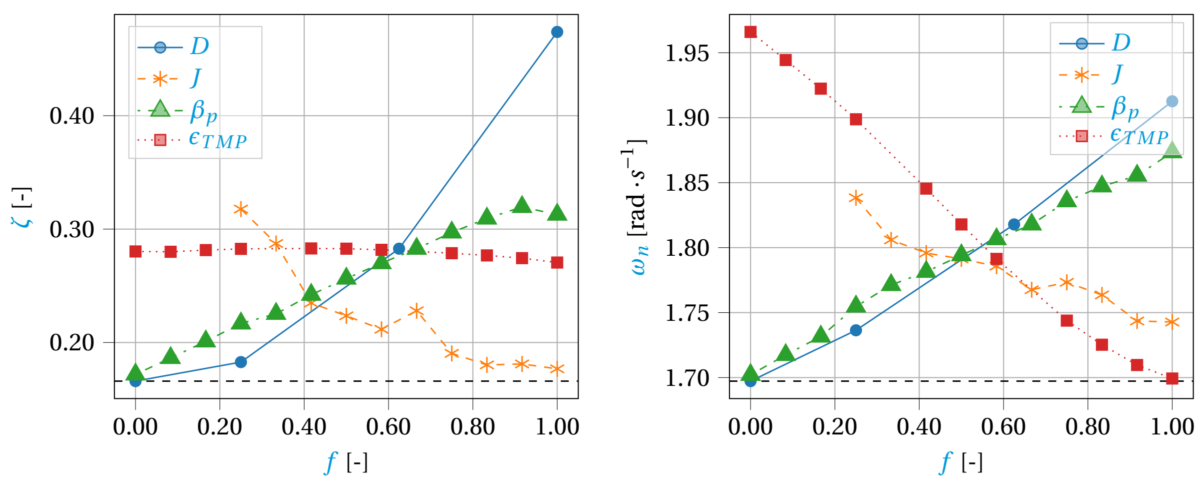

Figure 5.7: Slow cruise Dutch roll oscillation characteristics sensitivity analysis

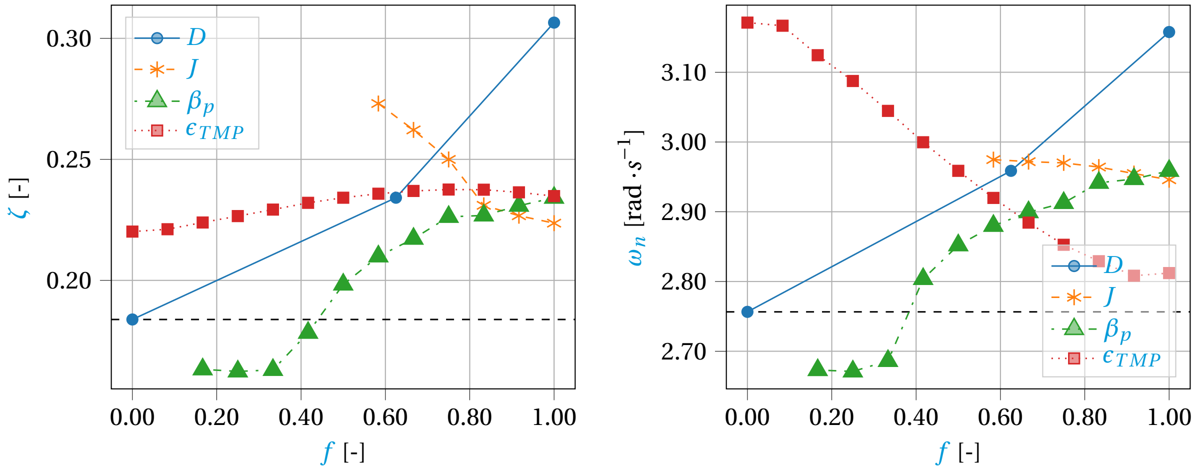

Figure 5.8: Fast cruise Dutch roll oscillation characteristics sensitivity analysis

not as straight as the C_{n_β} curve is. This is because the non-linear model moves through small thrust variations as discussed in Section 5.1, which do not limit us in our ability to conclude on the effect of varying thrust parameters. Comparing C_{n_r} in Figure 5.9 and ζ in Figure 5.7, one can see that the trends of C_{n_r} are copied exactly in an inverted fashion, as a more negative C_{n_r} increases the damping. This means that the contribution of the TMPs to C_{n_r} is larger than the contribution to C_{n_β}. An analogous approach can be followed for the fast case, yielding the exact same result and conclusion. That the contribution of C_{n_r} can become destabilising is portrayed in 5.8, where both ζ and ω_n decrease due to TMP for $f < 0.4$ for the β_s line. From Figure 5.10 we can obtain that the contribution of C_{n_r} indeed flips sign around $f = 0.4$. This effect is explained in Table 5.4, at C_{n_r} for X_p.

In cruise, we can conclude that both the damping as the natural frequency increase for the Dutch roll motion. To increase the frequency a negative toe-in angle should be attained, and more thrust increases both the frequency and the damping.

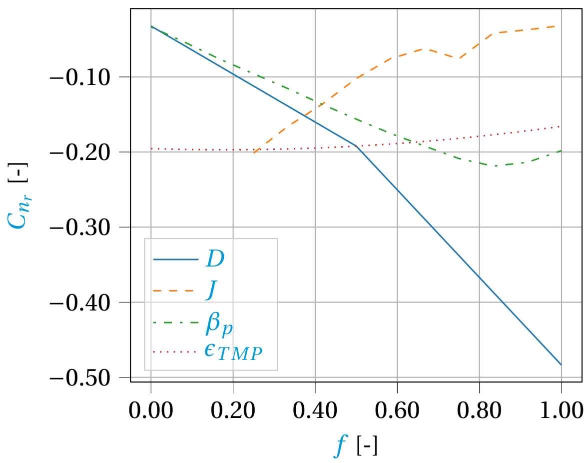

Figure 5.9: Slow cruise, TMP contribution to C_{n_r}

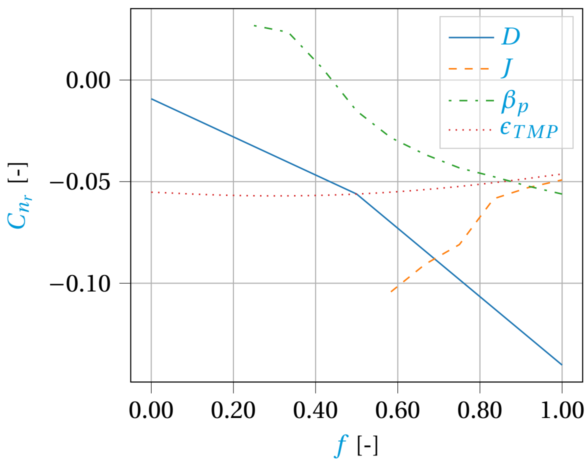

Figure 5.10: Fast cruise, TMP contribution to C_{n_r}

The descent cases, where the propellers are generating drag, in Figures 5.11 and 5.12 show more complex behaviour. Since the blades are configured for maximum power output and not for maximum performance in drag conditions, the range of available J is limited, as in for example Figure 4.9. Since in the descent case drag is generated, the side forces involved are small, by definition of Equation (2.10). Therefore the contribution of the tip mounted propellers to C_{n_β} is small. For higher values of J, the blade might be (partially) stalled as discussed previously, hence increase thrust with increasing advance ratio. This is true according to 4.9, leading to a local minimum in C_{n_β}, visualised by the ω_n curve as observed on the right hand side in Figure 5.12.

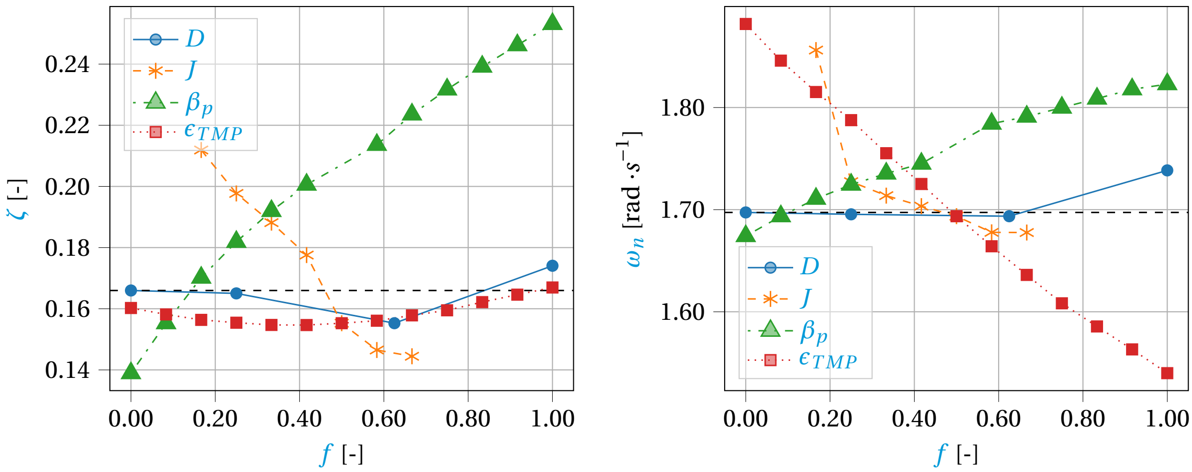

Figure 5.11: Slow descent Dutch roll oscillation characteristics sensitivity analysis

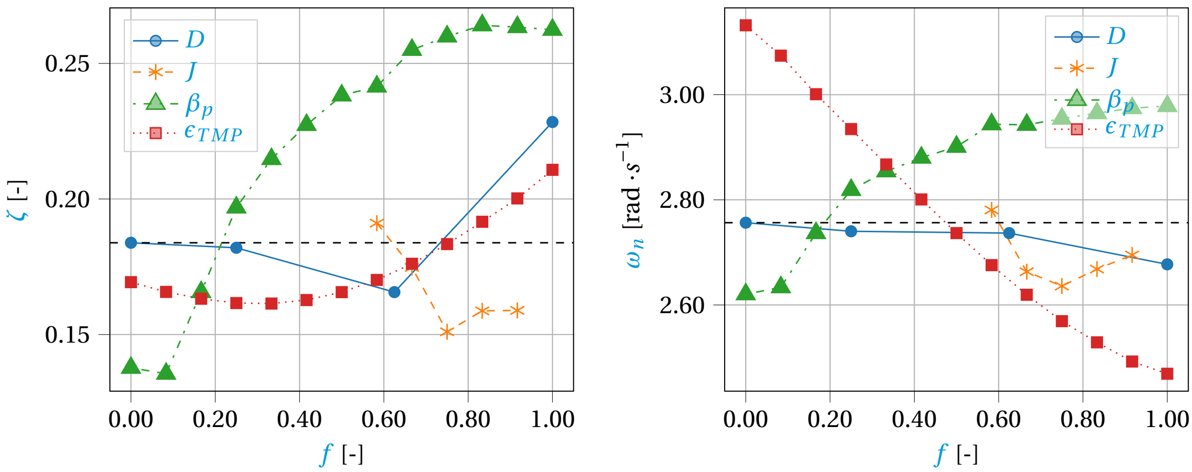

Figure 5.12: Fast descent Dutch roll oscillation characteristics sensitivity analysis

Even so, in the descent case, the parameter trends remain the same in comparison with the thrust generating case, unless hindered by stall phenomena. This does not hold for the toe-in angle. As in the thrust generating case the line corresponding to ϵ_{TMP} was nearly a straight line for ζ, it becomes a curve for the descent in Figures 5.11 and 5.12. The explanation for this comes from the contribution of the TMP to C_{n_r}, as previously stated in Table 5.4. Since the blade is so close to stall, where the thrust slope reverses with even higher advance ratios (for example visible in Figure 4.9, where for low blade pitches increasing J yields higher C_{nTMP}, hence more thrust), the contribution of the tip mounted propellers to C_{n_r} becomes destabilising. This explains the curve for ζ as a function of ϵ_{TMP}. To further support this conclusion, C_{n_r} for the descent cases is included here in Figures 5.13 and 5.14. Now that C_{n_r} is substantially smaller in magnitude than in the thrust-generating cases, the influence of C_{n_β} and C_{n_r} is both visible. For example, for ζ in Figure 5.12, the right hand side of the ϵ_{TMP} line is higher than the left hand side due to C_{n_β}. Yet the curve of C_{n_r} is also clearly visible, efficiently setting the minimum point for ϵ_{TMP} at $f = 0.3$. As in the thrust-generating case, the diameter amplifies both C_{n_r} and C_{n_β}. In the descent figures, the contribution of D to ζ is first negative, then positive. From the ω_n figures in these cases, we know that C_{n_β} is very small up to $D = 1.25$[m], hence letting C_{n_r} determine the trend. When the magnitude of C_{n_β} does get larger, the contribution of C_{n_β} is dominant, and sets the trend upward again. Since with increasing D the influence of the tip vortex gets smaller, where the tip vortex is detrimental to the propeller performance for a counter-rotating case compared to its isolated performance as discussed in Section 2.2, the propeller starts generating more thrust and hence more normal force for larger D in the drag-generating case.

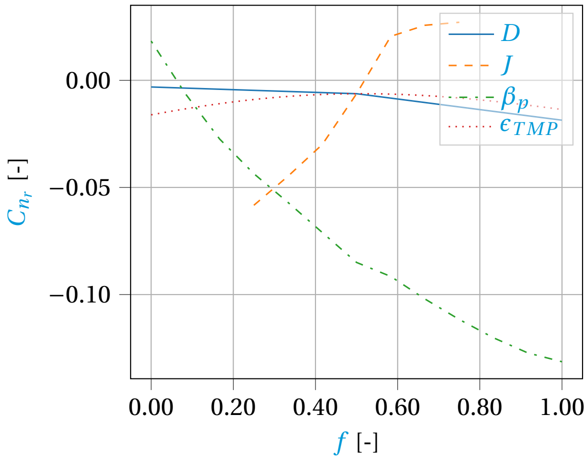

Figure 5.13: Slow descent, TMP contribution to C_{n_r}

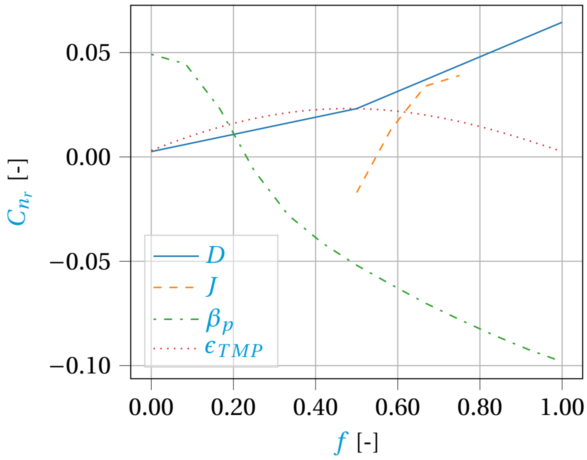

Figure 5.14: Fast descent, TMP contribution to C_{n_r}

As a note, one should not be tempted to say that the drag generating regime will degrade the Dutch roll performance. For example, in Figure 5.12, at β_p= 17.5deg (fourth point from the left), the propeller is still generating drag. However, the damping factor of the Dutch roll is higher than the reference value, proving that drag generation does not necessarily degrade dynamic stability. The performance of the stalled propeller must be evaluated in the same fashion as done here, as a propeller can hypothetically stall in flight. Whether this gives rise to hazardous situations has to be researched. Since this is not in the scope of the current research, this is left as recommendation.

Finally, in Figure 5.11 for β_p= 25[deg] the thrust value in the dataset was incorrect. The value returned by the dataset was around half the magnitude that β_p= 22.5[deg] or β_p= 27.5[deg] returned, and therefore the point is removed as an outlier. Since for all other blade pitches the trend is so coherent, this incorrect value does not influence our ability to draw conclusions from Figure 5.11.

5.2.3. Phugoid

The phugoid motion is a motion where potential and kinetic energy are interchanged. The rate at which each of these exchange energy determines the frequency, and the rate in which the energy dissipates per cycle gives the damping. As one can imagine, the engine plays are large role in this balancing act if the thrust is not assumed to be constant. Since the TMP engines are not necessarily different with respect to the vertical positioning than any other engine, an investigation into the behaviour of the phugoid in different thrust cases would not yield surprising nor unexpected results. Therefore this part is kept rather brief to discuss the applicability of the evaluation method for the phugoid, and only the parameter study for the most interesting case is shown, the other cases can be found in Appendix B. Since most cases only show straight trends in the phugoid, the fast cruise case is chosen to discuss due to its curved β_p trend. It is depicted in Figure 5.15. The motion is initiated by a step input of δ_e= −0.2865[deg], and Equation (5.2) is fitted to the time response of θ.

In Figure 5.15 one can see that all parameters have a considerable impact, except for the toe-in angle. Let us first review the ω_n graph. The responsiveness can be described as the amount of time the aircraft needs to respond to a change in velocity by changing the altitude, hence convert kinetic energy into potential energy. Therefore a key parameter is the derivative of Z_b with respect u. According to the graph, the higher the thrust, the higher ω_n and thus the responsiveness. With higher thrust, a larger pitch down moment is created since the engine is positioned above the CG. Therefore the elevator needs to be deflected upwards to counter this moment. Due to this extra loss in lift created, α of the wing needs to be higher. The higher the angle of attack of the wing, the higher the C_L of the wing, the higher the difference of Z_b with u. Hence, more thrust will increase ω_n.

The damping ratio ζ depends on the ratio between extra drag and extra lift due to some velocity

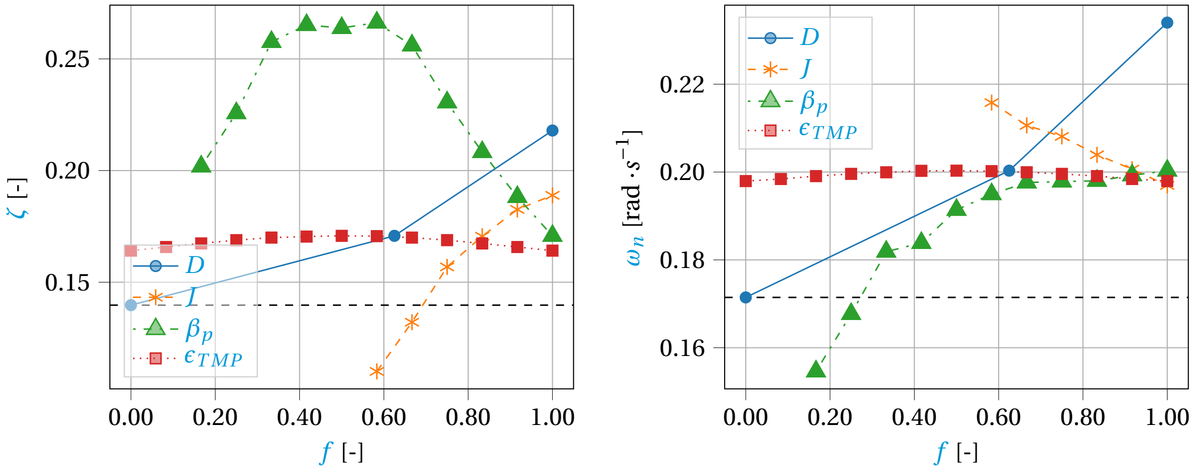

Figure 5.15: Fast cruise phugoid oscillation characteristics sensitivity analysis

disturbance. The extra lift contribution has just been discussed for ω_n. The change in drag due to velocity is somewhat easier to determine. Intuitively, we can say that if the advance ratio is increased, the local angle of attack on the blade decreases, decreasing T_C*, resulting in less thrust. This is a stabilising contribution. From Figure 5.15 we see that T_C* gets negative for $f \leq 0.6$ for the β_p curve. This is exactly where the ζ curve starts flattening in Figure 5.15. The derivative of T with V_∞ is given in Equation (5.5). Normally the rightmost part, $\delta T_C * / \delta V < 0$ according to Section 4.1. However, at very low blade pitches and high advance ratios, this trend reverses, as with the Dutch roll and its C_{n_r} contribution. This explains the left hand part of the β_p curve in Figure 5.15. In all other cases, higher thrust values are destabilising. Finally, ϵ_{TMP} degrades the TMP propeller X_b force. All mentioned effects are magnified, since this thrust force will create a moment due to the engine's placement above the CG. A decrement in thrust is converted to a positive moment change, pitching up the aircraft. Hence, more thrust will increase the responsiveness and decrease the damping in the phugoid.

$$\frac{\delta T}{\delta V} = \frac{1}{2}\rho S\left(2 \cdot V \cdot T_C * + \frac{\delta T_C *}{\delta V} V^2\right) \tag{5.5}$$

5.2.4. Short Period

In contrast to the previous two motions, the short period is a second order motion. This means that the first order motion needs to be subtracted from the time-history, and that the short period motion can be fitted upon that resulting curve. As one can imagine, this method is highly dependent upon the fit of the first order motion. From the previous sections, the Dutch roll and phugoid, confidence is built in the first order motion fit. However this section will suggest that the second order motion fit is unreliable, yet still the theory of this motion will be discussed. The motion is initiated by a step input of $\delta_e = -0.2865$[deg], and Equation (5.2) is fitted to the time response of q.

The short period is so rapid and so heavily damped, that the limits of the used method are reached. For the four situations, only the slow cruise case shows some trends, since for the other situations the method did not necessarily converge to an optimum line fit. These trends can be explained, yet for some jumps the author was not able to provide a solid line of argumentation. It is suspected that the inexplicable points are errors that propagate from fitting an equation to the result of subtracting the q response of the first order motion from the original q response. This is also hard to prove, since the found values are so close to each other. In such a fast and heavily damped motion differences are near impossible to analyse by hand.

The short period motion is a motion where the angle of attack and pitch rate vary rapidly. As one can imagine, the parameter C_{m_α} is very important, since this determines the aggressiveness of the stability. With a large C_{m_α}, a small disturbance in alpha will lead to a large force correcting this motion, hence leading to a rapid response. A discussion on the parameter effects on C_{m_α} has already been conducted in Section 5.1.

The effect of mounting the Piper Seneca with the tip-mounted propellers is displayed in Figure 5.16. Overall, the application of TMP decreased the damping ζ and increased the frequency ω_n compared to the base-line case without TMP. When comparing Figure 5.4 and ω_n for the short period, the same trends are found. Theoretically, with a large absolute C_{m_α}, the frequency should be high. To some extent this builds confidence in this second order fitting method. However, when reviewing the β_p line on the ω_n plot, an unexpected jump occurs at $f = 0.83$, after which the trend continues. This does not make any physical sense, and no explanation can be found in the analysis of the flight paths either. The aircraft is correctly trimmed at the start of the motion, and the input is correctly given.

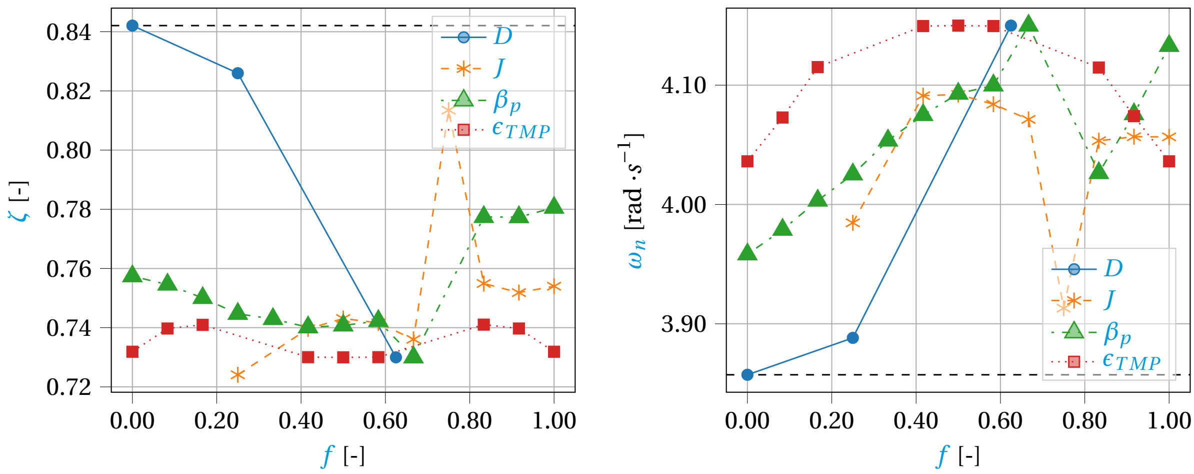

Figure 5.16: Slow cruise short-period oscillation characteristics sensitivity analysis

To illustrate the complexity of measuring this motion, the two responses for J=0.9 and J=1.6 are plotted in Figure 5.17. One should note that this is one of the largest differences attainable for either ζ and ω_n within this parameter sweep. In order to measure the damping, the 'desired' value for q for Time = 30 [s] has to be extrapolated from the rightmost part of the figure. We see that the curve for J= 1.6 has a higher peak than J= 0.9, yet the curve on the rightmost part of the graph is steeper for J= 1.6 than J= 0.9 as well. Even the frequency is hard to measure: the steeper the curve on the rightmost part of Figure 5.17, the longer the period will look since the dip after the first peak is then shifted right. This effect can be illustrated by looking for example at the curve $y = \cos x - x$. For $y = \cos x$ the minimum would be at $x = \pi$, yet for $y = \cos x - x$ one would intuitively say that the minimum occurs around $x = 4$. Hence, the Short period cannot be credibly analysed by fitting an exponential curve to the remainder of subtracting a first order curve from the original curve of q, nor by inspection from the time-history graph.

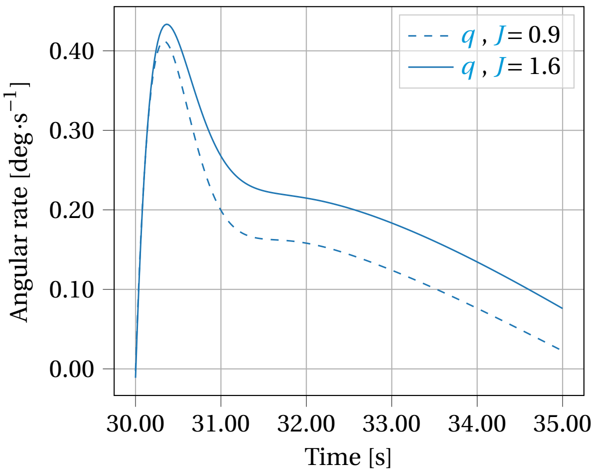

Figure 5.17: Slow cruise δ_e= −0.005[rad] step input time response

Whenever the natural frequency is increasing, the damping factor should decrease. Since the motion responds faster, and the swinging is not trivially dissipated faster, the amount of dissipation per cycle decreases. Overall this is true for Figure 5.16, yet most points remain inexplicable. ϵ_{TMP} shows a curve that resembles an M, where no scientific explanation can be found for. Furthermore, the jump in β_p is also present here, yet also for ζ no explanation can be given.

Since second order curves are very hard to fit, the line-fitting method to evaluate eigenmotion parameters does not work well. A better, well-proven method for this second order method would be a linear model, where eigenvalues can be readily extracted. This approach is not followed in this research, as the tip-mounted propeller implementation into Simulink did not allow for linearisation. Furthermore, the added value to this thesis would be small, as the effect of tip-mounted propellers will be relatively small on this longitudinal motion compared to a conventional configuration, since the vertical distance between the CG and propeller axis is similar. The linearised approach would force to accept that non-linearities would be disregarded, yet a solution will always be obtained. The exponential curve-fitting method does work well for first order motions. Since the fashion of fitting the curve is fundamentally different for the second order motion, the poor performance in the second order motion does not degrade the credibility of the first order motion conclusions.

6

Typical Stability and Control Contribution Assessment

Tip-mounted propellers have a significant effect on the dynamic stability of an aircraft, as presented in Chapter 5, where the contribution of TMP to directional stability is a design choice. Also the contribution to directional control can be significant, as stated in Section 4.3, where the amount of control power available is a design choice. To be able to see the actual contribution of TMP to the directional stability and control of an aircraft, a non-optimised typical design will be evaluated for directional static stability, directional dynamic stability, directional control, and compared with the reference aircraft. An attempt is done to relate the enhancement of directional stability and control to a reduction in VTP size, which will lead to a reduction in mass, drag and hence overall energy consumption.

First the design will be presented, followed by a discussion on the static directional stability impact, where empirical formulae will be used to relate the change in static directional stability to the VTP size. Then the change in Dutch roll eigenvalues will be discussed, along with a hypothetical discussion on how this could impact the VTP size, since a smaller VTP size can not be implemented to the flight mechanics model. Finally, time-history trajectories will be shown where a maximum rudder input of the original aircraft is compared with a non-optimised maximum TMP input by changing the propeller blade pitch.

Tip-mounted Propeller Diameter

The original Piper Seneca III has two engines. This original version will be referred to as the reference aircraft in the remainder of this chapter. As the new aircraft has to be fitted with tip mounted propellers, the amount of engines could still be two. However, it is not beneficial to the wing structural weight to move the engines to the tip. Therefore the original engines are left as they are, and two additional engines at the tip are added, which are also able to recuperate energy. This leads to the configuration as in Figure 1.5. This 'new' aircraft, having four engines of which two are driving a TMP, is referred to as the TMP aircraft in the remainder of this chapter.

The diameter of the propeller will determine the disk area, which has an influence on the thrust loading. Since the reference aircraft has two engines, where the TMP version has four, it is assumed that the needed power of the engines is simply divided over four instead of two. Hence, the maximum output power of the TMP engines is the original power of one engine divided by two, i.e. $K_P \leq 0.5$.

Assuming that the thrust to power ratio of the TMP engines, and the disk loading of the tip mounted propellers will be the same, only half of the original disk area per propeller is needed. Since the original propeller has a diameter of $D = 1.93$[m], the diameter of the TMP is calculated by Equation (6.1). This yields a value of 1.36[m], which is rounded to $D = 1.4$[m].

$$2\pi\left(\frac{D_{TMP}}{2}\right)^2 = \pi\left(\frac{D_{ref}}{2}\right)^2 \tag{6.1}$$

Tip-mounted Propeller Toe-in Angle

The toe-in angle is a key parameter for this design, as C_{n_β} is largely influenced by this angle. To what extent can be obtained from Figure 5.1. If the goal is to make C_{n_β} as large as possible, we would choose for the most negative value in this figure, which is $\epsilon_{TMP} = -20$[deg]. With such a negative toe-in angle, the engine would also produce an outward force Y_b. This is inherently lost energy, as both engines produce an opposing Y_b and will cancel each other out. This could therefore compensate the added benefits from placing the engine in the tip vortex. Furthermore, the exact interaction between the tip vortex and the propeller at a large toe-in angle has not been thoroughly investigated, and might therefore degrade the accuracy of the results.

As the diameter is set to $D = 1.4$[m], the ϵ_{TMP} curve in Figure 5.1 is scaled upward since this curve is drawn with $D = 1.25$[m]. What we now would like to know, is how much drag it saves to reduce the VTP size due to the enhanced C_{n_β}, and how much extra thrust is needed to compensate for the lost thrust in Y_b. This would quickly result in a large design mission, which is not the scope of this thesis. Since the cosine of 20 degrees indicates 6% loss in thrust (not taking into account increased thrust forces due to yaw, nor the added drag force due to propeller normal force), its loss is deemed to large. 10 degrees on the other hand, indicates a thrust loss of 1.5%. This is considered acceptable in comparison to the C_{n_β} gain indicated in Figure 5.1. Therefore, the toe-in angle is set to $\epsilon_{TMP} = -10$[deg].

Flight Cases Definition

Now that the design is defined, just as in Section 5.2, it must be evaluated in different flight cases to be analysed. First of all, the aircraft must be analysed in cruise. Since slow and fast cruise appeared to have different behaviour and demands for TMP, the slow and fast cases will be analysed here as well. Furthermore, the propellers can be used as spoilers, in a recuperation mode. Since the most negative power setting has proven to have high demands due to a positive C_{n_r} contribution of the propellers, this situation will be analysed as well. One has to keep in mind that this is a worst case scenario, and can easily be avoided by using a less negative thrust setting. Since the TMP aircraft will fly slow when extra drag is needed for descent slope control (e.g. during the landing phase), only the slow case is evaluated.

Table 6.1 state the engine settings for the three chosen cases. For completeness, D and ϵ_{TMP} are included as well, and will be the same in all cases. **In contrast to Section 5.2, the main engines are now enabled for both the reference aircraft as the TMP aircraft**. Since the trim and autopilot routines oscillate slightly for a power-on situation at airspeeds lower than 40 [m/s], an airspeed of 45 [m/s] is chosen for the slow cases. The fast cruise case is still at 80 [m/s].

Table 6.1: Evaluation cases definition

Case	Unit	Slow cruise	Fast cruise	Slow descent
V_∞	[m/s]	45.0	80.0	45.0
β_p	[deg]	30.0	40.0	12.5
J	[-]	1.0	1.8	1.3
D	[m]	1.4	1.4	1.4
ϵ_{TMP}	[deg]	-10.0	-10.0	-10.0

The chosen engine settings are done in a similar fashion as in Section 5.2. For specifics on how β_s and J are obtained the reader is referred to Chapter 5, where the engine settings for the flight situations in Table 5.1 are obtained. In short, the slow cruise case uses only the tip mounted propellers for thrust, so the main engines are idle. For the fast cruise case, not enough thrust is available by the TMP for sustained level flight. Therefore the maximum thrust is chosen, where the required engine power is smaller than half the original value, hence $K_P \leq 0.5$. The descent case is chosen upon maximum output power.

6.1. Static Stability

For directional static stability, C_{n_β} must be larger than zero for an aircraft. This value needs to be positive, as for any positive disturbance in β_s, the correcting yaw moment must be positive as well. The contribution of the VTP to C_{n_β} is positive, hence if we wish to increase the static stability of the aircraft, the TMP should contribute to a positive C_{n_β}.

If the static stability is increased by increasing C_{n_β}, one could decrease the size of the VTP to obtain the original C_{n_β}. According to Torenbeek [59, Ch. 9][1], C_{n_β} of the whole aircraft can be estimated with Equation

[1]The symbols that are used in this section are only used in this section, and are therefore not included in the glossary. If any confusion arises with respect to the symbols, the reader is referred to the glossary in Ref. [59]

(6.2). The rightmost part is then the contribution of the VTP. This leaves two unknowns, $C_{Y_{VTP_\alpha}}$ and $\left(\frac{V_{VTP}}{V}\right)$. The product of these two unknowns can be interpreted as a VTP efficiency factor. It is obtained by using the remainder of Torenbeek [59] his formulas in Equations (6.3) - (6.5). Used inputs values for the formulae can be found in Table 6.2. Values are obtained from Refs. [24, 26]. All units are used as defined by Torenbeek [59]. The analysis results in $C_{Y_{VTP_\alpha}}\left(\frac{V_{VTP}}{V}\right)^2 = 1.46$.

$$C_{n_\beta} = C_{n_{\beta_f}} + C_{n_{\beta_p}} + \Delta i C_{n_\beta} + \frac{S_{VTP} l_{VTP}}{Sb} \cdot C_{Y_{VTP_\alpha}} \left(\frac{V_V}{V}\right)^2 \tag{6.2}$$

$$C_{n_{\beta_f}} = -K_\beta \frac{S_{fs} l_f}{Sb} \left(\frac{h_{f_1}}{h_{f_2}}\right)^{1/2} \left(\frac{b_{f_2}}{b_{f_1}}\right)^{1/3} \tag{6.3}$$

$$K_\beta = 0.3 \frac{l_{cg}}{l_f} + 0.75 \frac{h_{f_{max}}}{l_f} - 0.105 \tag{6.4}$$

$$C_{n_{\beta_p}} = -0.053 B_p \sum \frac{l_p D_p^2}{Sb} \tag{6.5}$$

Table 6.2: Input values for directional stability estimation Equations (6.2) - (6.5)

Name	Value	Name	Value
S_{fs}	6.870	b_{f_2}	0.727
l_f	8.480	l_{cg}	3.376
S	19.390	B_p	2.000
b	11.860	l_p	2.160
$h_{f_{max}}$	1.185	D_p	1.930
h_{f_1}	0.919	$\Delta i C_{n_\beta}$	0.024
h_{f_2}	0.925	S_{VTP}	1.801
b_{f_1}	1.177	l_{VTP}	4.040

With this VTP efficiency factor, the contribution of the VTP to C_{n_β} can be calculated. When reducing S_{VTP}, C_{n_β} of the whole aircraft will decrease. This behaviour is depicted in Figure 6.1. The horizontal axis represents the fraction of the VTP that is mounted. From this figure one can obtain that the total contribution of the VTP to C_{n_β} is 0.0463.

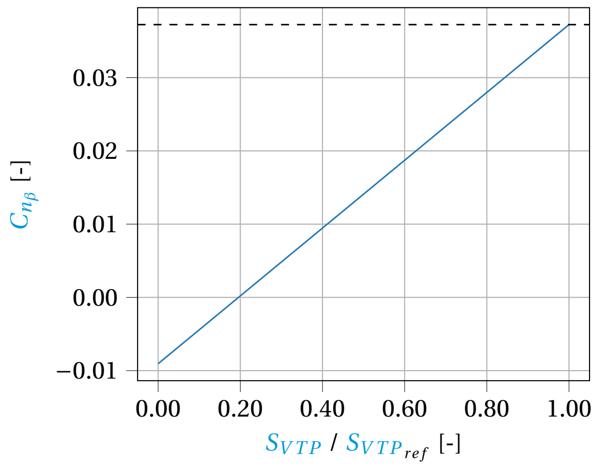

Figure 6.1: C_{n_β} of reference aircraft with varying VTP area

$$\frac{\Delta S_{VTP}}{S_{VTP_{ref}}} = \frac{-C_{n_{\beta_{TMP}}} \cdot S \cdot b}{l_{VTP} \cdot C_{Y_{V_\alpha}} \left(\frac{V_V}{V}\right)^2} \tag{6.6}$$

In Section 5.1 the contribution of tip mounted propellers to C_{n_β} is evaluated and depicted in Figure 5.1. If one would select a value of $\epsilon_{TMP} = -10$[deg], C_{n_β} would be around 0.15. This is scaled up a bit since that graph was for D=1.25[m], and the design has $D = 1.4$[m]. Using Equation (6.6) the resulting value of C_{n_β} due to TMP can be converted to a fractional reduction of S_{VTP}. This potential reduction of the VTP can be analysed for the previously defined cases, as C_{n_β} due to tip mounted propellers will vary with thrust settings (as indicated in Figure 5.1). The result of this evaluation is tabulated in Table 6.3.

Table 6.3: VTP reduction parameters

Case	Slow cruise	Fast cruise	Slow descent
$C_{n_\beta TMP}$	0.022	0.018	0.017
$\Delta\ S_{VTP}\ /\ S_{VTP ref}$	-0.484	-0.386	-0.367

The largest contribution of the tip mounted propellers to C_{n_β} is in the slow cruise case, where only nearly half of the reference S_{VTP} would suffice to keep C_{n_β} constant. In the fast cruise as slow descent cases, the fractions drop to 39% and 37% respectively. Therefore, to keep C_{n_β} at least the same as the reference aircraft, the TMP aircraft would need to have only 63% of the reference area of the reference VTP, hence reducing mass, drag and the overall energy consumption.

6.2. Dynamic Stability

The previous section has shown that tip-mounted propellers have a stabilising contribution to directional static stability, and thus enable a reduction in vertical tailplane size without sacrificing directional static stability performance. In this section the impact on dynamic directional stability will be investigated, by analysing the Dutch roll behaviour for the cases defined in the beginning of this chapter, in Table 6.1.

As a conclusion of the previous section, the gain in C_{n_β} was related to a potential decrease of S_{VTP}. Unfortunately, due to the way the Piper Seneca Simulink model is built, it is not possible to decrease the size of the VTP in the flight mechanics model. All moment and force coefficients that are influenced by the VTP, would need to be manually edited, since the model is not built in a parametrised fashion. As the linearised state-space system suggests in Equations (2.16) and (2.17), this would require editing numerous parameters. This is impossible to do within the time scope of this thesis. The feasible way to explore such an option, would be to build such a model from the ground up, and verify and validate it with the Piper Seneca model. This is placed as a recommendation for future research.

The dynamic stability analyses are performed without reduction in S_{VTP}, for reasons just explained. Since in Section 5.2 the Dutch roll eigenvalues seemed to correspond well with expectations from the linearised simplified Dutch roll Equations (2.19) and (2.20), an effort will be done to estimate a VTP size reduction from state derivatives as for example C_{n_β}.

In the same fashion as described in Section 5.2, ζ and ω_n are obtained for the different flight cases. The results are tabulated in Table 6.4. In slow cruise ζ is increased the most with respect to the reference aircraft, followed by fast cruise, and has decreased in the slow descent case. For all cases ω_n has increased.

Table 6.4: Dutch roll eigenvalues

	ζ		ω_n	
Configuration	Reference	TMP	Reference	TMP
Slow cruise	0.168	0.294	1.734	2.040
Fast cruise	0.183	0.235	2.739	3.140
Slow descent	0.167	0.138	1.706	1.934

This result is comparable with the results obtained in Section 5.2, where in the slow cruise configuration the largest gain was found in both ζ and ω_n. This gain was smaller in the fast cruise case, and even negative in the descent cases. However it was also mentioned there this behaviour in the descent case is because of the reversal of the TMP contribution to C_{n_r}. A higher thrust setting, i.e. less drag, would overcome this problem. Therefore, if one would wish to obtain at least the same damping, some negative thrust boundary must be set and not crossed in flight. This thrust boundary may be well into the negative thrust regime, as not all negative thrust values degrade the damping factor, yet only the thrust values near minimum power. For example,

Figure 5.11 states that for $\beta_p \geq 15$[deg] (corresponding to $f \geq 0.15$ for the β_p line), the TMP contribution to ζ is positive with respect to the reference aircraft. Figure 4.8 indicates that $\beta_p \geq 15$[deg] and $J = 1.3$ is still far into the negative power regime. Therefore, the recuperation abilities of the TMP are not compromised, yet slightly limited.

Dutch roll approximation formulas, which were used to support the theory described in Section 5.2, found in Equations (2.19) and (2.20), can be of help relating the enhancement in ζ and ω_n to a possible reduction in S_{VTP}. Since the Dutch roll trends for TMP in Section 5.2 conformed quite well to these equations, they can give a rough approximation for a possible reduction of S_{VTP}. For ω_n this yields a simple approximation, as it scales with the root of C_{n_β} (Equation (2.20)). To keep ω_n the same, one should strive to set C_{n_β} the same as the reference aircraft. This analysis is done in the previous section, where static stability was evaluated. The damping factor depends in this very simple approximation on three factors, C_{n_β}, C_{Y_β} and C_{n_r} in Equation (2.19). In the following analysis we will assume that the aircraft moves along a straight line, reducing C_{Y_β} to zero. Increasing C_{n_β} decreases the damping factor, yet in Table 6.4 the damping factor has increased. Since we know from the previous section that C_{n_β} increased, this suggests that the C_{n_r} contribution of TMP is large, hence the required contribution of the VTP to C_{n_r} decreases.

So let us review that the effect of reducing S_{VTP} is on C_{n_r}. The isolated C_{n_β} of the VTP can be used to calculate C_{n_r} of the VTP: a flight speed and yaw rate combined result in some inflow angle, which can be related to β_s. Hence, both are derived from a VTP having some inflow angle. One can convert the derivatives using Equation (6.7), obtained from mathematically manipulating the definitions of C_{n_r} and C_{n_β} for the isolated VTP. For the reference aircraft $2l_{VTP}/b = 0.68$. Now, let us obtain the relation between C_{n_r} and C_{n_β} for the TMP. This can be determined from for example Figure 5.9 for C_{n_r}. The contribution of the TMPs to C_{n_r} is around -0.2. The contribution of C_{n_β} can be obtained from Table 6.3, around 0.02. Hence, the contribution of TMP to C_{n_r} is an order of magnitude larger than the contribution to C_{n_β}. Therefore, if one decreases S_{VTP} to restore the TMP aircraft's C_{n_β} to the reference value, the damping factor in Equation (2.19) will always get higher since the enhancement of TMP in C_{n_r} is much stronger than the enhancement of the VTP in C_{n_r}.

$$C_{n_{r_{VTP}}} = -\frac{2 \cdot l_{VTP}}{b} \cdot C_{n_{\beta_{VTP}}} \tag{6.7}$$

Let us apply this methodology to the fast cruise case in Table 6.4. From Table 6.3 we can obtain that the contribution of TMP to $C_{n_\beta} = 0.018$. This can be brought down to the original value by decreasing S_{VTP} with 38.6%. The increase in C_{n_r} will then be $-0.68 \cdot -0.018 = 0.01224$, yet Figure 5.10 indicates C_{n_r} has decreased with a value around -0.05 (no exact value can be obtained from this figure since the figure is obtained from a slightly different simulation case). Since C_{n_r} has increased more by the contribution of the TMPs than reduced by reducing S_{VTP}, the damping factor ζ will still have increased with respect to the reference aircraft. This means that in this case the S_{VTP} reduction advice from Table 6.3 can be copied.

This advice will hold for the cruise cases, yet the tabulated result from Table 6.3 does not hold for the slow descent case, as it suffers from a destabilising C_{n_r} contribution from the TMP. However, if this flight situation of large negative thrust is simply not entered, one can neglect this constraint. A thrust boundary should then be set where the C_{n_r} contribution of the TMPs equals the reduction in C_{n_r} due to decreasing S_{VTP}. Such a design step to evaluate the limits of the aircraft is left for future work, as the focus of this thesis is to show the contribution of TMP to directional stability, as we have just done.

6.3. Directional Control Comparison

A first analysis into the control forces that are attainable with TMP was done in Section 4.3. It was concluded that the reachable moment coefficients with tip mounted propellers are comparable with the ones created by the original rudder. However, this does not show the flight mechanics behaviour of applying such a control force. Furthermore, it was stated that the determination of the amount of control force needed is a design problem. Now that an initial design is chosen, the behaviour of the aircraft subjected to a control force by tip mounted propellers can be analysed. This is done by reviewing a graphical representation of the aircraft state for one second after a maximum input. The purpose of this section is to review the flight behaviour due to a maximum control input by comparing state angles and angular rates for the TMP design and the reference aircraft. The reference aircraft will only use the rudder to yaw, and the TMP aircraft will only use β_p to yaw.

The directional control force coefficient of the TMPs varies with airspeed and engine settings, as indicated in Section 4.3. In this section, the same cases as for the dynamic motions in Section 6.2 are evaluated, defined in Table 6.1. Apart from these cases, two OEI cases are added. In these cases the maximum control deflections must be reachable without any input power, as if one engine fails in a TMP configuration both TMP must be switched off. Therefore this is the most restrictive case encountered when using TMP for directional control. For all cases, the model is first allowed to fly for 60 seconds, after which the desired input is given.

In the cruise and descent cases, both positive and negative input power can be used, where the positive input power is limited to $K_P \leq 0.5$. In the OEI cases positive input power is limited to $K_P \leq 0$.

The maximum control deflections are obtained from the propeller dataset, such that the resulting engine setting complies with the constraints posted above. Furthermore, the rotational speed n of the propeller is kept constant, so the only input variable to change the force on the propeller is the blade pitch β_p. Along this axis in the propeller dataset, a minimum and a maximum force is obtained, where the corresponding blade pitches are used as input. So for example the slow cruise case, will operate at the conditions described by Table 6.1. At this point in the propeller forces dataset, a maximum and a minimum thrust along the blade pitch axis is obtained, subjected to the power constraint mentioned above. The rudder is not deflected in the TMP case. For the reference aircraft, always a full rudder deflection is used, hence $\delta_r = -35$[deg].

In the remainder of this section, the new design will be referred to as 'TMP', and the reference aircraft without TMP as 'Ref'.

Yaw control response in slow cruise

In this case all power that is needed for a steady horizontal flight path can be supplied by the tip mounted propellers. For the TMP aircraft the original engines are set to zero power conditions, i.e. idle power setting. For the reference aircraft the power setting on the engines for a steady horizontal flight is set by the trim routine and the autopilot. The blade pitch deflection is $\beta_p = 30$[deg] and $\beta_p = 10$[deg] for the left and right TMP respectively. This is the maximum deflection attainable by the approach just described. Since β_p was already 30[deg] according to Table 6.1, only extra drag and no extra thrust is generated.

The resulting flight path due to the maximum TMP β_p by means of an angular representation of the aircraft state is depicted in Figures 6.2 and 6.3. In this case the TMP case can yaw quicker than the reference case can, attaining 115% of β_s of the reference aircraft after one second of full deflection.

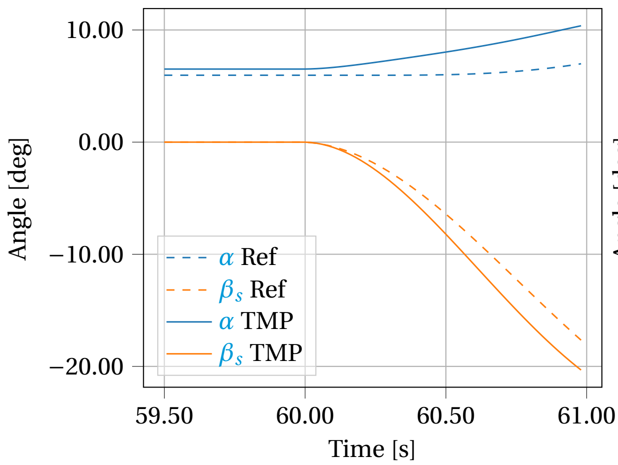

Figure 6.2: Slow cruise inflow angle response

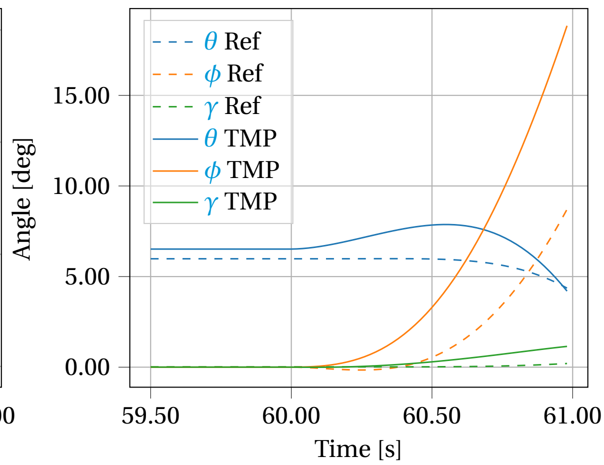

Figure 6.3: Slow cruise state angle response

As the propeller was not able to provide extra thrust for this advance ratio, the propeller could only be used as spoiler. Due to the deceleration, decreasing the flight velocity u, the angle of attack is increasing. Since the thrust force that was pushing the nose of the aircraft down is traded in for a drag force that is pulling the nose up, the aircraft starts pitching up, shown by the θ line in Figure 6.3.

When the rudder is negatively deflected, a negative moment is created along the X-axis in the body frame, hence a negative roll rate p is introduced as in Figure 6.4. Due to the yawing motion where the left wing is providing more lift than the right one, this roll rate is quickly reversed. Since the moment created along the X-axis in the body frame due to the TMP deflection is negligible, this adverse roll tendency is not present with the TMP aircraft. As the adverse roll is not present, the aircraft will directly have a positive roll rate. Therefore, the response in roll with a TMP control input is quicker for the TMP aircraft than the reference aircraft. Due to the pitch moment of the drag-generating engine, a strong pitch up motion develops, which is quickly more than compensated for by the increase in α. At the end of the analysis this even leads to a more aggressive pitch down motion than the reference case. For both aircraft α is increasing, as it is defined by $\tan^{-1}(w/u)$. The u component will decrease with increasing β_s, increasing the angle of attack.

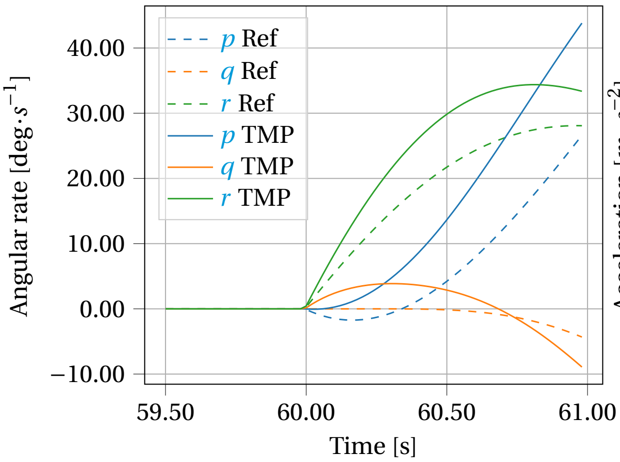

Figure 6.4: Slow cruise angular rate response

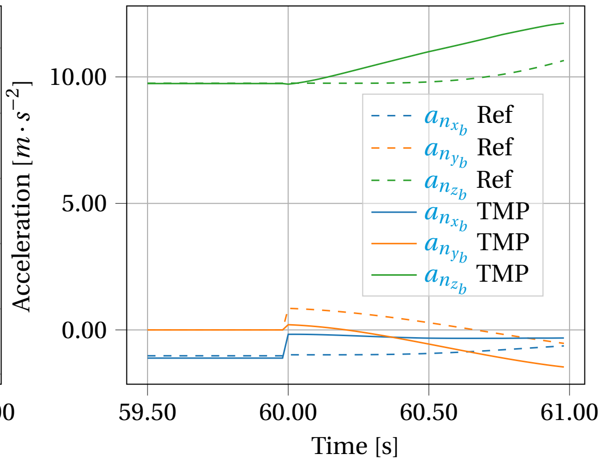

Figure 6.5: Slow cruise Cartesian normal accelerations

From Figure 6.5 the differences in Cartesian accelerations are readily obtained, as felt by the pilot/passenger of the aircraft, hence including gravity. Due to the sudden drag generation of the tip mounted propeller the aircraft decelerates. A small acceleration in Y is present since the thrust on the left engine is now higher, resulting in a force to the left (negative Y). The pilot therefore feels that he is pulled to the right (positive Y). For the reference case, the Y acceleration is due to the rudder input. This acceleration is much larger than the one created by the tip mounted propellers. Since the angle of attack is increasing, more lift is generated, which is increasing $a_{n_{z_b}}$ and increasing γ. Apparently the dihedral of the wing is providing enough lift when yawing that can compensate the loss of lift due to pitch rate.

Yaw control response in fast cruise

In the fast cruise case not enough thrust is available by the smaller tip mounted propellers to overcome the drag. Therefore the tip mounted propellers are set to a maximum thrust setting where $K_P \leq 0.5$, and the remainder of thrust needed is set by the trim routine on the main engines. The reference aircraft simply uses its main engines for thrust.

Since the TMP are set to a maximum thrust setting, no more thrust can be used to yaw, so only drag can be used. The yaw control capabilities will be smaller than in the slow cruise case since the minimum β_p that can be used in the propeller dataset is larger now. The blade pitch deflection is $\beta_p = 40$[deg] and $\beta_p = 20$[deg] for the left and right TMP respectively. The resulting flight angles are presented in Figures 6.6 and 6.7. As the angular rates and Cartesian accelerations for the fast cruise case are a scaling of the slow cruise case, these are not shown here.

In this fast cruise case the tip mounted propellers prove to be less efficient than the rudder for yaw control, since β_s after 1 second is 52% of the reference aircraft's β_s after 1 second. At such high speeds the propellers are unable to provide a large amount of thrust, resulting in lower thrust ranges than the slow cruise case. Furthermore, since the angle of attack is less than zero in Figure 6.6, and hence the local lift coefficient on the tips is less than zero, the tip vortex is degrading the propeller performance since the propeller will now co-rotate with the tip vortex.

The same trends due to the same influences are obtained in this fast cruise case as in the slow cruise case. Since the TMP yaw response is approximately half the yaw response of the reference aircraft, the development of state angles is somewhat more nuanced in Figure 6.7. So with respect to state trend development the slow and fast cruise cases are similar.

Yaw control response in descent

In this descent case, the propellers are set to a maximum power output setting for the TMP aircraft, so recuperating conditions. The propellers are thus generating drag. The reference aircraft is simply gliding

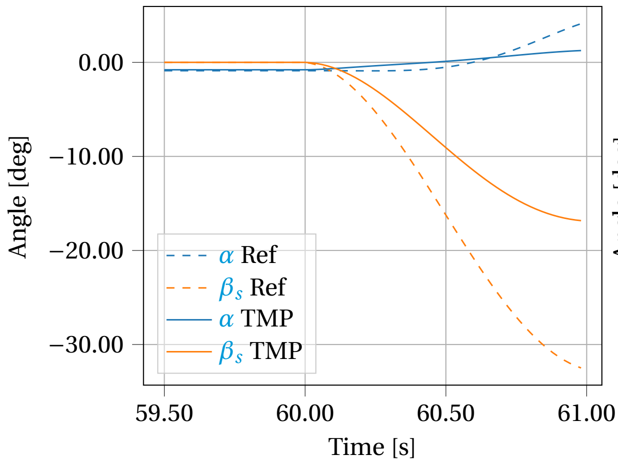

Figure 6.6: Fast cruise inflow angle response

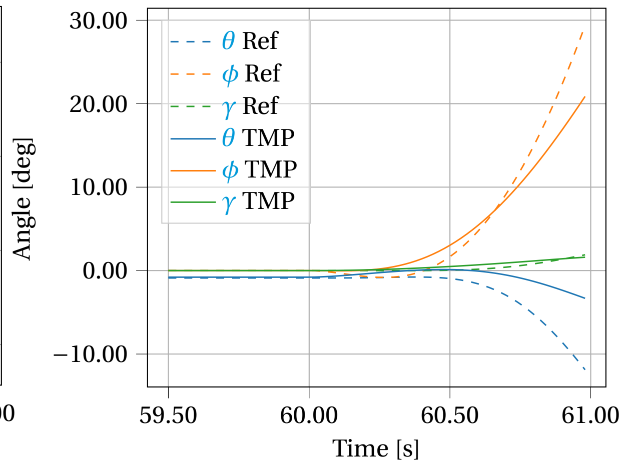

Figure 6.7: Fast cruise state angle response

with idle engines. The airspeed is set to 40 [m/s] in this case. The blade pitch deflection is β_p= 40[deg] and β_p= 10[deg] for the left and right TMP respectively.

The yaw control performance should be comparable with the slow cruise case, as the maximum inputs attainable should be comparable at similar flight speeds. The β_s response curve suggests that this is true in Figure 6.8, where β_s after one second of full deflection is 128% of the reference aircraft's β_s. However, the tip mounted propellers are now generating drag instead of thrust, resulting in a different pitch moment. Since drag will now be reversed to thrust, a pitch down motion is expected instead of first a pitch up motion, and then a pitch down motion. This expected behaviour is confirmed in Figure 6.9. In contrast to the slow cruise case, γ now declines for the TMP aircraft. The glide slope that the TMP aircraft attains is more than −10[deg], whereas γ is −6[deg] for the reference aircraft

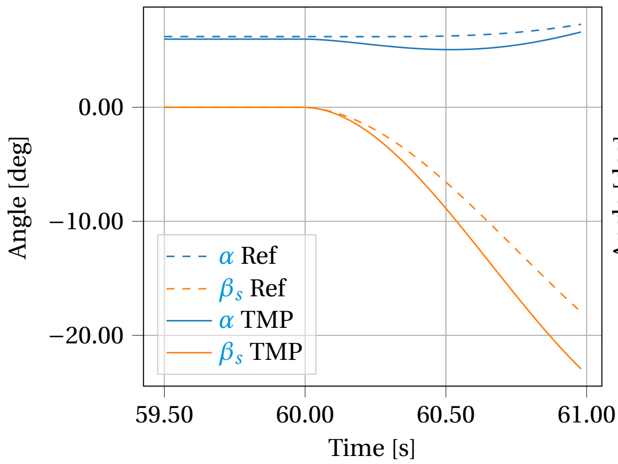

Figure 6.8: Slow descent inflow angle response

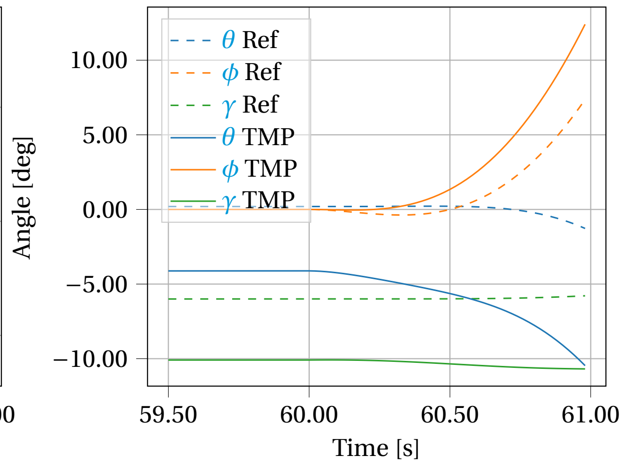

Figure 6.9: Slow descent state angle response

Figure 6.10 shows that q first goes down, remains constant, and slopes down again. When comparing this behaviour with α in Figure 6.8, the moment that q decreases again is the same moment when α is increasing. This also holds for the reference case. Hence, the aircraft behaves slightly different than the reference aircraft by a heavier pitch down manoeuvre and a larger roll response.

Yaw control response with one engine inoperative

Since TMP are rather inconvenient when one engine is inoperative, a critical part of the applicability of TMP for directional control is when a OEI situation arises. In this OEI case it is assumed that the rotational speed of the propeller can still be controlled, yet the power input to the propellers must be below zero. Hence,

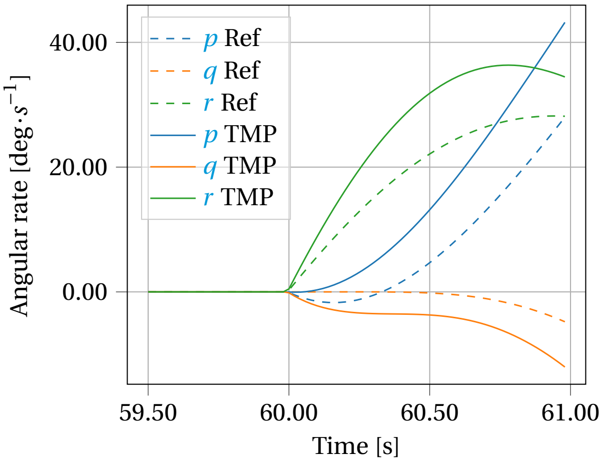

Figure 6.10: Slow descent angular rate response

the propellers are in recuperating conditions. Again a slow and a fast configuration is chosen, yet the fast configuration is now set to 60 $[m/s]$. This is done since it does not make sense necessarily to fly any faster with an engine inoperative. The blade pitch deflection is β_p= 21.5[deg] and β_p= 10[deg] for the left and right TMP respectively for the slow case, and β_p= 22[deg] and β_p= 10[deg] for the left and right TMP respectively for the fast case.

The corresponding angles for α and β_s are presented in Figures 6.11 and 6.12 for the slow and fast configurations respectively. The behaviour of the aircraft is similar to the descent case, where the propellers were producing drag as well. Since it is assumed that the propeller cannot produce thrust in this case, the yaw control performance is weaker. In the slow and fast cases the attained yaw angle after a second of full TMP deflection is 44% and 49% respectively of the reference aircraft's yaw angle after a second of full rudder deflection.

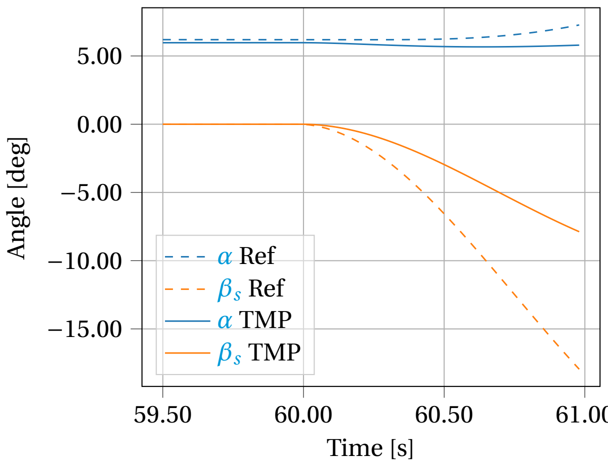

Figure 6.11: Slow OEI inflow angle response

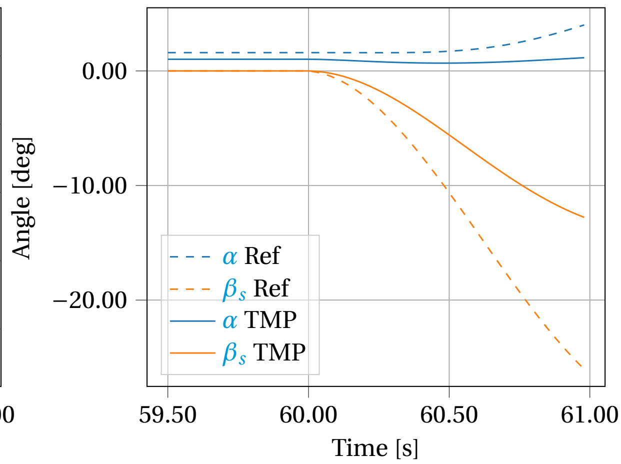

Figure 6.12: Fast OEI inflow angle response

In both cases the trimmed angle of attack for the TMP aircraft is smaller than the trimmed α for the reference aircraft. Due to the large drag force of the propellers, the TMP aircraft must compensate for this pitch up moment by deflecting its elevator downwards, resulting in a lift force up, alleviating the required α on the wings.

Since the input power to the propellers must be negative, the time history of the tip-mounted propellers input power is interesting as well. A static input to the blade pitch is given in the model. According to Figures 6.13 and 6.14, after the input is given, the left input power decreases. This indicates that the blade pitch could be increased, resulting in less drag, and therefore increase the yaw rate.

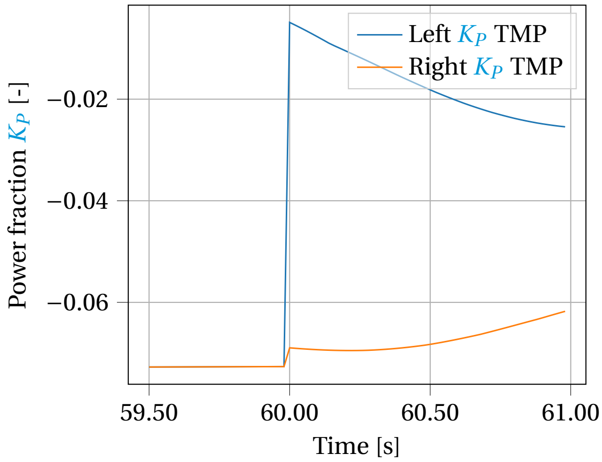

Figure 6.13: Slow OEI power fraction response

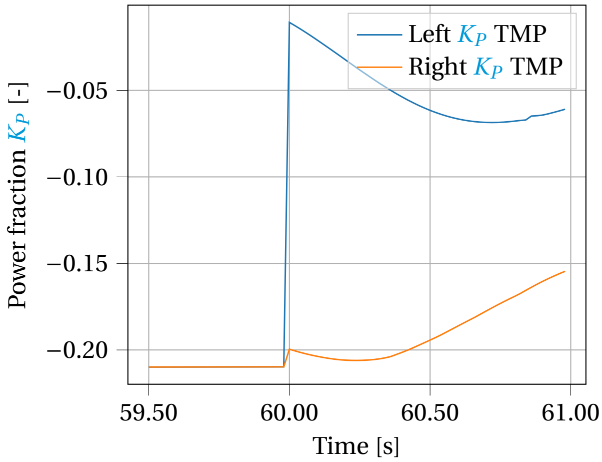

Figure 6.14: Fast OEI power fraction response

As one can see, in this very limiting case, the yaw angles attained are still around half of what the conventional aircraft can do. If one considers that the situation that is depicted here is not the analysis of a fully optimised design, this is a promising result for an aircraft fitted with TMP in a OEI situation.

Yaw control response reflection

In cases where thrust and drag forces are within operational range, as the slow cruise and slow descent cases, yaw control response to TMP is adequate. In more limiting cases, as the fast cruise and both OEI cases, observed TMP yaw control performance was around half the yaw control performance of the reference aircraft. All yaw control deflections using TMP were done without any optimisation, where only β_p could be varied. If a proper design study is to be undertaken, the yaw control performance of TMP would increase. If more directional control force is desired, the conventional rudder can still be used. This concludes the analysis on nominal operating conditions. However, if an aircraft enters a spin, sufficient yaw control authority must be present to recover from this flight situation. This study is not valid for this flight situation since (amongst other reasons) the inflow field on the propeller is not valid since the lifting line code cannot handle separated flow, nor is it relevant to the objective of this thesis. To extend the validity of this model into the stalled regime is left as recommendation.

Furthermore, if one would decrease the VTP area, the yaw performance of the TMP would be increased. If the goal is to reduce the VTP size, this must be possible from a control point of view. Based on the results of the yaw control response study, the VTP area can be reduced by 44% based on β_{sTMP} / β_{sRef} response fractions, if one assumes that the amount of β_s attained after a second of deflection is proportional to the rudder size. Finally, the descent angle for maximum recuperation $\gamma = -10$[deg], where the reference aircraft has a descent angle of $\gamma = -6$[deg]. This indicates that the TMPs can be used as descent slope controllers as well.

7
Conclusion & Recommendations

First the conclusion will be presented, followed by recommendations for future research.

Conclusion

The research question was formulated in Chapter 1. To be able to answer this question, four objectives are identified:

1. Develop a program that calculates the forces on a propeller that resides in the wing-tip vortex.
2. Evaluate the static stability contribution of tip-mounted propellers.
3. Simulate the dynamic response to a perturbation of an aircraft fitted with tip-mounted propellers.
4. Compare the time-response of a conventional rudder deflection and a tip-mounted propeller deflection for both positive and negative input power.

For each of these objectives the results will be summarised here. When combining these results a final conclusion can be formulated, as an answer to the research question.

Develop a program that calculates the forces on a propeller that resides in the wing-tip vortex

A lifting line program is written to estimate the velocity inflow field on a pusher propeller. The lifting line velocity field is validated by comparing it to a velocity field resulting from CFD analysis. The thrust and power are obtained from a combined blade-element momentum vortex model, which is widely used within the TU Delft. Empirical formulae are used to obtain the thrust, normal force and power when the propeller is subjected to an angle of attack. All assumptions are checked, and are shown to be applicable.

Evaluate the static stability contribution of tip-mounted propellers

A sensitivity study of the input parameters for the forces on the propeller is conducted. The input parameters are linked to the state of the aircraft by mathematical relations. Again a sensitivity study is conducted, yet now on the static stability contribution. C_{n_β} and C_{m_α} are evaluated. For the asymmetric case, the toe-in angle ϵ_{TMP} has a large influence, where a negative ϵ_{TMP} increases C_{n_β}. When considering the size of typical propellers for this TMP configuration, an indicative (no optimisation study is performed) vertical tailplane area reduction of 37% is obtained. For the symmetric case, the magnitude of thrust is the most important parameter. Higher thrust values make C_{m_α} more negative as the propeller axis is positioned above the centre of gravity. In a design study, the vertical distance between the propeller axis and the centre of gravity of the aircraft is an important parameter due to its large influence on C_{m_α}.

Simulate the dynamic response to a perturbation of an aircraft fitted with tip-mounted propellers

An exponential curve is fitted to the time-response curves of the flight mechanics model extended with tip-mounted propeller forces. Three motions are simulated: Dutch roll, Phugoid and Short period. The exponential curve method works well for the first order motions Dutch roll and Phugoid, yet degrades in accuracy for the second order motion Short period. For the Dutch roll motion, the toe-in angle ϵ_{TMP} has a large influence on the frequency ω_n of the motion, yet has a smaller influence on the damping ratio ζ. The main influence of thrust is on ζ, where more thrust increases ζ. For the Phugoid motion, higher thrust will increase ω_n and decrease ζ. For both motions, if the propeller is recuperating and hence generating negative thrust, a further attempt to decrease the thrust may destabilise the motion.

Compare the time-response of a conventional rudder deflection and a tip-mounted propeller deflection for both positive and negative input power

Since the propeller axis is positioned above the centre of gravity, a pitch moment is introduced when 'deflecting the TMP controls', hence changing the thrust of the propellers by changing the blade pitch β_p. Therefore the angle of attack increases more - with respect to a conventional rudder - when the TMPs are producing thrust, and decreases when the TMPs are recuperating. The roll rate over yaw rate fraction is larger in the TMP case, as the initial adverse roll (since the rudder is positioned above the CG) is absent. When a maximum deflection is initiated with TMP, where the highest respectively lowest thrust value at some advance ratio for the left respectively right TMP is selected, the yaw rate response r outperforms the conventional rudder when flying slow. When flying fast, the attained TMP sideslip angle β_s after one second is half the β_s produced by the rudder after one second. This is similar to the result obtained for a one-engine inoperative case, where β_s due to TMP deflection is a bit less than half β_s due to rudder deflection.

This leaves us with the research question.

Can tip-mounted propellers enhance the directional stability and controllability of an aircraft?

Yes. To enhance the directional stability, the rotation axis of the tip-mounted propellers should be placed outwards, hence with a toe-out angle. With respect to static stability, the vertical tailplane surface area can be reduced, depending on the design. A typical, not optimised design indicates that the vertical tailplane area can be reduced with 37%. With respect to control, a typical design shows that tip-mounted propellers can be more effective directional control devices than the conventional rudder. This control effectiveness compared to a conventional rudder decreases to 52% with increasing flight speed, and 44% when only negative propeller input power can be used, when for example one engine is inoperable.

Recommendations

This research is a first step towards a synergistic strategy of using tip-mounted propellers not only for enhanced propeller or wing performance, yet also for enhanced directional stability and control. This can reduce the size of the vertical tailplane, reducing drag and mass, and hence reduce overall energy consumption. Furthermore, the tip-mounted propellers can be used to recuperate energy on descent, reducing the overall energy consumption even further. This also offers glide-slope control possibilities. To work towards the implementation of TMP for stability and control, the following two areas of research should be investigated.

Extend propeller-wing model for stalled-regime validity

The rudder has a very important function that is not addressed in this thesis: if an aircraft enters a spin (one wing is stalled and the other one produces lift, resulting in a spiralling motion towards earth), the rudder is used to halt the spinning motion. Furthermore, as the TMP contribution to the Dutch roll damping becomes negative when sections of the propeller blade begin to stall, this regime might introduce hazardous situations by badly-damped eigenmotions or even departure. It is therefore of utmost importance to obtain a model that is valid in a stalled-wing/propeller regime.

Parametrise the vertical tailplane in flight mechanics model

To reduce the VTP size, the dynamic performance of a TMP aircraft with a reduced VTP size needs to be analysed. In the current model non-linear responses could not be obtained for a reduced VTP size. Only an enhancement/degradation with respect to the original aircraft could be measured. A flight mechanics model where the VTP is parametrised needs to be obtained. This can be done either by modifying the Piper Seneca model, or using/building a new parametrised model that can be verified by comparing it with the Piper Seneca model.

A

Propeller Forces Post-processing

In Section 3.2.3 the dataset post-processing using interpolation and application of β_p and J limits from Table 3.6 is explained. To visualise this interpolation, TMP yaw moment coefficient plots are used. The physical meaning of this plots is not repeated here, the sole purpose is to show the post-processing step. The dataset without interpolation results in Figure A.1, and after the post-processing step in Figure A.2. Values outside of the confidence-intervals of β_p and J are removed, and the values at J= 0.5 for β_p= 12.5, 15, 20 are interpolated as intended.

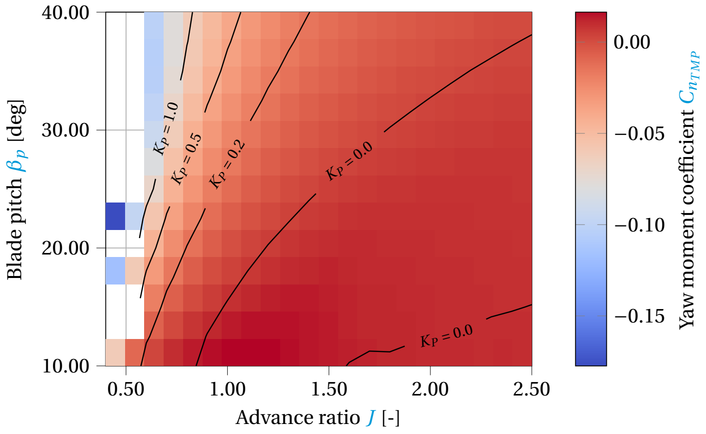

Figure A.1: Original TMP yaw moment coefficients

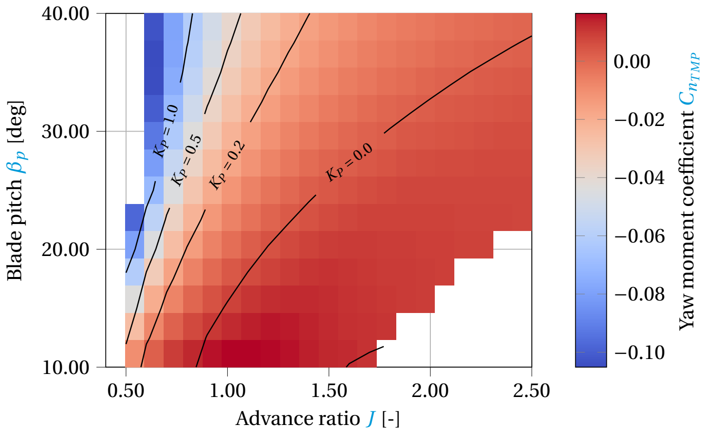

Figure A.2: Post-processed TMP yaw moment coefficients

B

Phugoid Sensitivity Analysis (cntnd.)

As the longitudinal motions are no necessary subject to answer the research question, yet might be interesting for the reader, the three remaining cases of the parametric phugoid motion analysis that were not included in Section 5.2.3 are presented here throughout Figures B.1 - B.3. Generally it can be stated that more thrust decreases the damping ratio, and increases the natural frequency.

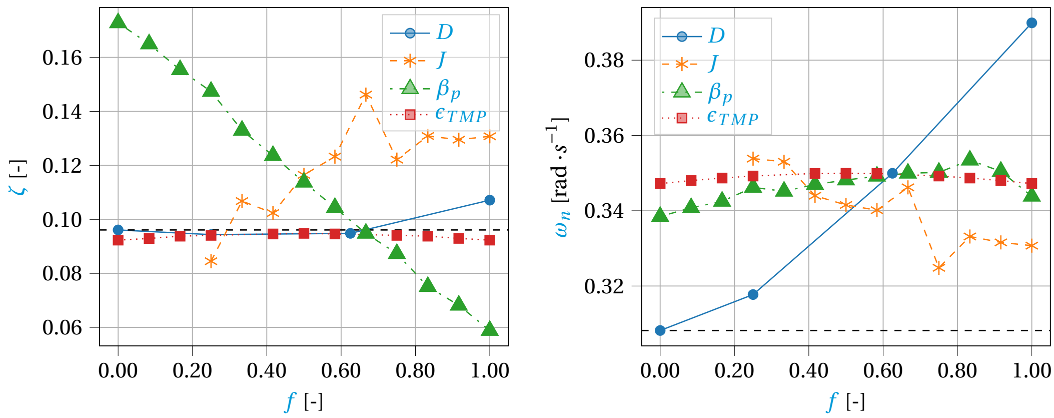

Figure B.1: Slow cruise phugoid oscillation characteristics sensitivity analysis

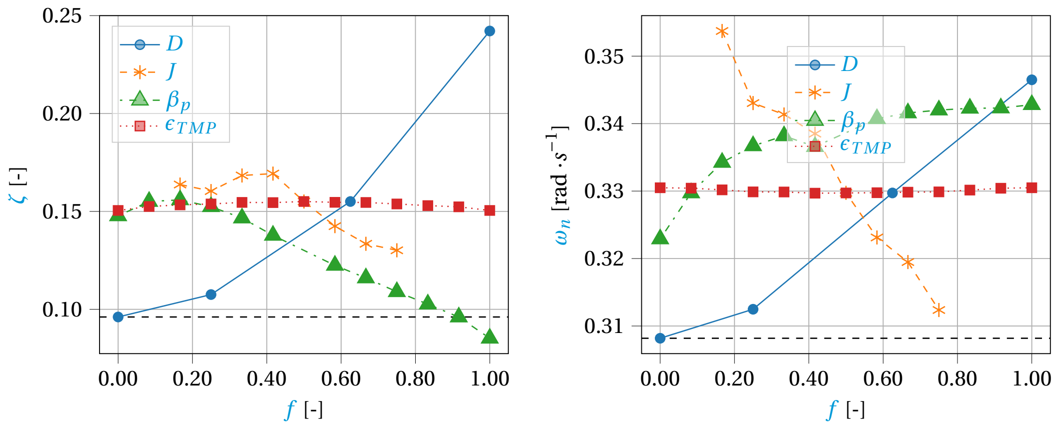

Figure B.2: Slow descent phugoid oscillation characteristics sensitivity analysis

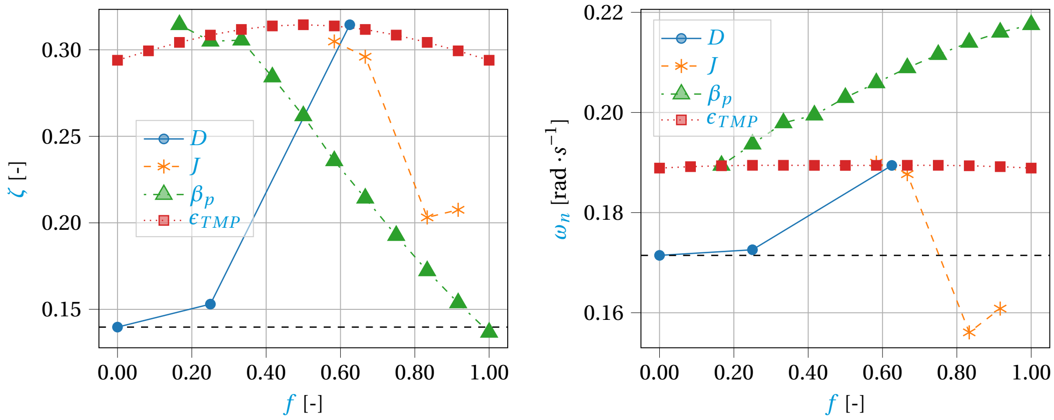

Figure B.3: Fast descent phugoid oscillation characteristics sensitivity analysis

Bibliography

[1] Wald, Q. R., "The Wright Brothers Propeller Theory and Design," *37th Joint Propulsion Conference and Exhibit*, 2001.

[2] Snyder, M. H. J., and Zumwalt, G. W., "Effects of Wingtip Mounted Propellers on Wing Lift and Induced Drag," *Journal of Aircraft*, Vol. 6, No. 5, 1969, pp. 392–397.

[3] Snyder, M. H. J., "Effects of a Wingtip-Mounted Propeller on Wing Lift, Induced Drag , and Shed Vortex Pattern," Doctorate thesis, Oklahoma State University 1967.

[4] Patterson, J. C., Jr, and Bartlett, G., "Effect of a Wing-Tip Mounted Pusher Turboprop on the Aerodynamic Characteristics of a Semi-Span Wing," *21st Joint Propulsion Conference*, American Institute of Aeronautics and Astronautics, 1985. doi:10.2514/6.1985-1286.

[5] Miranda, L. R., and Brennan, J. E., "Aerodynamic Effects of Wingtip-Mounted Propellers and Turbines," *4th Applied Aerodynamics Conference*, San Diego, CA, USA, 1986, pp. 221–228. doi:10.2514/6.1986-1802.

[6] Veldhuis, L. L. M., "Propeller Wing Aerodynamic Interference," Doctoral thesis, TU Delft 2005.

[7] Janus, J. M., Chatterjee, A., and Cave, C., "Computational Analysis of a Wingtip-Mounted Pusher Turboprop," *Journal of Aircraft*, Vol. 33, No. 2, 1996, pp. 441–444. doi:10.2514/3.46959.

[8] Stokkermans, T. C. A., van Arnhem, N., Sinnige, T., and Veldhuis, L. L. M., "Validation and Comparison of Rans Propeller Modeling Methods for Tip-Mounted Applications," *2018 AIAA Aerospace Sciences Meeting*, 2018. doi:10.2514/6.2018-0542.

[9] Sinnige, T., "Aerodynamic and Aeroacoustic Interaction Effects for Tip-Mounted Propellers," Doctoral thesis, TU Delft 2018. doi:10.4233/uuid:214e1e9a-c53e-47c7-a12c-b1eb3ec8293b.

[10] Ginter, S., *Chance Vought V-173 and Xf5u-1 Flying Pancakes*, Naval Fighters, Vol. 21, 1992.

[11] Brelje, B. J., and Martins, J. R. R. A., "Electric, Hybrid, and Turboelectric Fixed-Wing Aircraft: A Review of Concepts, Models, and Design Approaches," *Progress in Aerospace Sciences*, 2019, pp. 1–19. doi:10.1016/j.paerosci.2018.06.004.

[12] Jansen, R., Duffy, K. P., and Brown, G., "Partially Turboelectric Aircraft Drive Key Performance Parameters," *53rd AIAA/SAE/ASEE Joint Propulsion Conference*, American Institute of Aeronautics and Astronautics, Atlanta, Georgia, USA, 2017. doi:10.2514/6.2017-4702.

[13] Moore, M. D., "Misconceptions of Electric Aircraft and Their Emerging Aviation Markets," *52nd Aerospace Sciences Meeting*, American Institute of Aeronautics and Astronautics, National Harbor, Maryland, 2014. doi:10.2514/6.2014-0535.

[14] Ameyugo, G., "Distributed Propulsion and Future Aerospace Technologies," Ph.D. thesis, Cranfield University 2007.

[15] Schiltgen, B., Gibson, A. R., Green, M., and Freeman, J., "More Electric Aircraft: "Tube and Wing" Hybrid Electric Distributed Propulsion with Superconducting and Conventional Electric Machines," SAE Technical Paper 2013-01-2306, SAE International 2013. doi:10.4271/2013-01-2306.

[16] Barnes, J. P., "Regenerative Electric Flight: Synergy and Integration of Dual-Role Machines," *53rd AIAA Aerospace Sciences Meeting, 2015*, American Institute of Aeronautics and Astronautics Inc, AIAA, 2015. doi:10.2514/6.2015-1302.

[17] Welstead, J., and Felder, J. L., "Conceptual Design of a Single-Aisle Turboelectric Commercial Transport with Fuselage Boundary Layer Ingestion," *54th AIAA Aerospace Sciences Meeting*, California, USA, 2016, p. 1027. doi:10.2514/6.2016-1027.

[18] Patterson Jr, J. C., "Wingtip Vortex Turbine," U.S. Patent 4,917,332, 17 April 1990.

[19] Eržen, D., Andrejašič, M., Lapuh, R., Tomažič, J., Gorup, ., and Kosel, T., "An Optimal Propeller Design for in-Flight Power Recuperation on an Electric Aircraft," *18th AIAA Aviation Technology, Integration, and Operations Conference, 2018*, American Institute of Aeronautics and Astronautics Inc, AIAA, 2018. doi:10.2514/6.2018-3206.

[20] Deere, K. A., Viken, S., Carter, M. B., Viken, J. K., Cox, D. E., Wiese, M. R., and Farr, N. L., "Computational Component Build-up for the X-57 Maxwell Distributed Electric Propulsion Aircraft," *2018 AIAA Aerospace Sciences Meeting*, American Institute of Aeronautics and Astronautics, 2018. doi:10.2514/6.2018-1275.

[21] Borer, N. K., Patterson, M. D., Viken, J. K., Moore, M. D., Bevirt, J., Stoll, A. M., and Gibson, A. R., "Design and Performance of the Nasa Sceptor Distributed Electric Propulsion Flight Demonstrator," *16th AIAA Aviation Technology, Integration, and Operations Conference*, American Institute of Aeronautics and Astronautics, 2016. doi:10.2514/6.2016-3920.

[22] Sarlioglu, B., and Morris, C. T., "More Electric Aircraft: Review, Challenges, and Opportunities for Commercial Transport Aircraft," *IEEE Transactions on Transportation Electrification*, Vol. 1, No. 1, 2015, pp. 54–64. doi:10.1109/tte.2015.2426499.

[23] Gohardani, A. S., Doulgeris, G., and Singh, R., "Challenges of Future Aircraft Propulsion: A Review of Distributed Propulsion Technology and Its Potential Application for the All Electric Commercial Aircraft," *Progress in Aerospace Sciences*, Vol. 47, No. 5, 2011, pp. 369–391. doi:10.1016/j.paerosci.2010.09.001.

[24] de Muynck, R., "Aerodynamic Model and Engine Model of the Piper Seneca Iii," Preparational thesis report, Delft University of Technology August 1989.

[25] Koolstra, H., "Preventing Loss of Aircraft Control: Aiding Pilots in Manual Recovery from Roll-Limited Situations," Doctoral thesis, Delft University of Technology 2017. doi:10.4233/uuid:96053b94-0f1a-45cd-9e45-1f39e78c55de.

[26] Corporation, P. A., *Seneca Information Manual*, PUBLICATION DEPARTMENT, 1972.

[27] Anderson, J. D., Jr, *Fundamentals of Aerodynamics*, 5th ed., McGraw-Hill Education, 2011.

[28] Anderson, J. D., and Corda, S., "Numerical Lifting Line Theory Applied to Drooped Leading-Edge Wings Below and above Stall," *Journal of Aircraft*, Vol. 17, No. 12, 1980, pp. 898–904. doi:10.2514/3.44690.

[29] Phillips, W. F., and Snyder, D. O., "Modern Adaptation of Prandtl's Classic Lifting-Line Theory," *Journal of Aircraft*, Vol. 37, No. 4, 2000, pp. 662–670. doi:10.2514/2.2649.

[30] McCormick, B. W., *Aerodynamics of V/Stol Flight*, Academic Press, San Diego, 1999.

[31] Theodorsen, T., *Theory of Propellers*, McGraw-Hill, 1948.

[32] Wald, Q. R., "The Aerodynamics of Propellers," *Progress in Aerospace Sciences*, Vol. 42, No. 2, 2006, pp. 85–128. doi:10.1016/j.paerosci.2006.04.001.

[33] McCormick, B. W., *Aerodynamics Aeronautics and Flight Mechanics*, 1st ed., John Wiley & Sons, 1979.

[34] Drzewiecki, S., "Des Hélices Propulsives," *Bulletin de l'Association Technique Maritime*, Vol. 11, Imprimerie Gauthier-Villars, Paris, 1900, pp. 89–116.

[35] Gur, O., and Rosen, A., "Comparison between Blade-Element Models of Propellers," *Aeronautical Journal*, Vol. 112, No. 1138, 2008, pp. 689–704. doi:10.1017/S0001924000002669.

[36] Goldstein, S., "On the Vortex Theory of Screw Propellers," *Proc. R. Soc. Lond. A*, Vol. 123, No. 792, 1929, pp. 440–465.

[37] Crigler, J. L., "Comparison of Calculated and Experimental Propeller Characteristics for Four-, Six-, and Eight-Blade Single-Rotating Propellers," Tech. Rep. NACA-WR-L-362, National Advisory Committee for Aeronautics Februari 1944.

[38] De Young, J., "Propeller at High Incidence," *Journal of Aircraft*, Vol. 2, No. 3, 1965, pp. 241–250. doi:10.2514/3.43646.

[39] Ribner, H. S., "Propellers in Yaw," Tech. Rep. NACA-WR-L-219, NACA December 1943.

[40] Sinnige, T., Stokkermans, T. C. A., Ragni, D., Eitelberg, G., and Veldhuis, L. L. M., "Aerodynamic and Aeroacoustic Performance of a Propeller Propulsion System with Swirl-Recovery Vanes," *Journal of Propulsion and Power*, 2018, pp. 1–15. doi:10.2514/1.B36877.

[41] Sinnige, T., van Arnhem, N., Stokkermans, T. C. A., Eitelberg, G., and Veldhuis, L. L. M., "Wingtip-Mounted Propellers: Aerodynamic Analysis of Interaction Effects and Comparison with Conventional Layout," *Journal of Aircraft*, 2018, pp. 1–18. doi:10.2514/1.C034978.

[42] Sinnige, T., Stokkermans, T. C. A., Arnhem, N. v., and Veldhuis, L. L. M., "Aerodynamic Performance of a Wingtip-Mounted Tractor Propeller Configuration in Windmilling and Energy-Harvesting Conditions," 17-21 Juni 2019. doi:10.2514/6.2019-3033.

[43] van Arnhem, N., Sinnige, T., Stokkermans, T. C., Eitelberg, G., and Veldhuis, L. L., "Aerodynamic Interaction Effects of Tip-Mounted Propellers Installed on the Horizontal Tailplane," *2018 AIAA Aerospace Sciences Meeting*, 2018. doi:10.2514/6.2018-2052.

[44] Patterson, J. C., Jr, and Bartlett, G. R., "Evaluation of Installed Performance of a Wing-Tip Mounted Pusher Turboprop on a Semispan Wing," Article 01488341 (ISSN), NASA 1987.

[45] Catalano, F. M., "On the Effects of an Installed Propeller Slipstream on Wing Aerodynamic Characteristics," *Acta Polytechnica*, Vol. 44, No. 3, 2004, pp. 8–14.

[46] Mulder, J., van Staveren, W., van der Vaart, J., de Weerdt, E., De Visser, C. C., in 't Veld, A., and Mooij, E., "Flight Dynamics," 24-03 2013.

[47] Stokkermans, T. C., Nootebos, S., and Veldhuis, L. L., "Analysis and Design of a Small-Scale Wingtip-Mounted Pusher Propeller," 17-21 June 2019. doi:10.2514/6.2019-3693.

[48] van Arnhem, N., "Design and Analysis of an Installed Pusher Propeller with Boundary Layer Inflow," Master thesis, Delft University of Technology 2015.

[49] Klein, P. C., "Parametric Modeling and Optimization of Advanced Propellers for Next-Generation Aircraft," Master thesis, Delft University of Technology 2017.

[50] Hartman, E. P., "Negative Thrust and Torque Characteristics of an Adjustable-Pitch Metal Propeller," Technical Report NACA-TR-464, National Advisory Committee for Aeronautics. Langley Aeronautical Lab.; Langley Field, VA, United States 1933.

[51] Weick, F. E., "Working Charts for the Selection of Aluminum Alloy Propellers of a Standard Form to Operate with Various Aircraft Engines and Bodies," Technical Report NACA TR-350, NACA 1931.

[52] Li, Q., Öztürk, K., Sinnige, T., Ragni, D., Eitelberg, G., Veldhuis, L., and Wang, Y., "Design and Experimental Validation of Swirl-Recovery Vanes for Propeller Propulsion Systems," *AIAA Journal*, Vol. 56, No. 12, 2018, pp. 4719–4729.

[53] Yaggy, P. F., and Rogallo, V. L., "A Wind-Tunnel Investigation of Three Propellers through an Angle-of-Attack Range from 0° to 85°," Technical note, NASA 1960.

[54] Lesley, E. P., Worley, G. F., and Moy, S., "Air Propellers in Yaw," Technical Report NACA-TR-597, NACA 1937.

[55] McLemore, H. C., and Cannon, M. D., "Aerodynamic Investigation of a Four-Blade Propeller Operating through an Angle-of-Attack Range from 0 to 180 Degrees," Tech. Rep. NACA-TN-3228, NACA 1954.

[56] Ribner, H. S., "Formulas for Propellers in Yaw and Charts of the Side-Force Derivative," Tech. Rep. NACA-TR-819, NACA 1945.

[57] Van Bang, N., and Rozehnal, D., "Measurment of Aircraft Propeller in Yaw Flow," *6th International Conference on Military Technologies, ICMT 2017*, edited by V. Krivanek, Institute of Electrical and Electronics Engineers Inc., Brno, Czech Republic, 2017, pp. 566–569. doi:10.1109/MILTECHS.2017.7988821.

[58] "Military Specification Flying Qualities of Piloted Airplanes," 1980.

[59] Torenbeek, E., *Synthesis of Subsonic Aircraft Design*, student edition ed., Delft University Press/Martinus Nijhoff, 1982.